

Thèse

Présentée à

l'Université de Lille – Sciences et Technologies

Ecole doctorale Sciences de la Matière, du Rayonnement et de l'Environnement

Pour obtenir le grade de

DOCTEUR DE L'UNIVERSITE

Spécialité: Sciences des Matériaux

Alexandra M. GORYAEVA

Modélisation à l'échelle atomique des dislocations et de la plasticité dans la post-perovskite MgSiO_3

Soutenue le 6 Decembre 2016, devant le jury composé de

Dr. Andréa TOMMASI	Université de Montpellier 2	Président
Prof. Maureen D. LONG	Yale University	Examineur
Prof. Paul J. TACKLEY	ETH Zürich	Examineur
Prof. John P. BRODHOLT	University College London	Rapporteur
Dr. Laurent PIZZAGALLI	Institut Pprime, Poitiers	Rapporteur
Prof. Philippe CARREZ	Université de Lille 1	Directeur de thèse
Prof. Patrick CORDIER	Université de Lille 1	Directeur de thèse

PhD Thesis

l'Université de Lille – Sciences et Technologies
Ecole doctorale Sciences de la Matière, du Rayonnement et de l'Environnement

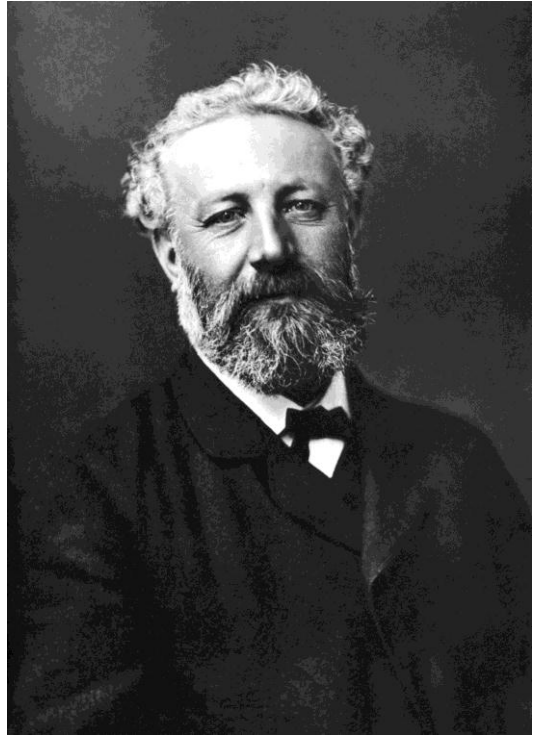
To obtain the degree of
DOCTOR
In Materials Sciences

Alexandra M. GORYAEVA

Modeling defects and plasticity in MgSiO_3 post-perovskite at the atomic scale

Scientific committee:

Dr. Andréa TOMMASI	University of Montpellier 2	President
Prof. Maureen D. LONG	Yale University	Examiner
Prof. Paul J. TACKLEY	ETH Zürich	Examiner
Prof. John P. BRODHOLT	University College London	Reviewer
Dr. Laurent PIZZAGALLI	Institut Pprime, Poitiers	Reviewer
Prof. Philippe CARREZ	University of Lille1	Supervisor
Prof. Patrick CORDIER	University of Lille1	Supervisor



*L'homme, simple habitant de la terre,
ne saurait en franchir les bornes. Mais
s'il est rivé à son écorce, il peut en
pénétrer tous les secrets.*

Jules Verne, 1903

Résumé

La couche D'' située à la frontière manteau-noyau est une région des plus complexes caractérisée en particulier par une forte anisotropie à différentes échelles. Inaccessible de par sa profondeur et caractérisée par des conditions de pression et de température extrêmes (au delà de 120 GPa et 2000 K), l'étude de cette région de la Terre représente un défi majeur qui ne peut être abordé qu'au travers de quelques observables géophysiques et d'expériences de hautes pressions qui mènent parfois à des résultats contradictoires. En particulier, les causes de la forte anisotropie sismique de D'' sont toujours l'objet de débats (orientations préférentielles de cristaux (CPO) ou d'inclusions, hétérogénéités thermo-chimiques,...). La contribution de l'orientation préférentielle des cristaux à l'anisotropie reste cependant une piste privilégiée compte-tenu de la structure très anisotrope de la post-perovskite. De plus, la couche D'' est une couche limite thermique à l'interface entre le noyau constitué d'un alliage de fer liquide et le manteau inférieur constitué de silicates solides mais au comportement visqueux. Les propriétés physiques de D'' sont donc particulièrement importantes pour comprendre les transferts thermiques en provenance du noyau et leur contribution à la convection mantellique. Ce phénomène implique l'écoulement plastique de roches contrôlé par le déplacement de défauts cristallins. Cependant, pour la post-perovskite, les informations concernant les propriétés mécaniques, les systèmes de glissement majeurs ou les défauts sont extrêmement parcellaires. Pour ces phases de hautes pressions, la modélisation numérique représente une approche de choix pour obtenir des informations sur les mécanismes de déformations élémentaires difficiles à obtenir par voie expérimentale. Le but de ce travail est d'étudier à l'échelle atomique les défauts majeurs de la post-perovskite MgSiO_3 (dislocations $[100]$, $[001]$ et $\frac{1}{2}[110]$) ainsi que leurs mobilités afin d'évaluer la capacité de cette phase à se déformer plastiquement par glissement de dislocations dans les conditions de la couche D'' .

Abstract

The D'' layer, located right above the core-mantle boundary (CMB), represents a very complex region with significant seismic anisotropy both at the global and local scale. Being a part of inaccessible deep Earth interior, characterized by extreme P - T conditions in excess of 120 GPa and 2000 K, this region is extremely challenging for interpretation relying only on the direct geophysical observations and high-pressure experiments, leading often to contradictory results. Thus, the reasons of the pronounced anisotropy in D'' are still debated (*e.g.* crystal preferred orientation (CPO), oriented inclusions, thermo-chemical heterogeneities *etc.*). Among them, contribution of CPO in anisotropic silicate post-perovskite phase is commonly considered as substantial. Furthermore, the D'' layer is a thermal boundary layer located at the interface between liquid iron alloy, constituting the outer core, and solid although viscous silicates of the lowermost mantle. As such, its physical properties are critical for our understanding of the heat transfer from the core, driving mantle convection. The latter is governed by plastic flow, which, in turn, is controlled by the motion of defects in crystals. However, for the high-pressure post-perovskite phase, information about mechanical properties, easy slip systems, dislocations and their behavior under stress is still scarce. For high pressure phases, numerical modelling represents a powerful tool able to provide the intrinsic properties and the elementary deformation mechanisms, not available for direct observations during high-pressure experiments. The aim of this study is to access the structure and mobility of [100], [001] and $\frac{1}{2}\langle 110 \rangle$ dislocations in MgSiO_3 post-perovskite, relying on the full atomistic modeling approach, in order to infer the ability of this phase to plastically deform by dislocation glide at D'' conditions.

CONTENTS

INTRODUCTION.....	13
CHAPTER 1. Literature overview on the post-perovskite.....	19
1.1. Post-perovskite crystal structure.....	20
1.2. Perovskite → post perovskite phase transition.....	21
1.3. Stability of post-perovskite at extreme pressures.....	26
1.4. Elasticity of silicate post-perovskite.....	29
1.5. Plastic deformation of MgSiO ₃ post-perovskite and its structural analogues.....	30
CHAPTER 2. Models and methods.....	35
2.1. Atomic scale modeling: methodology and computational setup.....	36
2.1.1. <i>Ab initio</i> calculations.....	36
2.1.2. Pairwise potential modeling.....	40
2.1.3. Nudged elastic band method.....	44
2.2. Atomistic modeling of planar defects.....	46
2.2.1 Generalized stacking faults.....	46
2.2.2. Twinning energy landscape.....	48
2.3. Atomistic modeling of linear defects.....	49
2.3.1 Designing and analyzing dislocation cores structures.....	50
2.3.2 Geometry of simulation cells.....	54
2.3.3 Computing lattice friction.....	57
2.4. Thermally activated dislocation glide.....	58
2.4.1. Kink-pair formation mechanism.....	58
2.4.2. LT model in conjunction with atomistic simulations.....	60
CHAPTER 3. Generalized stacking faults.....	63
3.1. Location of the shear planes.....	64
3.2. GSF excess energies.....	66
3.3. Validity of the pairwise potential.....	70
3.4. Influence of crystal chemistry.....	71
3.5. Searching for the easiest slip systems.....	74

3.6. Summary.....	74
CHAPTER 4. Dislocations with [100] Burgers vector.....	77
4.1. Stable dislocation cores.....	78
4.1.1. Screw dislocations.....	78
4.1.2. Edge dislocations.....	82
4.2 Anisotropic lattice friction: Peierls stress calculations.....	85
4.2.1. Glide of screw dislocations.....	85
4.2.2. Glide of edge dislocations.....	87
4.3 Peierls barrier and MEP of [100](010) screw dislocation glide.....	88
4.3.1. Pairwise potential calculations.....	88
4.3.2. DFT calculations.....	90
4.4 Line tension of [100](010) screw dislocations.....	92
4.5 Kink-pair formation on [100] screw dislocations.....	94
4.6. Summary.....	96
CHAPTER 5. Dislocations with [001] Burgers vector.....	99
5.1. Structure of stable [001] dislocation cores.....	100
5.1.1. Screw dislocations.....	100
5.1.2. Edge dislocations.....	102
5.2 Evolution of dislocation core characteristics with dissociation distance.....	103
5.3 Stacking fault energies.....	105
5.4 Dissociation process.....	108
5.5 Lattice friction.....	109
5.6 Kink-pair formation enthalpy.....	110
5.7. Summary.....	112
CHAPTER 6. Dislocations and deformation twinning with $\frac{1}{2}$[110] Burgers vector.....	113
6.1. Structure of $\frac{1}{2}$ [110] dislocation cores.....	114
6.1.1 Screw dislocations.....	114
6.1.2 Edge dislocations.....	116
6.2 Evolution of $\frac{1}{2}\langle 110 \rangle\{110\}$ dislocation cores under applied stress.....	118

6.3 Stacking fault structure and γ -energy.....	120
6.4 Modeling $\frac{1}{2}\langle 110 \rangle\{110\}$ deformation twinning.....	122
6.4.1 Generalized planar fault energy.....	123
6.4.2 Twin nucleation model.....	125
6.4.3 Twin morphology and critical twinning stress.....	128
6.5. Summary.....	130
CHAPTER 7. Discussion and implications.....	131
7.1. Structures of dislocation cores in MgSiO_3 post-perovskite	132
7.2. Anisotropic lattice friction.....	135
7.3. Thermally activated dislocation glide.....	139
7.4. Implications.....	142
CONCLUSIONS.....	147
PERSPECTIVES.....	151
Acknowledgements.....	153
Bibliography.....	155
List of publications.....	169
List of abbreviations.....	170

INTRODUCTION

Being restricted to the surface of the Earth, we tend to reveal the secrets of its inaccessible deep interior. An important source of information about the inner structure and composition of the planet comes from geophysical observations and from seismic waves that propagate through the Earth or along its subsurface after the occurrence of earthquakes. The travel time of seismic waves represents the first observable. Seismic wave velocities depend on the elastic properties and on the density of the matter through which the waves travel. This allows distinguishing the major divisions of the Earth's interior into a silicate mantle which extends to a depth of ~2900 km, and the iron rich metallic core with a radius of ~3400 km, subdivided into a liquid outer and a solid inner core (Fig. 1).

The Earth's mantle is not homogeneous with depth: abrupt variations in seismic body wave velocities indicate changes in structure or/and composition of the Earth's interior with depth. Based on such observations, the Earth's mantle is further divided into two major

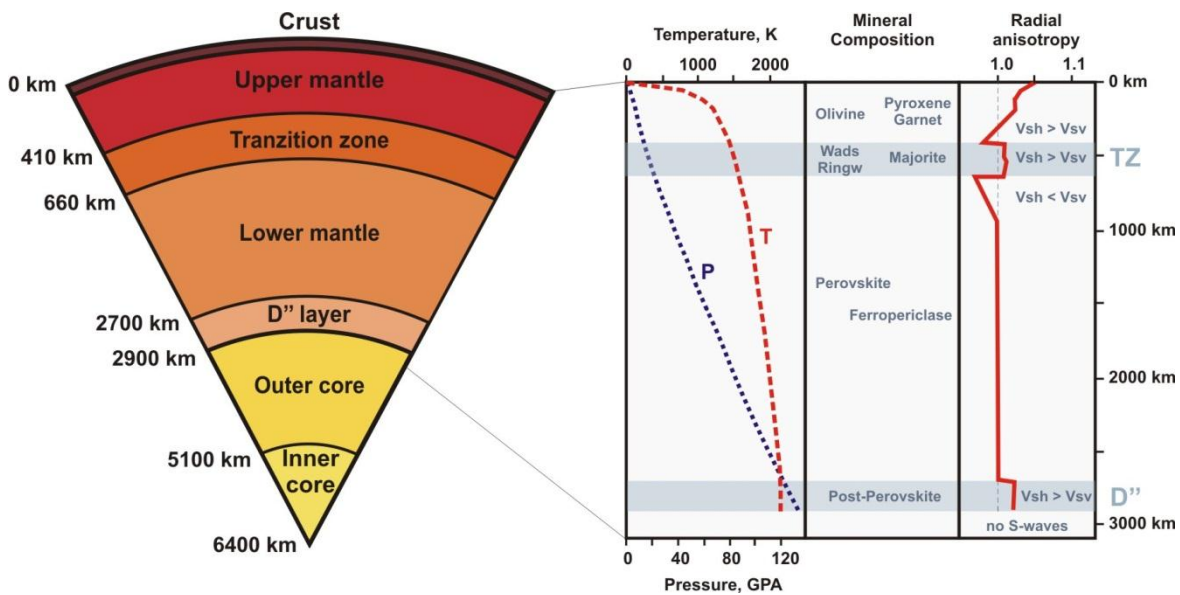


Fig.1. Schematic illustration of the Earth inner structure and the major distinct characteristics of the Earth's mantle. Right panel is taken from Mainprice et al. (2000). The radial seismic anisotropy profile corresponds to the seismic model SP6-F by Montagner and Kennett (1996).

parts: the upper mantle that extends to a depth of about 410 km and mostly consists of $(\text{Mg,Fe})\text{Si}_2\text{O}_4$ olivine (60%), $(\text{Mg,Fe,Ca})_2\text{Si}_2\text{O}_3$ pyroxenes and $(\text{Mg,Fe,Ca})_3\text{Al}_2\text{Si}_3\text{O}_{12}$ garnets; and the lower mantle between 660-2700 km mostly made up by $(\text{Mg,Fe,Ca,Al})(\text{Al,Si})\text{O}_3$ perovskite (PV), named bridgmanite in 2014 (Tschauner and Ma 2014), and $(\text{Mg,Fe})\text{O}$ ferropericlasite. Besides these two regions, there are two highly anisotropic layers of ~200 km thickness (Fig. 1) where horizontally polarized shear waves travel faster (velocity V_{SH}) than vertically polarized shear waves (V_{SV}): the transition zone (TZ) which separates the lower and the upper mantle, and the D'' layer located right above the core-mantle boundary (CMB). Sharp seismic discontinuities in the transition zone are known to be associated with subsequent phase transitions of $(\text{Mg,Fe})\text{Si}_2\text{O}_4$ olivine into wadsleyite at ~410 km depth and ringwoodite at ~520 km depth, while the nature of the profound D'' layer, lying almost halfway to the Earth's center, is still a matter of ongoing debates. Being located at the interface between the outer core and the lowermost mantle, where liquid iron alloy meets solid silicates, this region represents one of the most complex boundary layers of the Earth, where, for instance, the density contrast exceeds the one between the crust and the atmosphere. The properties of this region inevitably influence the processes occurring both in the core and in the mantle. Although being solid, the mantle undergoes slow convection due to the temperature and density gradient between its different regions. At the surface, downwelling zones are associated with cold and dense subducting slabs (the portion of a tectonic plate) sinking into the mantle, while the upwelling regions mainly correspond to the hot mantle plumes, rising from sources which may be as deep as the CMB (Fig. 2). Thus, the heat flow across the CMB plays an important role for the thermal structure of the planet, and contributes to the driving force of mantle convection.

Historically, the few hundred kilometers zone above the CMB were interpreted as a continuous thermal boundary layer, characterized by reduced seismic velocity gradient. This view has changed in the early 1980s, when the discontinuous increase in the shear wave velocities was first observed between 250 and 350 km above the CMB (Lay and Helmberger 1983). Since that time, numerous seismological observations (*e.g.* Weber 1993; Garnero and Helmberger 1995; Thomas *et al.* 2004; Lay 2008; Hutko *et al.* 2009; Long 2009; Cobden and Thomas 2013 *etc.*) have shown that the D'' region is much more

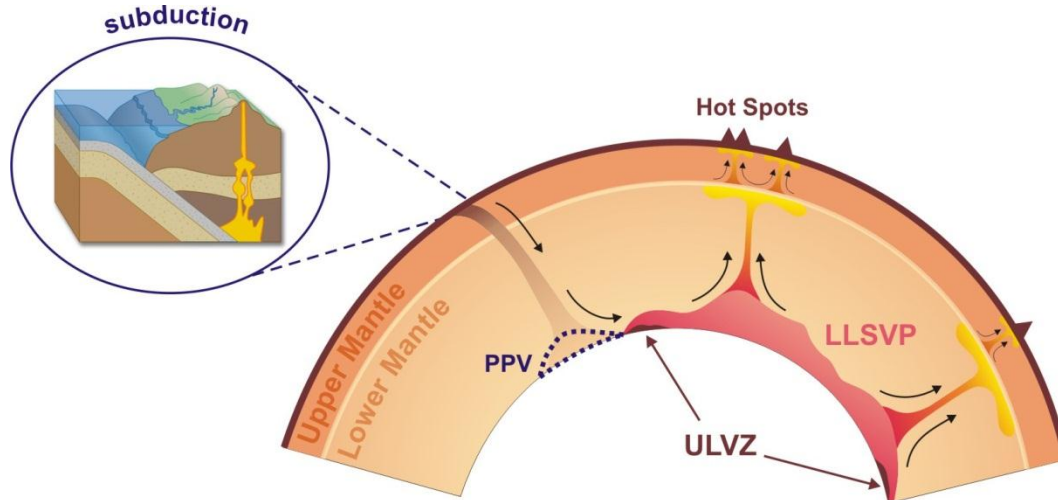


Fig.2. Schematic illustration of the distinct large scale structures at the bottom of the mantle and their possible role in mantle convection. LLSVP corresponds to the large low shear wave velocity provinces. Mantle plumes are generated at their top and entrain some fractions of the matter from the deep interior towards the surface. ULVZ stands for the ultralow velocity zones, likely represented by residuals of the magma ocean enriched in iron. The PPV zone corresponds to the lenses of post-perovskite, thought to be stable in relatively cold regions beneath the subducted slabs. The thickness of the PPV lenses strongly depends on the temperature. The picture is modified from Deschamps *et al.* (2015).

complex and heterogeneous than the rest of the lower mantle, where no major discontinuities are detected.

Topographically, global structures are detected in the deep mantle beneath Africa and South-Central Pacific (Fig.3). These zones are characterized by shear wave velocity anomalies of -2 to -5%, and therefore, defined as large low shear-wave velocity provinces (LLSVPs). It's generally accepted that these provinces, covering ~20% of the CMB, are hotter than the rest of the mantle and represent the main source of mantle plumes (see Davies *et al.* 2015 for a review). Location of LLSVPs is strongly correlated with location of the hot spots and the reconstructed eruption sites on the Earth's surface (Fig.3). However, seismic observations in LLSVPs cannot be explained by thermal anomalies alone. The exact nature of LLSVPs is still not clear and understanding compositional anomalies (*e.g.* enrichment in iron) is needed to better explain it.

Another low velocity anomalies at the bottom of the mantle are characterized by significant drop of V_P and V_S velocities by ~10% (Garnero and Helmberger 1995) and,

therefore, commonly referred as ultralow velocity zones (ULVZ). In contrast to LLSVPs, ULVZs form local structures of 5-40 km. These zones are generally observed at the edges of LLSVPs (Fig. 2) and interpreted as denser regions, possibly represented by pockets of partial melt enriched in iron (Williams and Garnero 1996; Rost *et al.* 2005).

Locally, regional seismic data also indicates presence of abrupt vertical changes in speed of both P and S waves at the top of D'' region. This abrupt changes are commonly referred as D'' discontinuity. Numerous studies reported existence of such structures between ~100 and 450 km above the CMB in different parts of the globe (see Cobden *et al.* 2015 for a review). Mapping the regions, where D'' discontinuity has been observed for S and P waves (Fig. 3), clearly demonstrates that D'' discontinuity does not form a global structure, but rather represents lenses locally disposed out of LLSVPs, *i.e.* in colder regions, likely associated with subducted slabs.

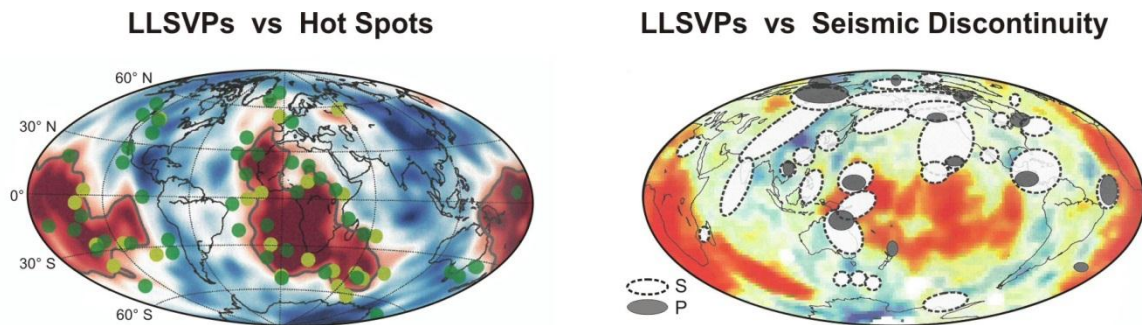


Fig.3. Superposing the shear wave tomography at the CMB (2800 depth) with location of surface hotspots (green dots on the left panel), reconstructed eruption sites (yellow dots on the left panel) and with S- and P-waves seismic discontinuities (right panel). On both plots LLSVPs correspond to the red areas. The pictures are taken from Davies *et al.* (2015) and Cobden *et al.* (2015).

By analogy with the phase transformations in the TZ, Sidorin *et al.* (1999) suggested that seismic observations of the D'' discontinuity could be explained by a mineral phase transition with a large positive Clapeyron slope of ~7 MPa/K. However, at that time no phase transition was known to occur and bridgmanite was believed to be stable down to the CMB (Knittle and Jeanloz 1987; Kesson *et al.* 1998) where pressures are expected to reach 120-135 GPa. In 2004, several research groups (Murakami *et al.* 2004; Oganov *et al.* 2004; Shim *et al.* 2004) independently demonstrated that MgSiO_3 bridgmanite transforms into

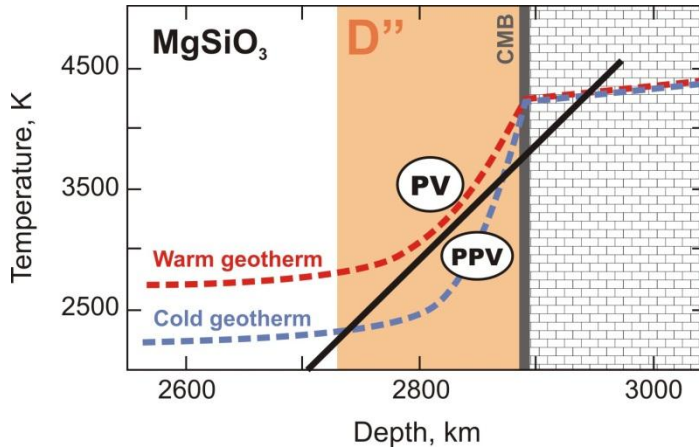


Fig.4. Schematic illustration of the relation between cold and warm geotherms at the bottom of the lower mantle with the PV→PPV transition boundary. The picture is modified from Hernlund *et al.* (2005).

layered MgSiO_3 post-perovskite (PPV) at pressures and temperatures in excess of 120 GPa and 2000 K (see Chapter 1 for more details), *i.e.* at the P - T conditions close to that in the lowermost mantle.

In agreement with the hypothetical suggestion by Sidorin *et al.* (1999), the so-called “last mantle phase transition” is characterized by a large Clapeyron slope of 6-11 MPa/K (Ono and Oganov 2005; Hirose *et al.* 2006a; Tsuchiya *et al.* 2004a), which indicates that lateral variations in the temperature at the CMB will result in large lateral variations in the transition depth. In cold regions, the post-perovskite transition rather occurs at relatively shallow depth, while in hot regions it may not transform at all (Fig. 4). Moreover, near the CMB where temperature increases rapidly, a back transition from PPV to PV (Fig. 4) may take place (Hernlund *et al.* 2005). Several seismologic observations indicate presence of double discontinuities, consistent with such a forward transformation, beneath the Pacific and the Caribbean (Thomas *et al.* 2004; Lay *et al.* 2006; van der Hilst *et al.* 2007; Hutko *et al.* 2008). However, taking into account large uncertainties in the thermochemical state of the lowermost mantle (Grocholski *et al.* 2012), the correlation between location of D'' discontinuities and location of cold regions can't be blindly interpreted as a direct evidence of PPV at the CMB. A major question is whether presence of this phase can explain the observed seismic anisotropy and discontinuity of D'' .

To answer this question, anisotropic seismic properties of the post-perovskite should be compared with the observed seismic data. Dynamic processes in the Earth's interior, such as mantle convection, cause deformation of the mineral phases that make up the mantle. At the mantle conditions, these rocks deform plastically under very low strain rates

(in the order of 10^{-16} - 10^{-14} s⁻¹) and their rheological behavior is controlled by the motion of defects in the crystal structure. Anisotropic mobility of defects produces crystal preferred orientation (CPO), which, in turn, significantly affects seismic properties of an aggregate. In this context, understanding anisotropic rheological and seismic properties of mineral phases is not possible without understanding the elementary deformation mechanisms at the microscopic scale. So far, the easy slip systems in the post-perovskite are poorly known. Silicate post-perovskite is only stable at very high P - T conditions and cannot be quenched to ambient pressure. Therefore, there is no direct experimental evidence of dislocations activity in this phase and the available information is limited to *in situ* XRD measurements of textures, from which one can only assume easy slip systems. Well controlled experimental deformation of minerals, followed by the micro texture analysis, are very challenging under extreme P - T conditions, and the textures observed experimentally for MgSiO₃ lead conflicting results (Merkel *et al.* 2007; Miyagi *et al.* 2011). Moreover, strain-rates accessible in a laboratory are 8-10 orders of magnitude larger than those in the mantle.

Alternatively, numerical modeling represents a powerful tool able to provide information on microscopic processes taking place in the deep Earth's interior. The present work aims to investigate fundamental mechanisms of plastic deformation in the high pressure MgSiO₃ post-perovskite through modeling defects and their mobility at the atomic scale, which in perspective will allow determining the relevant deformation textures resulting from dislocation creep in this phase at the lower mantle conditions.

CHAPTER 1

Literature Overview on the Post-Perovskite

In 2004, discovery of the so-called “last mantle phase transition” immediately became promising to shed light on puzzling properties of the D'' layer, including its marked seismic anisotropy. Since that time, anisotropic physical properties of the post-perovskite have been intensively studied in order to answer the major question whether this phase can explain the enigma of D'' . This chapter provides a bibliographic overview of MgSiO_3 post-perovskite physical properties, essential for understanding rheological properties in the lowermost mantle, and summarizes the results of high-pressure experiments and numerical modeling performed within the last 12 years. The overview includes the description of the intrinsic crystal structure; experimental and theoretical evidence of the post-perovskite transition boundary and stability field at extreme pressures; insights into anisotropic elasticity and analysis of the available data on plastic deformation of silicate post-perovskite and its low-pressure structural analogues.

1.1 Post-perovskite structure

High-pressure MgSiO_3 post-perovskite phase exhibits orthorhombic CaIrO_3 -type crystal structure (space group $Cmcm$, $z=4$) with anisotropic unit cell parameters $a=2.456 \text{ \AA}$, $b=8.042 \text{ \AA}$ and $c=6.093 \text{ \AA}$ at 121 GPa (Murakami *et al.* 2004). The occupied Wyckoff positions are $4c$ for Mg, $4a$ for Si, and $4c$ and $8f$ for O. Uncommonly for high-pressure minerals, post-perovskite is characterized by the presence of two non-equivalent cation layers parallel to (010). These layers are formed by Si-octahedra and eightfold coordinated Mg exclusively (Fig. 1.1). Along [100], Si-octahedra share edges forming rutile-like chains which are interconnected by apical oxygen atoms along [001] direction, building up (010) Si-layers. In contrast to the octahedra, centered by highly charged Si atoms, Mg polyhedra are linked with each other and Si-layers by edges and triangle faces. Due to the octahedral junctions by vertices, in the dense post-perovskite structure there are still [100] empty channels with pseudo trigonal symmetry (left panel of Fig. 1.1).

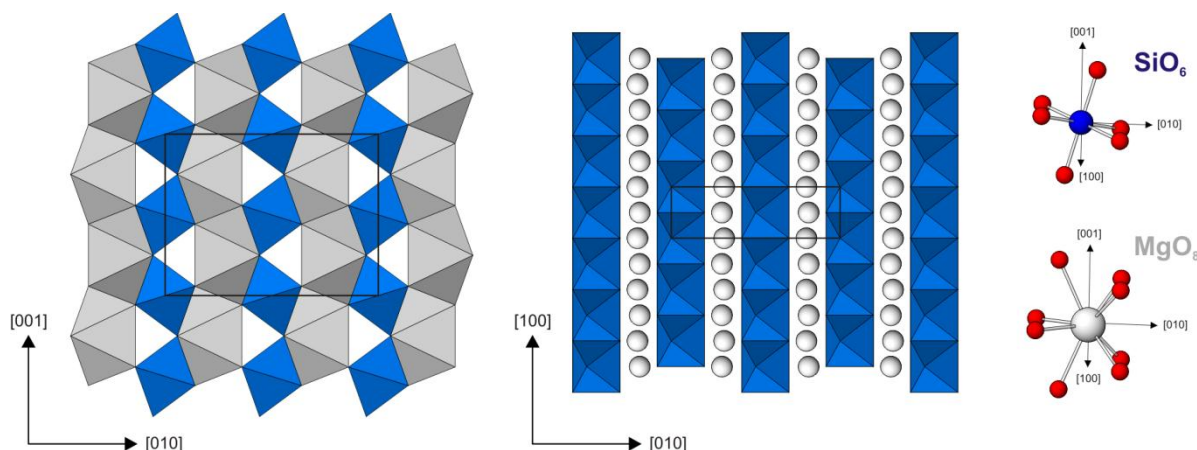


Fig. 1.1 Crystal structure of MgSiO_3 post-perovskite. Mg atoms and polyhedra are shown in grey, Si – in blue and O – in red.

Being normal to the shortest lattice repeat, (100) represents the most densely packed atomic plane. In the post-perovskite, there are only two {100} atomic layers (per unit length) which are geometrically identical and shifted from each other by $\frac{1}{2}[010]$ in accord with the symmetry produced by the C -lattice. Presence of two equivalent atomic layers

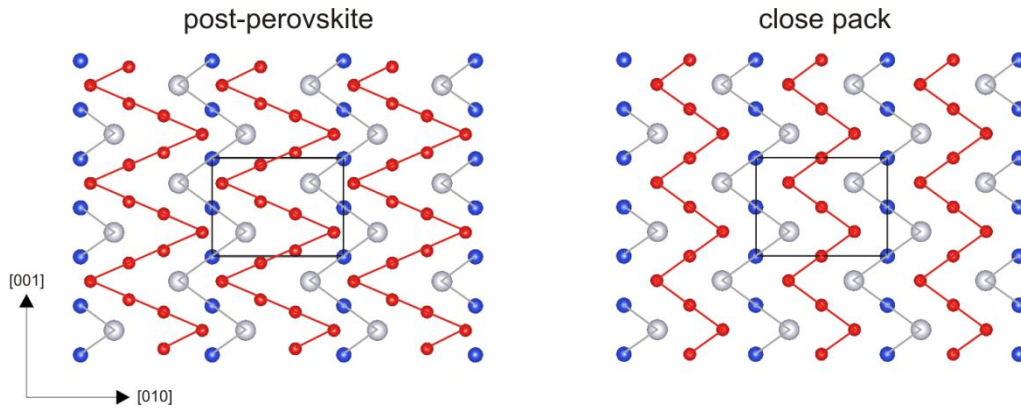


Fig. 1.2 Atomic (100) monolayer of the post-perovskite compared with orthorhombically distorted close pack layer. Zigzags of cations and anions are highlighted with grey and red, respectively; unit cell is shown with black rectangular.

with pseudo trigonal features, shifted from each other, implies a relation with the hexagonal close packed (*hcp*) structure. However, the specific arrangement of atoms with different nature within each (100) layer (Fig. 1.2) as well as the location of these layers with respect to each other excludes the possibility to describe the post-perovskite structure in terms of a distorted close pack formed by anions or/and cations.

1.2 Perovskite → post-perovskite phase transition

Transition boundary

The first experimental evidence of MgSiO_3 post-perovskite phase transition (Murakami *et al.* 2004) was detected in a laser-heated diamond anvil cell (LHDAC) at P - T conditions in excess of 125 GPa and 2500 K (Pt scale by Jamieson *et al.* (1982)). The transition was shown to be reversible at 101 GPa and 2200 K, however, a specific Clapeyron slope was not properly constrained. Simultaneously, the existence of this new phase was confirmed by *ab initio* simulations (Oganov and Ono 2004, Tsuchiya *et al.* 2004a). Further, the transition boundary in pure MgSiO_3 was experimentally determined (Ono and Oganov 2005, Hirose *et al.* 2006a) based on Pt (Jamieson *et al.* 1982; Holmes *et al.* 1989), MgO (Speziale *et al.* 2001) and Au (Heinz and Jeanloz 1984; Shim *et al.* 2002; Tsuchiya 2003) pressure standards (Fig. 1.3). The transition pressures reported from

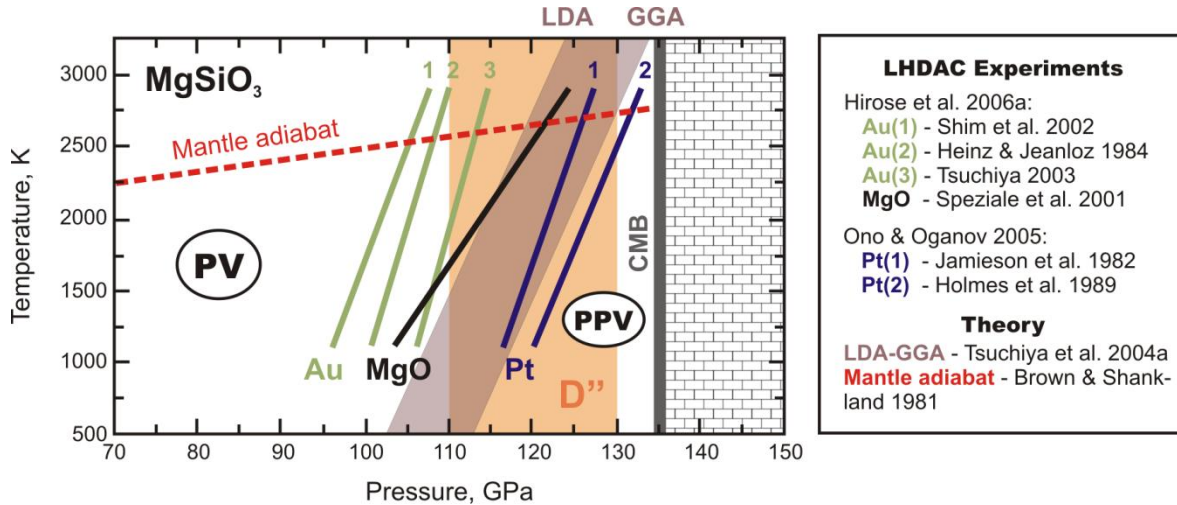


Fig. 1.3 Perovskite \rightarrow post-perovskite transition boundaries observed experimentally (Hirose et al. 2006a; Ono and Oganov 2005) with different pressure scales and calculated from the first principles (Tsuchiya et al. 2004a) for pure MgSiO_3 . Range of D'' discontinuity is taken from Cobden et al. (2015).

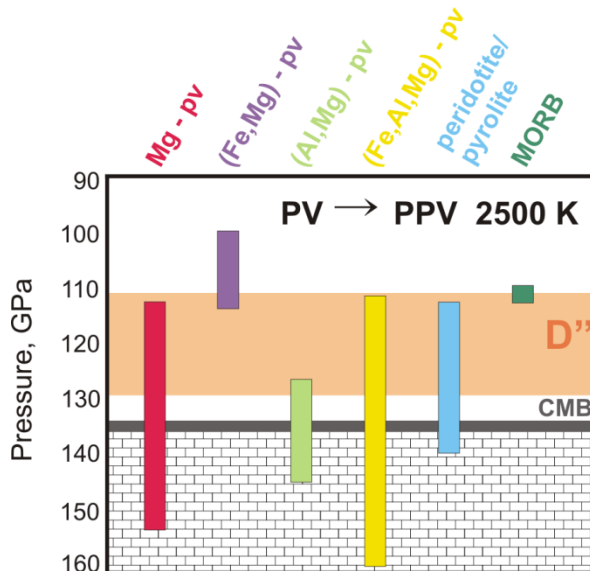


Fig. 1.4 Pressure ranges of the silicate perovskite \rightarrow post-perovskite phase transitions observed experimentally at 2500 K for various compositions compared to the pressure conditions of the D'' layer. The diagram is built based on the overview of experimental data published in Cobden et al. (2015).

different pressure scales vary by more than 20 GPa. Even while using a given standard, different equations of state (EoSs) of the calibration material may result in some discrepancies in the P - T conditions determined (see Fig. 1.3 for Au and Pt scales). In overall, the transition pressures estimated with Pt are higher than those defined with Au but both are characterized by the similar Clapeyron slope of ~ 6 - 7 MPa/K (Ono and Oganov

2005, Hirose *et al.* 2006a), close to that suggested to be necessary for the solid-solid phase transition accounting for the observed D'' discontinuity (Sidorin *et al.* 1999). At the same time, MgO standard provides intermediate pressures but with a higher dP/dT gradient of the phase boundary close to 11.5 MPa/K (Hirose *et al.* 2006a).

Complementary to the high-pressure experiments (Ono and Oganov 2005, Hirose *et al.* 2006a), the Clapeyron slope for the PV \rightarrow PPV transformation in pure Mg-silicate was computed from the first-principles by Tsuchiya *et al.* (2004a) within the quasiharmonic approximation (QHA) framework (Carrier *et al.* 2008, Wallace 1972). The estimated range of the phase transition, with the lower pressure frontier from LDA (Perdew and Zunger 1981) and the higher – from GGA (Perdew *et al.* 1996) exchange correlation functionals, is indicated with a shaded area on Fig. 1.3. The calculated Clapeyron slope is ~ 7.5 MPa/K, consistent with those derived from high-pressure experiments with Pt and Au scales. Although the uncertainties in the defined phase transition boundaries are quite large both for experimental and theoretical techniques, superposing the overall results with the estimated mantle adiabat (Brown and Shankland 1981) suggests that the phase transition in MgSiO₃ is likely associated with the D'' discontinuity at ~ 120 GPa and 2500 K (Fig. 1.3) as it was reported from the very first experiments by Murakami *et al.* (2004).

Besides pure MgSiO₃, Fe- and Al-bearing compositions have been extensively studied in order to estimate compositional effects on the PV \rightarrow PPV transition boundary (Fig. 1.4). Experiments and theoretical simulations performed on binary (Mg_{1-x}Fe_x)SiO₃ system indicate that incorporation of Fe²⁺ as Mg substituent significantly decreases the transition pressure (Mao *et al.* 2004, 2005; Caracas and Cohen 2005; Zhang *et al.* 2016). Thus, experimental measurements on the silicate systems with compositions close to (Mg_{0.9}Fe_{0.1})SiO₃ consistently provide the onset of PV \rightarrow PPV phase transition at pressures and temperatures about 111 GPa and 2500 K (Shieh *et al.* 2006; Catalli *et al.* 2009; Metsue and Tsuchiya 2012). At the same time, most of theoretical (Akber-Knutson *et al.* 2005; Caracas and Cohen 2005; Zhang and Oganov 2006) and experimental (Tateno *et al.* 2005) studies, except for *ab initio* simulations by Tsuchiya and Tsuchiya (2008), indicate that Al³⁺ has the opposite effect stabilizing perovskite phase at higher pressures (Fig. 1.4). Accounting for simultaneous presence of both Fe and Al impurities, experimental studies of ternary (Mg_{1-x}Fe_x)(Si_{1-x}Al_x)O₃ systems indicate a widely varying transition region from +20 GPa above to -25 GPa below the CMB (Nishio-Hamane *et al.* 2007; Catalli *et al.* 2009; Andrault *et al.* 2010; Shieh *et al.* 2011).

The post-perovskite phase transition was also experimentally observed in more complex multi-phase systems compositionally close to natural peridotitic/pyrolitic mantle and Mid-Ocean Ridge Basalt (MORB). Most observations of PV \rightarrow PPV transformation in pyrolitic compositions occur in a relatively narrow transition region of $\sim 113 - 127$ GPa at 2500 K (Murakami *et al.* 2005; Ono and Oganov 2005; Ohta *et al.* 2008; Sinmyo *et al.* 2011). However, study by Groholski *et al.* (2012) demonstrates that the transition boundary in pyrolite may be shifted up to 140 GPa. Since most of these studies were based on gold pressure standards, the calibration effect would not account for more than ~ 5 GPa of discrepancy and the origin of the latest is still debated. Experiments performed for compositions close to MORB (Hirose *et al.* 2005; Ohta *et al.* 2008; Grocholski *et al.* 2012), corresponding to the component of subducted slabs which may penetrate into the lower mantle (Tackley 2011), consistently report the onset of the phase transition between ~ 107 and 114 GPa at 2500 K (Fig. 1.4).

In summary, the experimental data illustrated on (Fig. 1.4) clearly demonstrates that P - T conditions and thickness of the phase boundary represent a complex function of chemical composition, which, in turn, remains obscure due to the uncertainties in the thermochemical state of the lowermost mantle (Grocholski *et al.* 2012).

Mechanism of the phase transition

As suggested by Tsuchiya *et al.* (2004a), a structural relation between perovskite ($Pbnm$) and post-perovskite ($Cmcm$) phases can be seen from the compressive behavior of $MgSiO_3$ perovskite (Wetzcovitch *et al.* 1995), illustrated on the upper panel of Fig. 1.5. In the perovskite structure under an applied strain ε_6 , the angles between octahedral edges bisected by (110) plane decrease faster than other similar angles. With sufficiently large strain ($\varepsilon_6 > 0.3$) these angles vanish and give rise to the layered post-perovskite structure. However, a uniform transformation by simply closing the corners between Si-octahedra was demonstrated to be energetically less favorable than the transition through intermediate phases built by successive [101](010) stacking faults (Zahn 2011; Oganov *et al.* 2005). During this process, the shear strain decreasing the angles between octahedral edges is expected to enhance the onset of phase transformation. The reverse PPV \rightarrow PV transformation is believed to occur through accumulation of $\langle 110 \rangle \{ 110 \}$ stacking faults in post-perovskite (Oganov *et al.* 2005) as illustrated on Fig. 1.5.

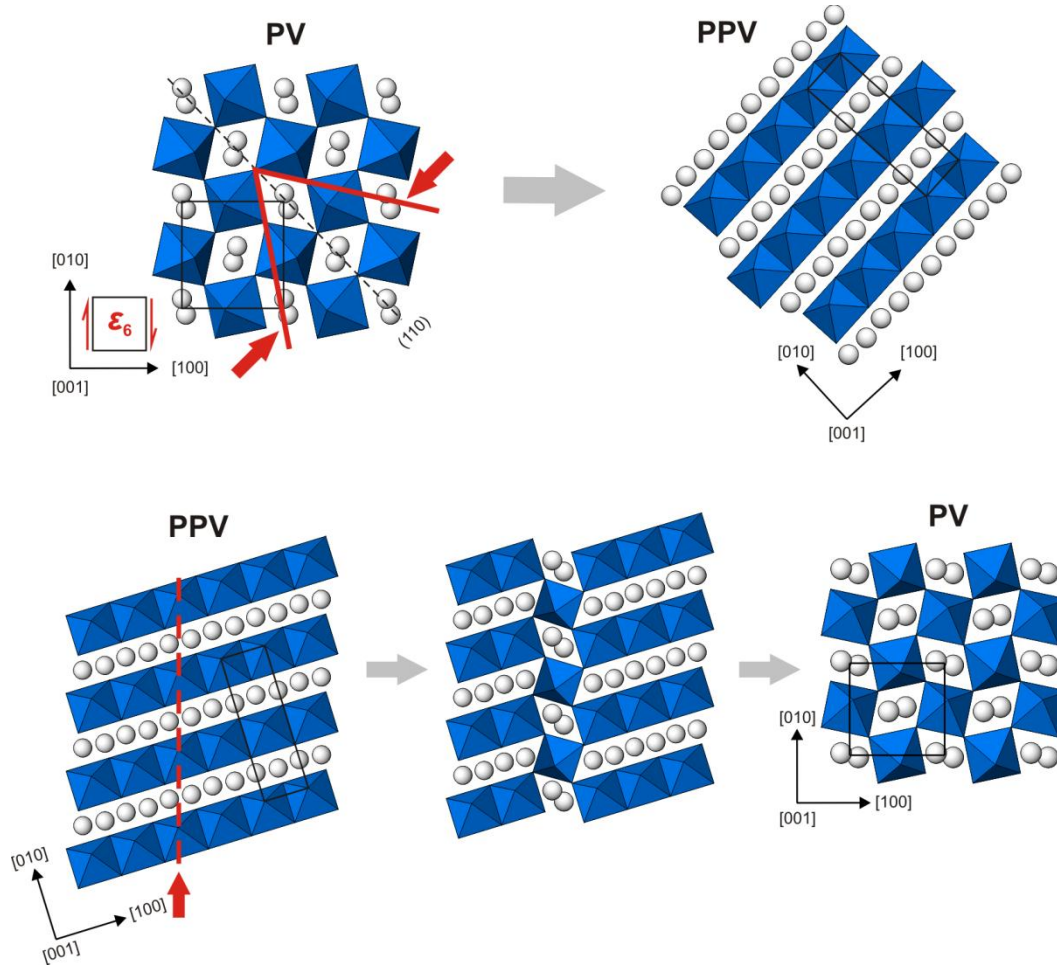


Fig. 1.5 Structural relation between the orthorhombic perovskite (bridgmanite) and post-perovskite phases. Transformation mechanism on the upper panel proposed by Tsuchiya *et al.* (2004a), on the lower one – by Oganov *et al.* (2005)

According to the transition mechanisms described above (Tsuchiya *et al.* 2004a; Oganov *et al.* 2005), the post-perovskite structure inherits [001] direction of the perovskite (Fig.1.5), while $[100]^{\text{PV}}$ and $[010]^{\text{PV}}$ directions correspond to $\langle 110 \rangle^{\text{PPV}}$ vectors in the post-perovskite reference (Fig. 1.5). Relying on this simple structural relation between the two phases, one can expect the appearance of a local structure resembling post-perovskite geometry inside $[010](100)$ and $[100](010)$ dislocation cores in perovskite; and, by analogy, - resembling perovskite in $\langle 110 \rangle\{110\}$ dislocation cores in the post-perovskite. Indeed, such a kind of dislocation cores was reported for dissociated $[010](100)$ and $[010](100)$ edge dislocations in MgSiO_3 bridgmanite (Hirel *et al.* 2014; 2016). For these

dislocations, stacking faults between the two partials look like a lamella of the distorted post-perovskite structure where octahedra are linked by edges in one direction, by corners in another one and don't interconnect in the third direction, forming a nucleus of 2D layers. Thus, dislocations in perovskite might prompt the instant of the phase transition into post-perovskite and vice versa. However, up to now there is no evidence on atomic structure of $\langle 110 \rangle$ dislocation cores in post-perovskite, possibly playing an important role for the PPV \rightarrow PV transformation process.

1.3 Stability of post-perovskite at extreme pressures

Besides the Earth's CMB, several studies suggest the mantle of some extra-solar large rocky planets (if differentiation into silicate mantle and metallic core takes place there) to be made mostly of the silicate post-perovskite phase (Stamenković *et al.* 2011; Tackley *et al.* 2013; Baraffe *et al.* 2014). The so-called super-Earths, *e.g.* in GJ876d (Rivera *et al.* 2005), CoRoT-7 (Queloz *et al.* 2009), Kepler-10b (Batalha *et al.* 2011) and some other planetary systems, are expected to have a density $\rho = 5.6 \pm 1.3 \text{ g/cm}^3$, very close to that of Earth, and radii of about twice the Earth radius. Based on these characteristics, pressures at the base of their mantles are expected to reach Tera Pascals (Valencia *et al.* 2006; Sotin *et al.* 2007). The interior dynamics of these planets causes a keen scientific interest nowadays and understanding of the post-perovskite plasticity may provide some insights into rheological processes taking place outside of the Solar System.

Taking into account the extreme P - T conditions relevant to the interior of super-Earths, only shock experimental techniques can be directly applied to investigate the stability field of the silicate post-perovskite phase there. Alternative experiments performed for isostructural low-pressures analogues and theoretical studies of the post-perovskite behavior under compression provide contradictory results and report several possible scenarios of phase transformations into the so-called post-PPV phases followed by their decomposition into oxides (Fig. 1.6). Thus, study of MnTiO_3 post-perovskite suggested its decomposition into MnO and orthorhombic MnTi_2O_5 (Okada *et al.* 2011), however, the precise crystal structure of the latest was not identified. Similarly, a gradual dissociation of MgSiO_3 post-perovskite into MgO (CsCl - type) and MgSi_2O_5 with small

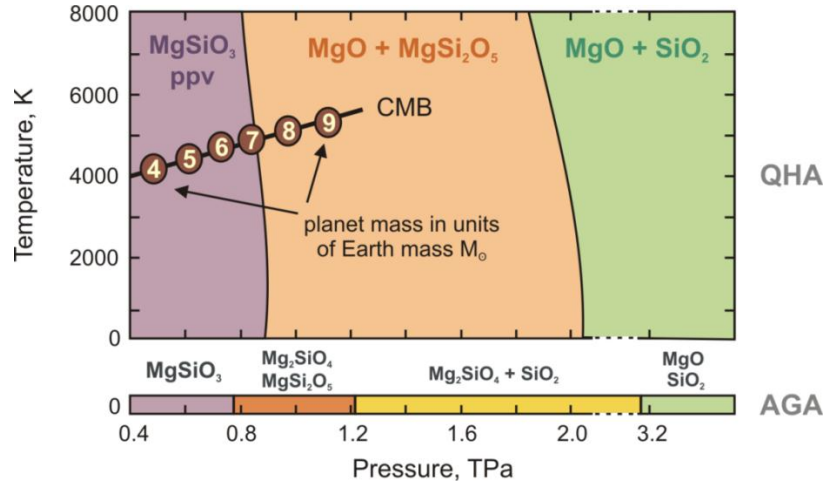


Fig. 1.6 Phase diagram of the two-stage (QHA by Umemoto and Wentzcovitch (2011)) and three-stage dissociation (AGA by Wu et al. (2014)) of $MgSiO_3$ PPV in comparison with the estimated P - T conditions at CMB of terrestrial exoplanets (Sotin et al. 2007).

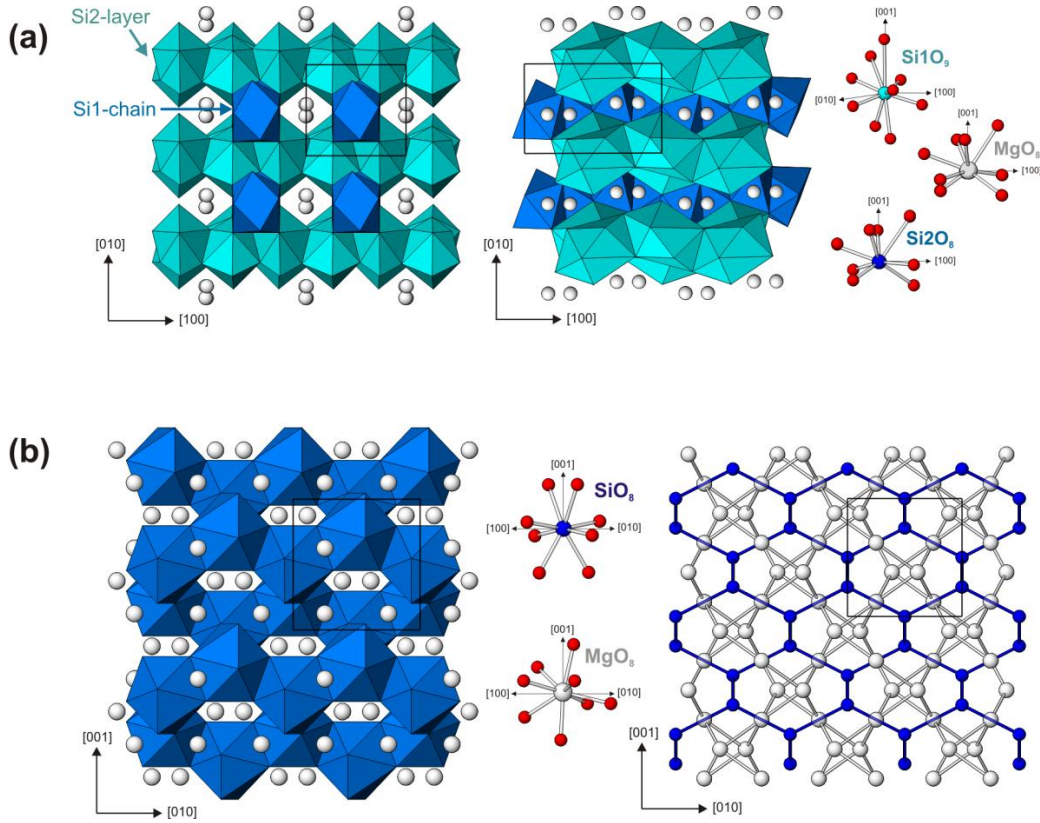


Fig. 1.7 (a) Monoclinic $MgSi_2O_5$ post-PPV ($P2_1/c$) observed by (Umemoto and Wentzcovitch 2011) and (Wu et al. 2014). (b) Tetragonal Mg_2SiO_4 post-PPV ($\bar{I}42d$) reported by (Wu et al. 2014). On the right panel anion sublattice is left out.

monoclinic distortions from the orthorhombic *Pbam* cell ($P2_1/c$, $a = 4.429 \text{ \AA}$, $b = 4.031 \text{ \AA}$, $c = 6.179 \text{ \AA}$, $\beta = 89.68^\circ$) was predicted at $\sim 0.9 \text{ TPa}$ by Umemoto and Wentzcovitch (2011) from the first-principles simulations within the quasiharmonic approximation (QHA) (Carrier *et al.* 2008, Wallace 1972). In MgSi_2O_5 , both Si and Mg atoms change their original coordination into denser 9- and 8-fold coordinated polyhedra (Fig. 1.7a) interconnected in such a way that 9-fold coordinated Si2 form (010) layers linked with each other by [100] chains made of 8-fold coordinated Si1. The empty [100] channels in this rigid Si network are filled by Mg atoms. The $P2_1/c$ post-PPV phase is shown to be stable up to pressures of $\sim 2.1 \text{ TPa}$ (Fig. 1.6) when it undergoes further decomposition into MgO (CsCl-type) and SiO_2 (Fe₂P-type) oxides.

Another theoretical study by Wu *et al.* (2014) based on adaptive genetic algorithm (AGA) confirms the appearance of MgSi_2O_5 ($P2_1/c$) post-PPV, however, the dissociation mechanism (Fig. 1.6) is shown to be more complex than the one proposed by Umemoto and Wentzcovitch (2011). At the first stage of the MgSiO_3 PPV decomposition at $\sim 0.77 \text{ TPa}$, MgSi_2O_5 ($P2_1/c$) is found to coexist with another high-pressure tetragonal phase Mg_2SiO_4 ($I\bar{4}2d$, $a = 4.5745 \text{ \AA}$, $b = 4.7006 \text{ \AA}$). In this structure, both Si and Mg are 8-fold coordinated and create a complex network made of 6-member corrugated rings penetrating into each other (Fig. 1.7b) in accord with the symmetry produced by the diamond d -plane. Under further compression, MgSi_2O_5 ($P2_1/c$) breaks down into SiO_2 (Fe₂P-type) and Mg_2SiO_4 ($I\bar{4}2d$) at $\sim 1.25 \text{ TPa}$, followed by gradual dissociation into MgO (CsCl-type) and SiO_2 (Fe₂P-type). The complete decomposition into oxides is expected to occur at $\sim 3.09 \text{ TPa}$, which notably exceeds the expected pressures in mantle of super Earth planets (Sotin *et al.* 2007).

Comparing the estimated internal pressures and temperatures of the large rocky planets (Valencia *et al.* 2006; Sotin *et al.* 2007) with the phase boundaries calculated using the QHA (Umemoto and Wentzcovitch 2011) and AGA (Wu *et al.* 2014), MgSiO_3 post-perovskite could be expected to remain stable in the mantles of super-Earths with masses smaller than $6\text{-}7M_\oplus$ (Fig. 1.6). Therefore, among the known planetary systems, transformation of MgSiO_3 post-perovskite into post-PPV phases possibly occurs in interior of big super Earths ($>7M_\oplus$) belonging to GJ876d (Rivera *et al.* 2005), while in the other systems, like CoRoT-7 (Queloz *et al.* 2009) and Kepler-10b (Batalha *et al.* 2011), post-perovskite would rather represent a major constituent of the silicate mantle down to the CMB.

1.4 Elasticity of silicate post-perovskite

The orthorhombic symmetry of post-perovskite results in the elastic stiffness tensor containing nine independent C_{ij} coefficients:

$$\begin{bmatrix} C_{11} & C_{12} & C_{13} & 0 & 0 & 0 \\ C_{12} & C_{22} & C_{23} & 0 & 0 & 0 \\ C_{13} & C_{23} & C_{33} & 0 & 0 & 0 \\ 0 & 0 & 0 & C_{44} & 0 & 0 \\ 0 & 0 & 0 & 0 & C_{55} & 0 \\ 0 & 0 & 0 & 0 & 0 & C_{66} \end{bmatrix} \quad (1.1)$$

Experimental measurements of elastic properties at P - T conditions relevant to the CMB are extremely challenging to perform and up to now there are no reports of elastic coefficients determined experimentally for the post-perovskite silicate phase. As an alternative to laboratory approach, several theoretical studies based on the first-principles simulations (Iitaka *et al.* 2004; Tsuchiya *et al.* 2004b, Oganov and Ono 2004; Liu *et al.* 2012) provide us some insights into athermal anisotropic elasticity of MgSiO_3 post-perovskite¹. Generally, all elastic moduli computed for the post-perovskite with LDA (Tsuchiya *et al.* 2004b, Iitaka *et al.* 2004; Caracas and Cohen 2005) are somewhat higher than those estimated using GGA (Oganov and Ono 2004; Carrez *et al.* 2007; Liu *et al.*

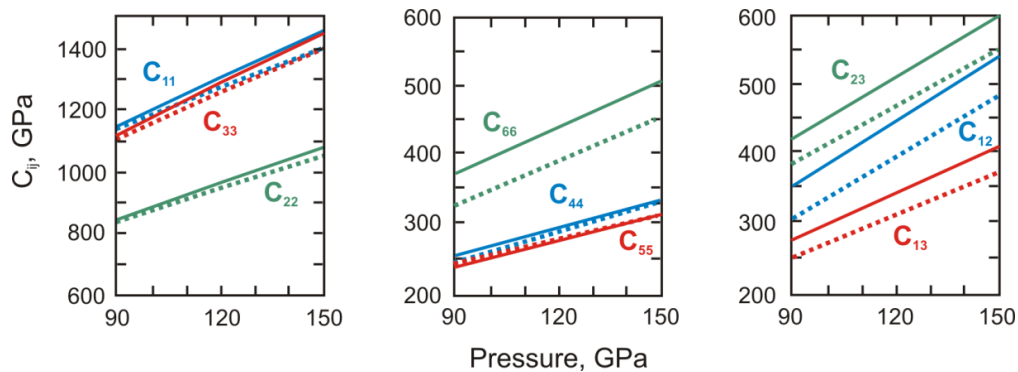


Fig. 1.8 Athermal elastic constants of MgSiO_3 post-perovskite computed from the first principles. Solid lines correspond to LDA simulations by Tsuchiya *et al.* (2004b); dotted lines – to GGA by Liu *et al.* (2012)

¹ Table with athermal elastic constants computed from the first principles at 120GPa is provided in Chapter 2

2012). Depending on the chosen exchange correlation functional (LDA or GGA), C_{66} , C_{12} , C_{13} and C_{23} differ within 15%, while other elastic coefficients C_{ij} are in a good agreement (Fig.1.8). Much lower values of the C_{22} coefficient compared to C_{11} and C_{33} (Fig. 1.9) indicate that the post-perovskite is much more compressible along the b –axis, normal to the structural layering (Fig. 1.1), than along the a and c -axis.

Studies of MgSiO_3 post-perovskite thermoelasticity based on the quasiharmonic approximation (QHA) (Wentzcovitch *et al.* 2006) and density functional molecular dynamics (DFT-MD) (Stackhouse and Brodholt 2007, Zhang *et al.* 2016) demonstrate that all elastic moduli are two orders of magnitude more sensitive to the changes in pressure (*i.e.* dC_{ij}/dP) than to the changes in temperature (dC_{ij}/dT). Recent *ab initio* simulations by (Zhang *et al.* 2016) in a wide range of pressures and temperatures indicate that incorporation of up to 20-25% of Fe^{2+} , Fe^{3+} and Al^{3+} into silicate post-perovskite at $T=2000$ K and $P=120$ GPa, close to that expected at the CMB, will result in an overall decrease of elastic moduli up to 10% without changing the intrinsic anisotropic character of the post-perovskite elasticity.

1.5 Plastic deformation of MgSiO_3 post-perovskite and its structural analogues

Seismic anisotropy of post-perovskite is not only linked to anisotropic elasticity resulting from the distinct layered structure. Seismological properties of crystalline aggregates depend also strongly on the development of crystal preferred orientation (CPO) mostly produced by dislocation creep. So far, the concept of easy slip system in the post-perovskite is poorly understood. Silicate PPV is only stable at very high P - T conditions and cannot be quenched to ambient pressure. Therefore, high-pressure experiments are limited to *in situ* XRD measurements of textures, from which one can only assume easy slip systems. Even though, the textures observed experimentally for MgSiO_3 and its close Ge-analogues lead to conflicting results (see Table 1.1). Thus, LHDAC experiments performed by Merkel *et al.* (2006, 2007) suggest a slip in (110) or/and (100), which seems to be consistent with theoretically predicted $\langle 110 \rangle \{ 110 \}$ by Oganov *et al.* (2005).

Table 1.1

Slip systems of MgSiO₃ post-perovskite and its structural analogues from high-pressure experiments and theoretical studies

Composition	Slip System	Method	Reference
(Mg, Fe)SiO ₃	(100) / {110}	LHDAC	Merkel <i>et al.</i> 2007
	(001)	LHDAC	Miyagi <i>et al.</i> 2010
	$[\bar{1}10](110)$	<i>ab initio</i> metadynamics	Oganov <i>et al.</i> 2005
	[100](010) [001](010)	<i>ab initio</i> GSF & PN model	Carrez <i>et al.</i> 2007a,b
	[001](010)	<i>ab initio</i> PN model, VPSC	Metsue <i>et al.</i> 2009
	[100](001)	<i>ab initio</i> GSF	Metsue and Tsuchiya 2013
MgGeO ₃	(100) / {110}	LHDAC	Merkel <i>et al.</i> 2006
	(100) – transf. Opx (001) – deform.	LHDAC	Okada <i>et al.</i> 2010
	(100) – transf. Opx (001) – deform.	LHDAC	Miyagi <i>et al.</i> 2011
	$[\bar{1}10](110)$ / (001) [010](001)	LHDAC <i>In-situ</i> 3D XRD	Nisr <i>et al.</i> 2012
	[100](001)	<i>ab initio</i> PN model VPSC	Metsue <i>et al.</i> 2009
MnGeO ₃	(001)	LHDAC	Hirose <i>et al.</i> 2010
CaPtO ₃	[100](010)	D-DIA, TEM	McCormack <i>et al.</i> 2011

Table 1.1 continued

	[100](010) [u0w](010)	Cubic anvil apparatus, TEM	Miyajima <i>et al.</i> 2006
	[100](010) [001](010)	D-DIA, TEM	Miyajima and Walte 2009
	[100](010) [001](010) {110} twins	LHDAC, TEM	Miyajima <i>et al.</i> 2010
	[100](010)	D-DIA, TEM	Walte <i>et al.</i> 2007
	(100) – transf. PV (010) – deformation	D-DIA, SEM-EBSD	Walte <i>et al.</i> 2009
CaIrO ₃	(010)	DAC, <i>In-situ</i> XRD	Niwa <i>et al.</i> 2007
	(010) {110} twins	DAC, TEM	Niwa <i>et al.</i> 2012
	[100](010)	Kawai-type apparatus, SEM- EBSD	Yamazaki <i>et al.</i> 2006
	[100](010)	D-DIA, <i>In-situ</i> XRD	Miyagi <i>et al.</i> 2008
	[100](010)	D-DIA, <i>In-situ</i> XRD, SEM-EBSD	Hunt <i>et al.</i> 2016
	[001](010)	<i>ab initio</i> PN model, VPSC	Metsue <i>et al.</i> 2009

However, during similar experiments by Miyagi *et al.* (2010, 2011), a strong development of (001) textures is observed. At the same time, Nisr *et al.* (2012) reports appearance of both (110) and (001) in MgGeO₃. Under similar conditions, MnGeO₃ (Hirose *et al.* 2010) produces textures consistent with slip in (001). Further experimental studies by Miyagi *et al.* (2011), Okada *et al.* (2010) and Walte *et al.* (2009) suggest that slip in (100) plane, similar to that observed by Merkel *et al.* (2006, 2007) can be rather classified as a transformation texture (from orthopyroxene), while (001) is likely produced during

deformation of PPV phase. Dominant (001) slip in MgSiO_3 and MgGeO_3 is consistent with the results from *ab initio* simulations of generalized stacking faults (GSF) by Metsue *et al.* (2013). This theoretical study also indicates that incorporation of Fe^{2+} decreases the strength of all slip systems without changing the general character of plastic anisotropy. Another numerical modeling based on the Peierls-Nabarro (PN) model (Peierls, 1940; Nabarro 1947) performed for MgSiO_3 by Carrez *et al.* (2007a,b) and Metsue *et al.* (2009), rather emphasizes the importance of dislocation glide in (010) parallel to the structural layering.

Alternatively to silicate and germanate compositions, use of analogue materials stable at ambient pressures allows direct TEM analysis of recovered samples. Therefore, not surprisingly, CaIrO_3 appears to be very attractive to perform well-controlled deformation experiments (see Table 1.1). In contrast to high-pressure MgSiO_3 and MgGeO_3 phases, both experimental and theoretical studies of CaIrO_3 consistently report the presence of [100](010) and [001](010) dislocations and (010) textures, independently from the applied deformation and analytical techniques (see Table 1.1). It's also interesting to note, that appearance of {110} twin domains in CaIrO_3 is systematically reported only during DAC experiments (Miyajima *et al.* 2010, Nawa *et al.* 2012). This implies that the observed {110} textures in MgSiO_3 and MgGeO_3 (Merkel *et al.* 2006, 2007) might not represent a transformation texture as suggested by Miyagi *et al.* (2011) and Okada *et al.* (2010), but instead could result from deformation through twinning due to high stress and strain rates produced by DAC.

However, before direct extrapolation of plastic behavior inferred for analogue materials into silicate compound, one should take into account that in terms of bonding (Hustoft *et al.* 2008, Metsue *et al.* 2009; Tsuchiya and Tsuchiya 2007), characteristics of CaIrO_3 differ from those in MgSiO_3 and MgGeO_3 (Kubo *et al.* 2008; Hustoft *et al.* 2008). First-principles studies also indicate that anisotropic elasticity (Tsuchiya and Tsuchiya 2007) and plasticity (Metsue *et al.* 2009) in CaIrO_3 are not the same as in silicate post-perovskite. Even so, being very close in terms of bond strength to MgGeO_3 and not to CaIrO_3 , MgSiO_3 may produce [001](010) CPO, remarkably similar to that in CaIrO_3 , and different from the expected [100](001) texture in germanates (Metsue *et al.* 2009).

Summarizing the available experimental and theoretical results (see Table 1.1), we are clearly far from understanding plasticity of both monocrystalline and polycrystalline

silicate post-perovskite. The only clear answer is provided for the low-pressure analogue CaIrO_3 . However, there is still no plausible definition of good isostructural analogues of MgSiO_3 post-perovskite, accounting for bond strength contrast controlling plastic anisotropy in monocrystalline material. This implies that experimental observations and theoretical predictions made for PPV low pressure analogues can not necessarily address rheology of the lowermost mantle.

CHAPTER 2

Models and Methods

Within the last forty years, atomic scale modeling has become a powerful tool for modeling physical properties of a wide range of materials. Theoretical modeling is especially valuable when performing well-controlled experiments at relevant P - T conditions, strain rates *etc.* is extremely challenging or simply impossible. The aim of this chapter is to describe the basic physical models of the two commonly used simulation techniques, employed in this work: *ab initio* atomic-scale calculations within the density functional theory (DFT) framework; and atomistic simulations based on classical interatomic potentials. The chapter also provides an outline of the technical methods used in this study for modeling planar and linear defects, including explicit description of the simulation cells geometries and of the computational setup used for modeling defects at the atomic scale.

2.1 Atomic scale modeling: methodology and computational setup

2.1.1 *Ab initio* calculations

Schrödinger equation

The total energy E of a system which consist of N electrons at positions r_i and M nuclei at positions R_i can be found by solving the (non relativistic and time independent) Schrödinger equation:

$$\hat{H} \Psi(r_1, r_2, \dots, r_N, R_1, R_2, \dots, R_M) = E \Psi(r_1, r_2, \dots, r_N, R_1, R_2, \dots, R_M), \quad (2.1)$$

where \hat{H} is the Hamiltonian operator and Ψ is the wave function. The Hamiltonian \hat{H} can be defined as combination of kinetic energy operator T and potential energy operator V :

$$\hat{H} = T_e + T_N + V_{ee} + V_{NN} + V_{eN}, \quad (2.2)$$

where T_e and T_N correspond to the kinetic energy of electrons and nuclei; V_{ee} , V_{NN} , V_{eN} - to the interaction energy between the electrons, the nuclei, and between electrons and nuclei, respectively. Despite the apparent simplicity of the Hamiltonian (2.2), solving the Schrödinger equation (2.1) is very difficult because of large $3N$ number of electronic coordinates. For an atomic system containing more than two electrons, it's impossible to obtain the exact wave function Ψ by solving the Schrödinger equation (2.1) without introducing some approximations.

Born-Oppenheimer approximation

The first basic assumption is known as Born-Oppenheimer or adiabatic approximation. It relies on the fact that electrons are much lighter than nuclei and, therefore, are characterized by higher velocities. Consequently, the kinetic energy of the nuclei are negligible with respect to those of electrons: $T_e \gg T_N$; thus, the T_N term can be neglected. Low mobility of nuclei allows assuming them stationary positioned and considering only electrons to behave as quantum particles, therefore, the interaction energy V_{NN} has a constant value E_{NN} , which does not play a role in solving the Schrödinger equation. Based on all these assumptions, the Hamiltonian (2.2) reduces to:

$$\hat{H} = T_e + V_{ee} + E_{NN} + V_{eN}. \quad (2.3)$$

The many electron Schrödinger equation can be further simplified while considering N single electron Schrödinger like equations, where each electron experiences an effective field of other electrons. At this point, the problem becomes one of finding suitable ways to define the effective electron interactions, and to describe the total wave function from the N single electron wave functions ψ_i with energy ϵ_i .

Density functional theory

The framework of density functional theory (DFT) was built by Hohenberg and Kohn (1964) based on two theorems: (i) that the external potential of a system of electrons is a unique functional of the electron density, and (ii) that the ground state and energy of the system is variational with respect to electron density. The energy of such a system can be written as:

$$E = E[\rho(r)] = \int V_{ext}(r)\rho(r)dr + F[\rho(r)], \quad (2.4)$$

where both the external potential V_{ext} and the “universal” functional F are functions of the electron density $\rho(r)$. The effective single electron approach, suggested by Kohn and Sham (1965), defines the total electron density as a sum over one-electron wavefunctions describing single non-interacting electrons moving in the mean field of other electrons. The electron density ρ at a given point r corresponds then to the sum of the probability of finding an electron from any of one-electron orbitals at that point.

The functional F , contributing to the total energy E (eq. 2.4) of the system can be decomposed into three parts:

$$F[\rho(r)] = T_s[\rho(r)] + E_H[\rho(r)] + E_{ex}[\rho(r)], \quad (2.5)$$

where T_s is a kinetic energy of an isolated electron; E_H – Coulomb interaction between the electronic density states related to positions r and r' ; and E_{ex} – the exchange correlation functional. The E_H term can be defined as:

$$E_H[\rho(r)] = \frac{1}{2} \int \frac{\rho(r)\rho(r')}{|r - r'|} d^3r d^3r'. \quad (2.6)$$

There is no general exact expression for the exchange-correlation functional E_{ex} in terms of the electronic density $\rho(r)$. The E_{ex} term is commonly defined by approximations described

in the next section. To compute the energy $E[\rho(r)]$ of the system, each one-electron equation should rely on the solutions of all the other equations, therefore, they all are solved together using a self-consistent approach.

Approximations for the exchange-correlation functional

Approximating the exchange-correlation functional is the only inaccuracy in DFT that does not arise from its numerical implementation. The Local Density Approximation (LDA) introduced by Kohn and Sham (1965) represents a very simple and accurate approximation. Within the LDA approach, the energy arising from exchange and correlation at a point r of electron density ρ is equal to the exchange and correlation energy in a system of electrons with uniform density ρ :

$$E_{ex}^{LDA}[\rho] = \int \rho(r) \epsilon_{ex}[\rho(r)] dr, \quad (2.7)$$

where ϵ_{ex} is the energy of exchange and correlation of a uniform electron gas which can be accurately defined by quantum Monte Carlo methods. The LDA functional was parameterized by Perdew and co-workers (Perdew and Zunger 1981; Perdew and Wang 1992). The use of LDA for condensed matter is known to lead to over binding (total binding energy is too high) and to somewhat underestimated bond lengths. Consequently, elastic moduli computed with LDA can be expected to be somewhat overestimated (*e.g.* Fig. 1.8 and Table 2.2).

An effective refinement to LDA is to include a dependence on the local density gradient $\nabla\rho$ in the exchange correlation functional. This approach is known as the Generalized Gradient Approximation (GGA) and can be defined as:

$$E_{ex}^{GGA}[\rho] = \int \rho(r) \epsilon_{ex}[\rho(r), \nabla\rho(r)] dr. \quad (2.8)$$

In this equation, the functional $\epsilon_{ex}[\rho(r), \nabla\rho(r)]$, accounting for the local density gradient $\nabla\rho$, can be calculated in several ways. Common GGA parameterizations include PW91 (Wang and Perdew 1992) and PBE (Perdew *et al.* 1996). Compared to LDA, GGA formalism often leads to slight under binding, *i.e.* to energies that are lower and bonds that are longer.

Plane waves and pseudopotentials

In practice, performing DFT simulations requires introducing some additional “machinery” making it efficient. In periodic solids, the most common approach is using the concept of plane waves and pseudopotentials. A plane wave basis set is established to represent the one-electron Kohn-Sham orbitals. The wave functions of the latter have the same periodicity as the crystal lattice (Bloch’s theorem), which is essential for describing 3D periodic boundary conditions of the system, making it infinite. Representing the periodic wave functions (Bloch waves) in reciprocal space allows studying a single unit cell while sampling the one-electron wave functions with k -points over the first Brillouin zone (primitive cell of the reciprocal crystal lattice). In principle, this sampling should be infinite, however, practically, it’s not possible and, therefore, restricted to a finite number of k -points (dependent on the size of the system), sufficient to reach a reasonable convergence for the total energy of the system.

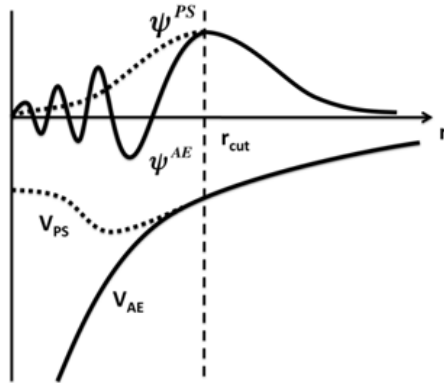


Fig. 2.1. Schematic illustration of a pseudo wavefunction ψ^{PS} and potential V_{PS} , compared to the corresponding all-electron (AE) functions.

The wavefunctions are characterized by the largest curvature close to the cores of atoms, therefore their explicit description in this region is computationally expensive. To reduce this effect, pseudopotentials are introduced to replace the potential energy of the interactions between the core and valence electrons which mainly determines the material properties. The core (effective ion) region is defined as the nucleus plus the inner atomic electrons and can be restricted to the zone with $r < r_{cut}$. Outside the core, *i.e.* in the region where $r > r_{cut}$, the pseudopotential wavefunction ψ^{PS} and potential V_{PS} matches the corresponding all-electron curvatures ψ^{AE} and V_{AE} (Fig.2.1). The most accurate approximation to handle the interactions between the nuclei and the electrons is projector

augmented wave (PAW) method developed by Blöchl (1994). It allows accounting for the orbitals of inner electrons (*i.e.* within the core) by using a linear transformation of the all electron wavefunctions into a pseudo wavefunction in the region $r < r_{cut}$. Other commonly used pseudopotentials, known as ultrasoft (US), are based on a generalized eigenvalue formalism (Vanderbilt 1990) and just smoothen the pseudo wavefunctions of the core. The US-potentials are therefore less accurate than PAW and the least time consuming. To define the number of plane waves needed to accurately describe the atomic system, the corresponding energy cutoff E_{cut} should be introduced.

Computational setup for modeling defects in MgSiO₃ PPV with VASP

In this work, *ab initio* calculations are performed based on the density-functional theory (DFT) within the generalized gradient approximation (GGA), with PW91 parameterisation as derived by Perdew and Wang (1992), and the all-electron projector augment-wave (PAW) method as implemented in the VASP code (Kresse and Furthmüller 1996; Blöchl 1994). The outmost core radius for Mg, Si and O are 2.0, 1.9 and 1.52 au, respectively. To achieve computational convergence, a plane-wave cutoff E_{cut} of 600 eV is applied. The first Brillouin zone is sampled using the Monkhorst-Pack scheme (Monkhorst and Pack 1976) with $8 \times 6 \times 1$ k -point grid to compute generalized planar fault energy (GPFE) for $\langle 110 \rangle \{110\}$ system in atomic arrays containing 180 atoms; with $10 \times 1 \times 1$ for $1b$ dipole simulation cells containing 360 atoms (employed for modelling [100] screw dislocations); and with $4 \times 1 \times 1$ grid for the $2b$ dipole cells containing 720 atoms (employed for calculating line tension Γ of [100] screw dislocations). The convergence energy is 10^{-3} meV/atom. Simulations are performed at a constant volume, corresponding to the bulk volume at 120 GPa.

2.1.2 Pairwise potential modeling

Atomic scale modeling from the first principles, relying on solving the Schrödinger equation, is a very accurate and, therefore, computationally expensive method. As such it is restricted to systems containing few hundred of atoms. This limitation often hampers using *ab initio* methods for direct atomic-scale modeling of dislocation cores in complex

materials since it requires designing large simulation cells containing thousands of atoms. Alternatively to the time consuming *ab initio* calculations, the total energy of an atomic array can be found through introducing parameterized functions that depend on the relative atomic positions. These functions are meant to mimic interatomic interactions with less complex function which leads to drastic saving in computer time and allows using large atomic arrays. This approach is widely used for atomistic modeling of minerals and other complex ionic materials (Lewis and Catlow 1985; Catlow and Price 1990; Price and Voadlo 1996; Wright 2003, *etc.*).

Interatomic interactions

In a system of N atoms, the total lattice energy U (the energy required to bring all atoms together from infinite separation) can be expressed as a Taylor expansion:

$$U = \sum_i^N U_i + \frac{1}{2} \sum_i^N \sum_j^N U_{ij} + \frac{1}{6} \sum_i^N \sum_j^N \sum_k^N U_{ijk} + \dots \quad (2.9)$$

In this expression, the first term represents the sum of the self-energies of all the atoms; the second one – the pairwise interaction between all the pairs of atoms distant by r , and so on. The interaction terms can be substituted by parameterized functions ϕ_{ij} , ϕ_{ijk} *etc.* For many systems, including MgSiO₃ perovskite (Oganov *et al.* 2000), good results can be achieved by truncating the Taylor expansion (2.9) at two-body terms ϕ_{ij} . However, in some systems, higher order interaction terms are needed. For instance, accounting for the three-body interactions ϕ_{ijk} is critical to accurately describe covalent bonds in rigid silicate and phosphate tetrahedra (*e.g.* in (Mg,Fe)₂SiO₄ olivine (Price *et al.* 1987) and Ca₅[PO₄]₃(F,Cl,OH) apatite (Rabone and De Leeuw 2006)).

The short range interactions of the pairwise term ϕ_{ij} can be summed to convergence only while considering interactions between atoms separated by less than a finite cutoff distance r_c . For Coulombic interactions, different technique of summation should be applied because of the slow rate of decay: in an infinite (periodic) solid the strength of the Coulombic interaction decreases as r^{-1} , while number of particles increases as r^3 . The most common approach to overcome this problem is to use Ewald summation (Ewald 1921). The sum is separated into two parts: for the region with $r \leq r_c$ and $r > r_c$, such as summing

the first one in real space and the second one in reciprocal space results in two convergent sums.

To describe the pairwise interactions ϕ_{ij} , there is a wide range of potential forms (the exhaustive description can be found in (Gale and Rohl 2003)). In this work we rely on the Buckingham potential form (Buckingham 1938), which consists of the exponential Born-Mayer potential (1932) accounting for the short range repulsion and the van der Waals attraction term. Based on the Buckingham potential, the lattice energy can be defined as:

$$U(r_{ij}) = \frac{q_i q_j}{r_{ij}} + A_{ij} \exp\left(-\frac{r_{ij}}{\rho_{ij}}\right) - \frac{C_{ij}}{r_{ij}^6}, \quad (2.10)$$

where the first term stands for long-range Coulombic interaction between i and j ions of charge q_i and q_j ; the second term describes short range repulsion parameterized by A_{ij} and ρ_{ij} ; and the last one corresponds to the van der Waals attraction controlled by a single C_{ij} parameter.

Pairwise potential parameterization

The parameterization used in this work was previously derived by (Oganov *et al.* 2000) for MgSiO₃ perovskite (bridgmanite). The corresponding A_{ij} , ρ_{ij} and C_{ij} coefficients for Mg-O, Si-O and O-O interactions are provided in Table 2.1.

Table 2.1

Parameterization of the Buckingham potential for MgSiO₃ by Oganov et al. (2000)

Bond ij	A_{ij} (eV)	ρ_{ij} (Å)	C_{ij} (eV·Å ⁻⁶)
Mg-O	1041.435	0.2866	-
Si-O	1137.028	0.2827	-
O-O	2023.8	0.2674	13.83

Based on this parameterization, the calculated ground state properties (structural parameters and elastic stiffness coefficients C_{ij}) of MgSiO₃ post-perovskite at $P = 120$ GPa and $T = 0$ K are provided in Table 2.2. The a and b parameters computed with the potential model are slightly overestimated in comparison with experimental data and DFT

Table 2.2

Lattice parameters (in Å), elastic constants C_{ij} , bulk and shear moduli B and G (in GPa) of $MgSiO_3$ post-perovskite calculated at 120 GPa and 0 K using the potential model by (Oganov et al. 2000) compared with those from previous DFT and experimental studies. Difference with DFT values is provided in brackets

	Potential	GGA ¹	GGA ²	LDA ³	LDA ⁴	Exp ⁵
a	2.521 (2-3%)	2.474	2.474	2.455	2.462	2.456
b	8.124 (~1%)	8.121	8.112	8.051	8.053	8.042
c	6.050 (~1%)	6.138	6.139	6.099	6.108	6.093
C_{11}	1118 (9-15%)	1252	1225	1270	1308	
C_{22}	781 (16-19%)	929	928	937	968	
C_{33}	1062 (12-18%)	1233	1211	1264	1298	
C_{12}	509 (15-24%)	414	409	425	444	
C_{13}	410 (19-26%)	325	328	329	343	
C_{23}	601 (19-26%)	478	484	493	507	
C_{44}	286 (~3%)	277	281	291	295	
C_{55}	119 (43-54%)	266	260	264	278	
C_{66}	256 (37-42%)	408	404	412	439	
B^*	667 (1-6%)	647	645	660	681	
G^*	228 (41-51%)	327	332	322	344	

¹Oganov and Ono (2004); ²Carrez et al. (2007a); ³Iitaka et al. (2004); ⁴Tsuchiya et al. (2004a,b);

⁵Murakami et al. (2004); * Voigt notation

calculations, while the c parameter is slightly underestimated. In general, all structural characteristics (including the unit cell volume) are in good agreement with previous experimental and theoretical data (the differences do not exceed 3%). The elastic C_{ij} tensor provided by the potential model is in a reasonable agreement with the available literature data. Generally, all non diagonal components are about 20% stiffer, while all diagonal components are about 15% softer, except C_{55} and C_{66} which differ by 40-50% from the corresponding DFT values (Table 2.2).

Reasonable agreement of athermal ground state properties with previous DFT and experimental studies (Table 2.2) makes the potential model by Oganov *et al.* (2000) promising for atomic scale modeling of MgSiO_3 post-perovskite. However, modeling plasticity and defects requires transferability of the potential to reproduce atomic configurations far from equilibrium where the potential was fitted. In order to validate the chosen parameterization for dislocation modeling, its ability to reproduce *ab initio* calculations of γ -lines is examined in Chapter 3.

Computational setup for modeling defects in MgSiO_3 PPV with LAMMPS

In this work, atomistic modeling of defects in MgSiO_3 post-perovskite is performed using the Buckingham form of a pairwise potential derived by Oganov *et al.* (2000) for MgSiO_3 bridgmanite (see eq. 2.10; Table 2.1) with the potential short range cut off distance $r_c = 12 \text{ \AA}$. Molecular statics simulations are carried out at $P = 120 \text{ GPa}$ and constant volume (corresponding to the volume of the perfect crystal) with the program package LAMMPS (Plimpton 1995), which relies on Ewald summation methods for Coulombic interactions. Energy minimization is performed using a conjugate-gradient (*cg*) algorithm (Lewis and van de Geijn 1993) followed by a Hessian-free truncated Newton (*hftn*) algorithm (Martens 2010) until the maximum force on atom drops below 10^{-9} eV/\AA ($1.602 \cdot 10^{-18} \text{ N}$).

2.1.3 Nudged elastic band method

Nudged elastic band (NEB) is an efficient method for searching the minimum energy path between a given initial and final state of transition (Henkelman and Jonsson 2000; Henkelman *et al.* 2008; Nakano 2008). This method is widely used to investigate diffusion

and absorption in crystals and at crystal surfaces (Wardle *et al.* 2006; Krashennnikov *et al.* 2009); and, more importantly for this study, to determine a path of a straight dislocation moving from one Peierls valley to the next one and the associated energy barrier (Rodney and Proville 2009; Pizzagalli *et al.* 2008a).

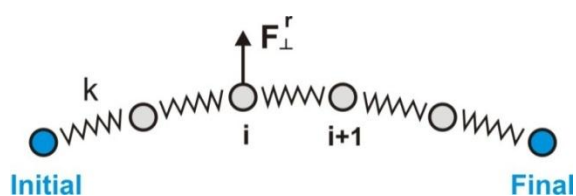


Fig. 2.2. Schematic illustration of a set of intermediate images bonded together with springs. The force component normal to the reaction path is indicated as F_{\perp}^r .

To employ this method, the exact atomic configurations of initial and final state should be known. The MEP between them will be found by constructing the set of images (replicas) of the system, typically on the order of 10-20. The initial guess of the path can be built as a linear interpolation of intermediate configurations. All configurations are bonded with springs (Fig.2.2) and the whole band acts as an elastic chain. As such, the intermediate images are always constrained to remain between the configurations that precede and follow them.

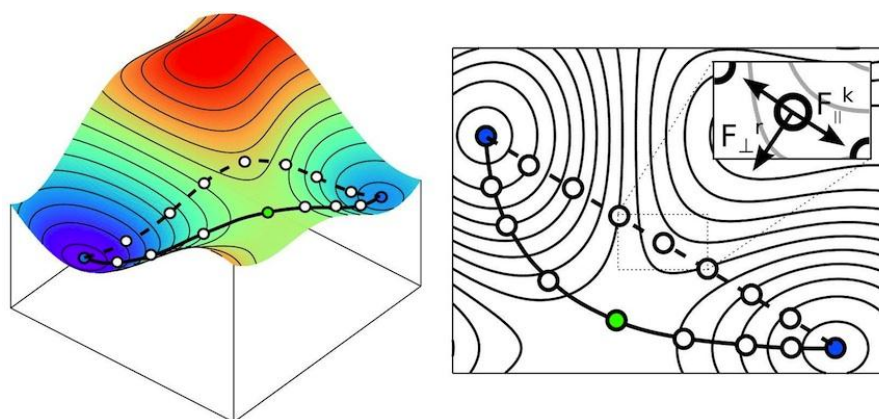


Fig. 2.3. Schematic illustration of the NEB calculation principle. Right side represents 3D energy landscape with the initial guess of the path (dashed line) and the final MEP (solid line) between the two minimum energy configurations located in the blue valleys. The left panel corresponds to the 2D projection of this energy landscape. Spring forces acting along the path and the force component normal to the path are indicated as F_{\parallel}^k and F_{\perp}^r , respectively. The picture is taken from Kraych (2016).

Optimization of the band involves minimization of the force acting on the images (Fig. 2.3). During NEB calculations, a force projection along the path is considered in such a way, that true forces F_{\perp}^r acting normally to the band do not affect the distribution of images along the MEP; and the spring forces F_{\parallel}^k do not interfere with the convergence of the band to the MEP, *i.e.* only control the spacing of the images along the path. The NEB calculation stops when the sum of these forces drops below a given convergence criterion.

In this study, the NEB simulations are performed for [100](010) screw dislocations in conjunction with the chosen pairwise potential (Oganov *et al.* 2000) via fire damped dynamics (Bitzek *et al.* 2006), as required by the minimization procedure implemented in LAMMPS. The MEP is sampled with 24 points (configuration images) which are bounded with a spring constant of 0.1 eV/Å ($1.602 \cdot 10^{-10}$ N). The force convergence criterion is taken as 10^{-3} eV/Å ($1.602 \cdot 10^{-12}$ N).

2.2 Atomistic modeling of planar defects

2.2.1 Generalized stacking faults

The calculation of generalized stacking faults (GSF), also called γ -surfaces, represents a first powerful approach to crystal plasticity (Vitek 1968). By application of a rigid body shear to a crystal structure followed by excess energy calculations, it is possible to identify easy shear paths. Further full atomistic modeling of the actual 3D structure of dislocations cores requires using large atomic arrays which are often beyond computational capabilities of the first principles calculations (see section 2.1.1). One can overcome this limitation while using empirical pairwise potentials (see section 2.1.2). The use of these potentials fitted against equilibrium properties must be validated in case of plasticity studies which involve atomic configurations far from equilibrium (Zimmerman *et al.* 2000; Godet *et al.* 2003; Carrez *et al.* 2008). In this work, the transferability of the pairwise potential derived by Oganov *et al.* (2000) is examined for modeling defects in MgSiO₃ post-perovskite by computing the GSF excess energies and comparing them with previous DFT calculations.

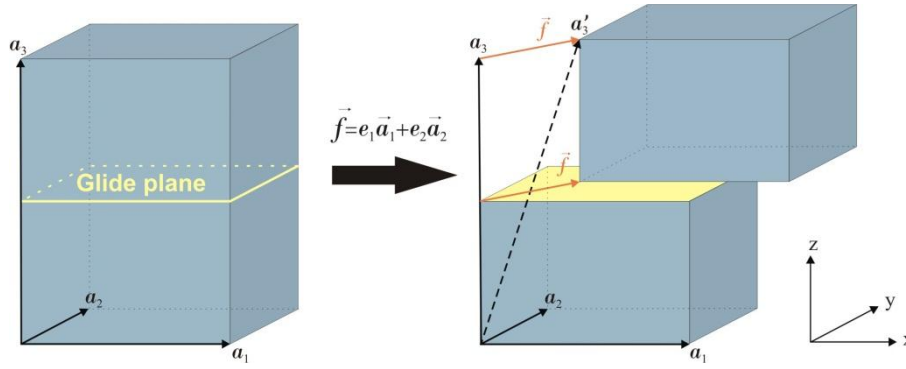


Fig. 2.4. Geometry of atomic systems designed for γ -surface calculations.

The excess energies γ , corresponding to the energy cost (per unit area) resulting from a rigid-body shear, are calculated by displacing the upper part of a perfect crystal over the lower part across a chosen (hkl) slip plane (Fig. 2.4). Simulations are performed for fully periodic atomic arrays built on three lattice vectors a_1 , a_2 and a_3 . The supercells are oriented in such a way that the (hkl) stacking fault plane of interest is normal to the Cartesian z direction (Fig. 2.4). It should be noted, that in complex materials there could be several nonequivalent geometric locations of a slip plane with a given (hkl) index which distort different atomic bonds. All possible configurations of slip planes in the post-perovskite structure are described in detail in Chapter 3. In order to keep a periodic boundary condition in a simulation cell containing a stacking fault, the lattice vector a_3 is given an additional component $\vec{f} = e_1\vec{a}_1 + e_2\vec{a}_2$, corresponding to the applied shear displacement (Fig. 2.4). Using a 5% increment of displacement e_i , the resolution of the energy landscape corresponds to 400 calculation points. After shearing the upper part, atomic relaxations are allowed along the direction normal to the glide plane, *i.e.* along z , exclusively. Absence of atomic relaxations parallel to the glide plane allows avoiding spurious recovery of the perfect crystal geometry during energy minimization. The optimum size of a simulation supercell along the z direction is found to be about 70 Å, which is large enough to allow relaxation of atoms close to the slip plane and to prevent the effect of atomic distortions on the boundary condition. Typical orthorhombic simulation supercell contains about 1500-2000 atoms. The energy minimization is performed at constant volume, corresponding to the ground state volume of a perfect

crystal under the given external pressure field of 120 GPa using the computational setup described in the section 2.1.2.

Based on the γ -surface excess energies, one can estimate the ideal shear stress (ISS), *i.e.* the upper limit of the stress that a perfect crystal can sustain (Paxton *et al.* 1995), as the absolute maximum of the γ -surface energies derivatives relative to the applied shear.

2.2.2 Twinning energy landscape

Deformation twinning at atomic scale is commonly modeled through computing twinning energy landscapes, also called generalized planar fault energy (GPFE). This energy landscape results from the lattice shearing process due to the successive passage of twinning partials characterized by displacement vector b_p (Fig. 2.5). In this process, the first layer fault corresponds to the intrinsic stacking fault (*isf*) similar to that produced by GSF calculations described above. To compute the second layer fault energy, a new shear level (geometrically identical to the first one) should be introduced. Then, only the atoms above this level are rigidly shifted by the same displacement vector b_p without affecting the already existing first layer fault.

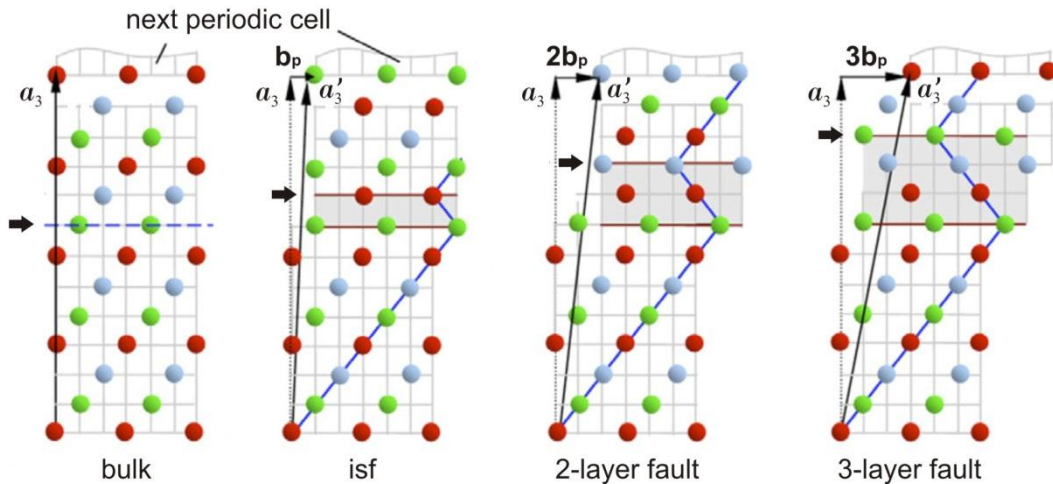


Fig. 2.5. GPFE calculations at atomic scale. Location of a newly introduced shear level is indicated with a black arrow for each simulation cell. The picture is modified from the scheme provided by Kibey *et al.* (2007) for modeling 3-layer twin nucleation in fcc metals.

As such, the upper part of the simulation cell is displaced by $2b_p$ (Fig. 2.5). A similar procedure can be further repeated to create the third, fourth *etc.* layers. Similarly to the GSF calculations (see section 2.2.1), in order to keep periodicity of the atomic array, the supercell vector a_3 is tilted by the total displacement vector (Fig. 2.5). Once the energy calculations for N and $N+1$ layers yield the same GPFE, the twin nucleation event is reached and further increase in the defect thickness represents the twin growth. For instance, in GPFE calculations for *fcc* and *bcc* metals, formation of 3-layer twins is typically observed (Kibey *et al.* 2007; Wang and Sehitoglu 2013; Ojha *et al.* 2014).

Several TEM studies of low pressure CaIrO_3 post-perovskite analogue (Miyajima *et al.* 2010; Niwa *et al.* 2012) indicate presence of $\langle 110 \rangle \{110\}$ twin domains (see Table 1.1 in Chapter 1). Therefore, in this study GPFE landscape is computed for $\langle 110 \rangle \{110\}$ system in MgSiO_3 post-perovskite. In order to avoid ineligible overestimation of the twinning energy landscape (which will lead to overestimation of the critical twinning stress), degrees of freedom along (110) plane are restricted for Si atoms only. In order to allow additional shuffling across the twinning plane optimizing the faulted structure, all the atoms within one Si-octahedra thick layer above and below the newly introduced stacking fault are allowed to relax fully (for more details see Chapter 7). These shuffles do not produce drastic structural changes and do not exceed 25% of interatomic distances. GPFE simulations are performed both from the first principles and with the empirical potential at constant volume conditions at 120 GPa. The designed simulation cells are as thick as 18 Si-octahedra layers (~ 43 Å) along the direction normal to $\{110\}$ twinning plane and contain 180 atoms. The exact computational setup for DFT and semi-empirical calculations is provided in sections 2.1.1 and 2.1.2, respectively.

2.3 Atomistic modeling of linear defects

Dislocations represent linear defects with a translational symmetry characterized by a dislocation line l , and a Burgers vector b (the elementary amount of shear carried by the dislocation). These two vectors are parallel in case of screw dislocations and perpendicular in case of edge dislocations (Fig. 2.6). The long range displacement field produced by dislocations can be described using continuum models, which however fail near the

dislocation core where elastic theory breaks down. Atomic scale modeling is a powerful technique able to provide direct information about the dislocation core structure which is essential, for example, for understanding the anisotropy of plastic shear.

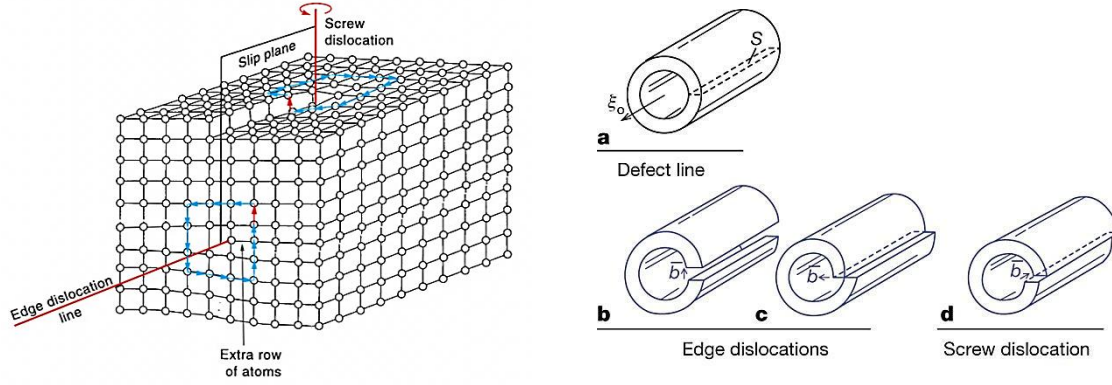


Fig. 2.6. Left panel: screw and edge dislocations in a crystalline material. Burgers circuit is indicated with blue arrows. Right panel: reference cylinder (a) with Volterra edge (b,c) and screw dislocations (d). The picture is modified from Cordier et al. (2014).

2.3.1 Designing and analyzing dislocation cores structures

Designing dislocation cores

Based on the isotropic elastic theory (Hirth and Lothe 1982), displacement field u_x produced by a Volterra screw dislocation (Fig. 2.6d) with Burgers vector b aligned with x axis can be described with the following expression:

$$u_x = \frac{b}{2\pi} \operatorname{atan}\left(\frac{z}{y}\right). \quad (2.11)$$

In this work, initial configurations of screw dislocations are created by imposing in a perfect crystal an isotropic displacement field u_x (2.11) using the command-line program Atomsk (Hirel 2015). Then, structural relaxation (using the computational setup described in sections 2.1.1 and 2.1.2) yields a dislocation core configuration counting anisotropic effects.

For a Volterra edge dislocation (Fig. 2.6b, c) with a dislocation line l lying along the x axis and the Burgers vector b along the y axis, the displacement field can be described as:

$$u_y = \frac{b}{2\pi} \left[\text{atan} \left(\frac{z}{y} \right) + \frac{yz}{2(1-\nu)(y^2 + z^2)} \right], \quad (2.12)$$

where ν is the Poisson ratio. Atomic structure of an edge dislocation is characterized by the presence of an atomic extra half plane (left panel of Fig. 2.6). Thus, an edge dislocation could be constructed through inserting an extra row of atoms into the system followed by introducing the corresponding elastic displacement field described by eq. 2.12. This method seems to be straightforward, however in practice, when such a dislocation is embedded into a simulation cell of finite size, it's not possible to keep the atomic array fully periodic along the Burgers vector direction because atomic planes at the cell boundaries are deformed. Also, in case of complex materials (characterized by the presence of several atomic sublattices), it is very difficult to control the exact location of the glide plane while creating a dislocation this way.

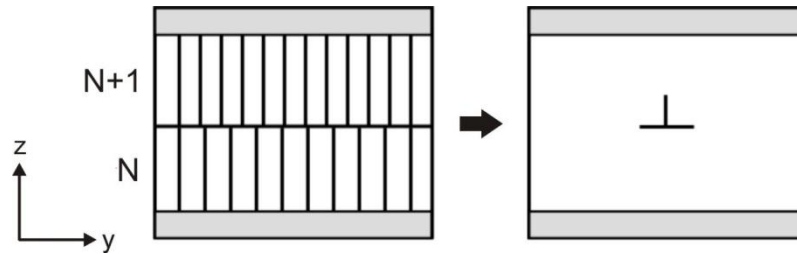


Fig. 2.7. Building an edge dislocation. Grey zone corresponds to the fixed area described in the section 2.3.2.

To avoid these technical difficulties, edge dislocations are constructed in this study by building and joining along the z axis two supercells of size $b \times N$ and $b \times (N+1)$ along the y direction (Fig. 2.7). Structural relaxation of the joint atomic array gives a rise to an edge dislocation (Osetsky and Bacon 2003; Bulatov and Cai 2006) with a Burgers vector aligned with y and a dislocation line along x .

Analyzing structure of relaxed dislocation cores

Geometric characteristics of relaxed dislocation cores can be extracted from their disregistry S , which can be computed from the relative displacements of atoms near the core. Figure 2.8 illustrates a typical structure of an edge dislocation spread along the y

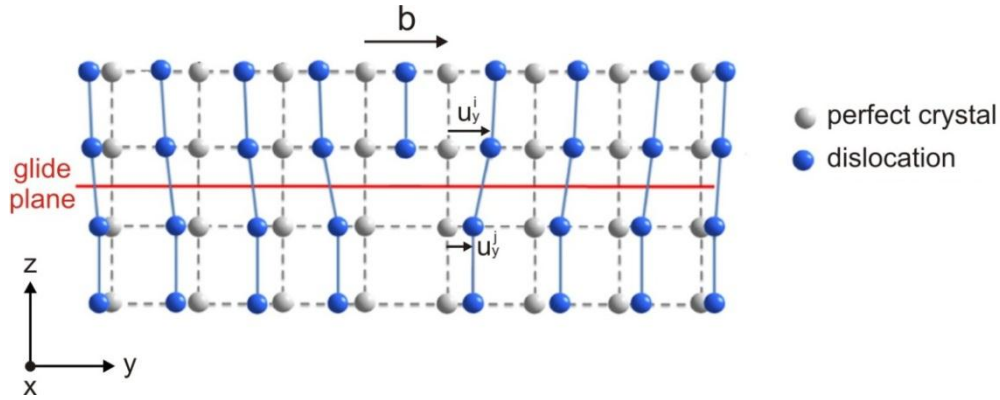


Fig.2.8. Crystal lattice containing an edge dislocation superposed with the original structure of the perfect crystal. The atomic displacements (along y) created by the dislocation above and below the glide plane are indicated as u_y^i and u_y^j , respectively; the Burgers vector direction is indicated with the arrow.

direction aligned with the burgers vector. With respect to the perfect crystal structure, atom i located right above the glide plane is displaced by u_y^i , while the nearest neighboring atom j located right below the glide plane is displaced by u_y^j . Analyzing such atomic displacements for all the i - j pairs along the dislocation core spreading, one can compute the corresponding atomic disregistry as $S_y = u_y^i - u_y^j$. To describe the 3D structure of a dislocation core, similar procedure can be performed along the other directions. For instance, for the edge dislocation presented on Fig. 2.8, disregistry S_x , computed along the dislocation line, will describe the screw component of the core. Presence of both edge and screw components will indicate mixed character of the dislocation. The same technique can be applied to compute disregistry produced by a screw dislocation core.

The discrete atomic disregistry S_r computed from the actual atomic displacements along r can be further characterized with the continuous function $S(r)$. For a dislocation core with a line lying along the x axis and spreading in the plane normal to z (Fig. 2.8), the corresponding $S(y)$ can be described with the following function (e.g. Joós *et al.* 1994):

$$S(y) = \frac{b}{2} + \frac{b}{\pi} \sum_i^N \alpha_i \cdot \arctan\left(\frac{y - y_i}{\zeta_i}\right), \text{ with } \sum_i^N \alpha_i = 1 \quad (2.13)$$

where b is the Burgers vector length; $0 \leq \alpha_i \leq 1$ is a variable constant equal 1 in case of compact dislocation cores; to 0.5 in case of symmetric core dissociation into two partials;

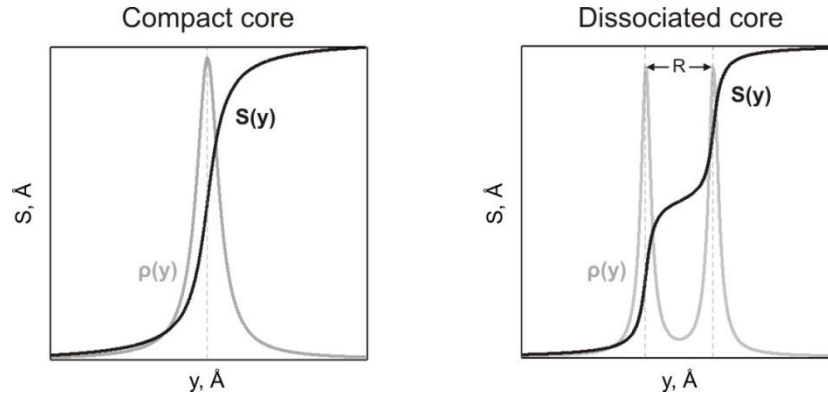


Fig. 2.9. Typical disregistry functions $S(y)$ and dislocation density $\rho(y)$ for compact ($\alpha=1$) and dissociated ($\alpha=0.5$) dislocation cores.

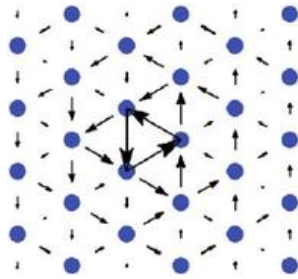


Fig. 2.10. Typical DD-map of $\frac{1}{2}\langle 111 \rangle$ screw dislocation core in bcc metals. Dislocation line and Burgers vector are normal to the plane of representation. The picture is taken from Hayward et al. (2012).

y_i is a location of the dislocation line along the glide direction y ; ζ is a half-width of a dislocation. The derivative $dS(y)/dy$ describes the Burgers vector density $\rho(y)$ in a given plane, and its full width at half maximum defines the width of the dislocation core, *i.e.* 2ζ . Distance between the maximum peaks of the $\rho(y)$ depicts the dissociation distance R between the partial dislocation lines (Fig. 2.9).

In contrast to edge dislocations, where dislocation core spreading can be clearly visualized, in screw dislocation cores, all atomic displacements are parallel to the line and therefore cannot be directly seen in views parallel to this direction. Hence, to get a representative image of a screw dislocation along its line, the differential displacement (DD) maps are commonly used. On this maps, the relative displacements $S_y = u_y^i - u_y^j$ along the dislocation line between all the neighboring atoms i and j are represented by arrows between those two atoms (Fig. 2.10). The lengths of the arrows scale to the amplitude of the displacement. Thus, based on this way of visual representation,

dislocation core spreading can be defined from the location of the biggest arrows between the pairs of atoms.

2.3.2 Geometry of simulation cells

In this work, two types of simulation cell geometries are employed (Fig. 2.11). The first one is fully periodic in all directions and contains a quadrupole of screw dislocations. The second one – of the so-called “slab” type, where the cell borders parallel to the glide plane are fixed. Keeping atomic systems as thin as a single Burgers vector b along x ensures the dislocation lines to be straight and infinite due to the periodic boundary conditions.

Quadrupole

For modeling compact [100] screw dislocation cores, a quadrupole arrangement of dislocations embedded in a fully periodic atomic array is used (Fig. 2.11a). Such a cell contains two dislocations with positive Burgers vector and two dislocations with negative arranged as a rectangular checkerboard pattern. This geometry allows canceling the long range displacement field produced by a single dislocation (Cai 2005) and ensures that interaction of dislocations remains only at a quadrupolar level and that the net force on each core is zero due to the periodic arrangement (Bigger *et al.* 1992). For the simulations performed with the pairwise potential, size of the atomic arrays was gradually increased along y and z in order to track size effect on the dislocation core geometry, Peierls stress σ_p and Peierls potential V_p . Simulation cell with a size of $b \times 100 \text{ \AA} \times 100 \text{ \AA}$ containing 3840 atoms is found to be sufficient to reproduce correctly the properties mentioned above. A quadrupole can be reduced into a twice smaller, but still fully periodic cell (Bigger *et al.* 1992) containing a dislocation dipole (Fig. 2.11a), which is especially useful for computationally expensive *ab initio* calculations. Thus, for DFT simulations, the smallest possible quadrupolar atomic array of $48 \text{ \AA} \times 36 \text{ \AA}$ (720 atoms) along [010] and [001], respectively, is reduced into a dipole (360 atoms).

Slab

Fully periodic atomic arrays containing a dipole or quadrupole arrangement of extended (dissociated) dislocations should be extremely large to minimize the long-range

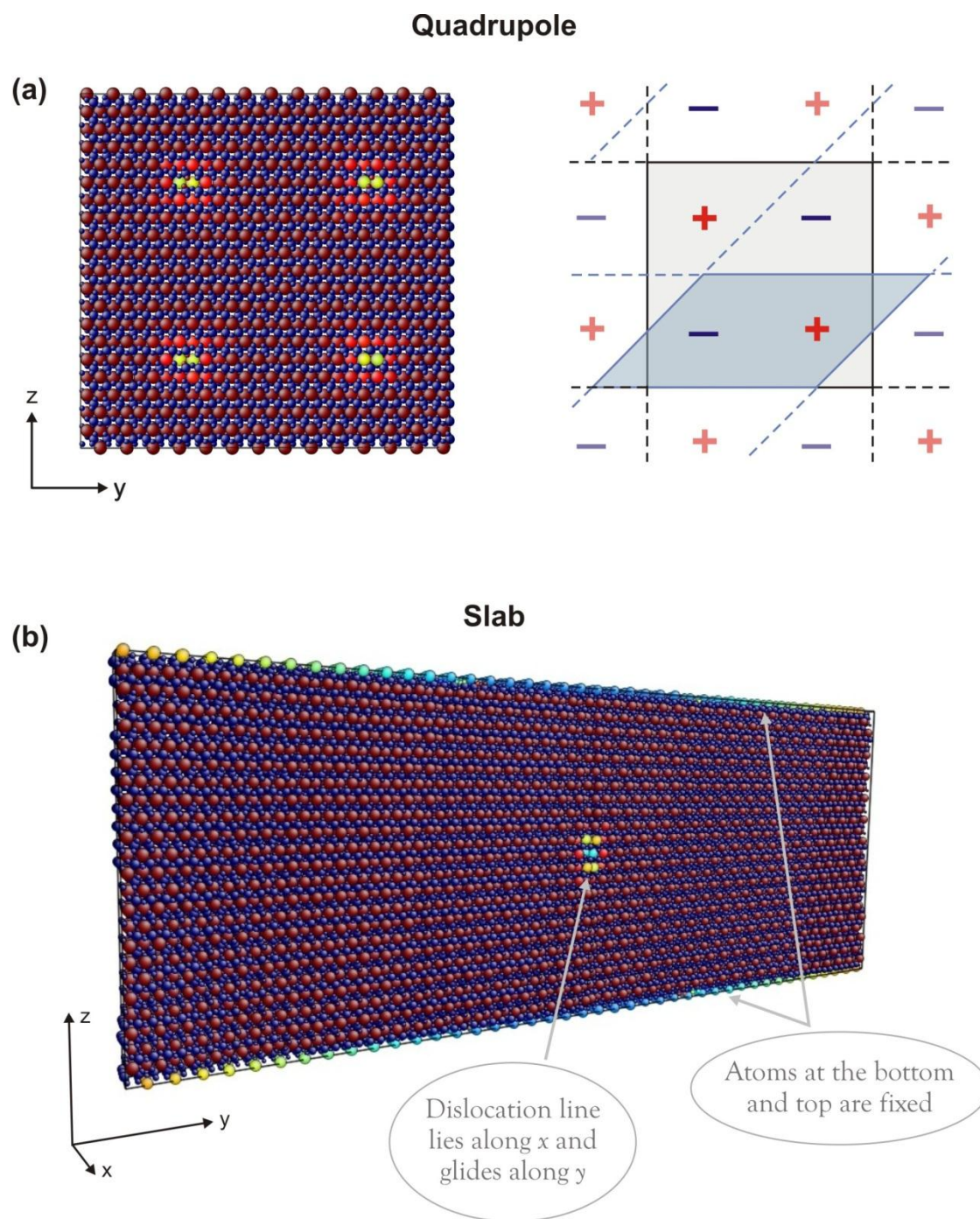


Fig. 2.11. (a) Right panel: post-perovskite atomic array containing a quadrupole of $[100]$ screw dislocations. Left panel: schematic illustration of a quadrupole and reduced dipole of screw dislocations in a fully periodic cell. (b) "Slab" geometry of simulation cells employed for modeling edge and extended screw dislocations in this work.

elastic interactions between the dislocations. In order to overcome this issue, the so-called “slab” geometry (Fig. 2.11b) is employed for modeling $[001]$ and $\frac{1}{2}[110]$ screw dislocations and all the edge dislocations, following the strategy described by (Hirel *et al.* 2014). In this approach, a single dislocation is embedded into a simulation cell which is designed to be fully periodic along the directions of the dislocation line (x) and the dislocation glide direction (y). Along the direction, normal to the glide plane (z), atoms at the bottom and at the top of the supercell are fixed to their regular positions (Fig. 2.11b) and atomic relaxation is only allowed for the rest of the crystal. This enables mimicking an infinite perfect crystal and allows avoiding ineligious interactions between the periodic replicas of the dislocation. The total width (along z) of the layer with fixed atoms is equal to the potential short range cut off distance, *i.e.* to 12 \AA in our case. For screw dislocations, the supercell parameter aligned with y is tilted by $\frac{1}{2}b$ along x in order to keep periodicity along the dislocation glide direction (Fig. 2.12).

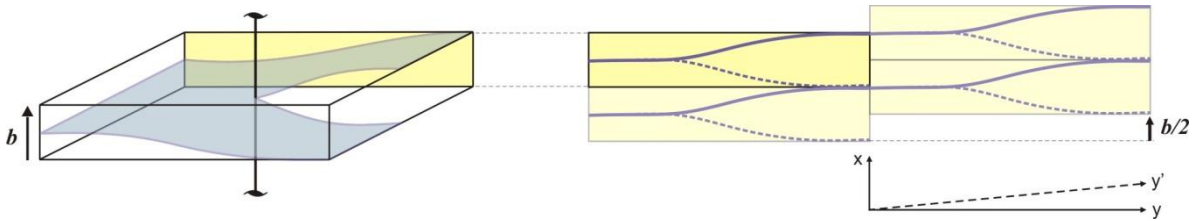


Fig. 2.12. Left panel: displacement field produced by a screw dislocation. Right panel: tilting y axis in order to keep periodicity of the ‘slab’ simulation cell along the glide direction.

If the supercell is not large enough, the dislocation core structure and the Peierls stress can be affected by the interaction of the dislocation with its periodic images. Thus, the size of the supercell is gradually increased until convergence is reached. Typical simulation supercell sizes are $\sim 350 \text{ \AA}$ along y , $\sim 160 \text{ \AA}$ along z , and as a single unit cell parameter along x . Such cells contain of the order of 30,000-60,000 atoms depending on the unit length along x .

2.3.3 Computing lattice friction

In order to move, a dislocation has to overcome the intrinsic resistance of the lattice, which is commonly described through the corresponding energy barrier (Fig. 2.13), called Peierls potential (Peierls 1940, Nabarro 1947), or through the critical stress needed to move a straight infinite dislocation line in absence of thermal activation, called Peierls stress.

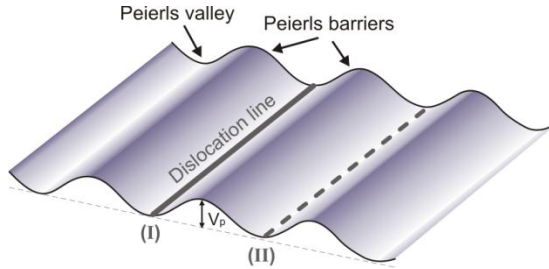


Fig.2.13. Lattice friction: schematic illustration of a straight dislocation line gliding over the Peierls potential from the valley (I) to the valley (II).

The Peierls potential V_p can be directly computed with the NEB method (see section 2.1.3) as the energy barrier that a straight dislocation line has to overcome in order to move from one stable position in the Peierls valley to the next one. The corresponding Peierls stress σ_p can be estimated from the maximum slope of the Peierls potential: $\max \frac{dV_p}{dy} = b\sigma_p$. In this work, this strategy is applied for [100] screw dislocations with compact cores, which allow building fully periodic atomic systems (*e.g.* as illustrated on Fig. 2.11a).

Alternatively, critical stress σ_p , needed to trigger dislocation glide can be found by applying a simple shear strain to the simulation cell in order to increase the shear stress in a glide plane. The force acting on the dislocation is then given by the Peach-Koehler equation (Peach and Koehler, 1950):

$$\vec{F}_l = (\vec{\sigma} \cdot \vec{b}) \times \vec{l}, \quad (2.15)$$

where \vec{F}_l is a force acting on a unit length of a dislocation line \vec{l} ; $\vec{\sigma}$ is the applied stress tensor resulting from straining the cell and \vec{b} is the Burgers vector. In this work, this approach is applied both for fully periodic (Fig. 2.11a) and for the slab-type (Fig. 2.11b) simulation cells. All atomic systems, employed to compute lattice friction, are oriented in such a way that the dislocation line lies along x and glides in the plane normal to z along the y axis. In order to initiate a dislocation glide, ε_{xz} and ε_{xy} components are gradually increased for screw and edge dislocations, respectively, in accord with the eq. (2.15). To

ensure quasi-static loading, after applying a shear strain increment (of the order of 10^{-4} - 10^{-3}), the deformed atomic configuration is optimized accordingly to the procedure described in the computational setup. The Peierls stress σ_p is evaluated as the critical stress needed to initiate the dislocation glide. The values estimated for different glide planes describe anisotropic lattice friction in a material.

2.4 Thermally activated dislocation glide

2.4.1 Kink-pair formation mechanism

At finite temperature, the actual motion of a dislocation from one Peierls valley to the next one is assisted both by stress and thermal activation, which means that actual dislocation motion starts at the stresses lower than the Peierls stress. The corresponding mechanism involves nucleation of kink-pairs on a dislocation line followed by their propagation through the crystal structure, *i.e.* the dislocation does not move as a straight line, but partly bows out over the Peierls potential (Fig. 2.14). For low lattice friction materials, like metals, the limiting process of thermally activated dislocation glide is nucleation of the kink-pairs (Cai *et al.* 2004); while for high-lattice friction materials, it may be rather controlled by the kink-pair migration, *e.g.* in case of dissociated dislocations in silicon (Bulatov *et al.* 2001; Pizzagalli *et al.* 2008b).

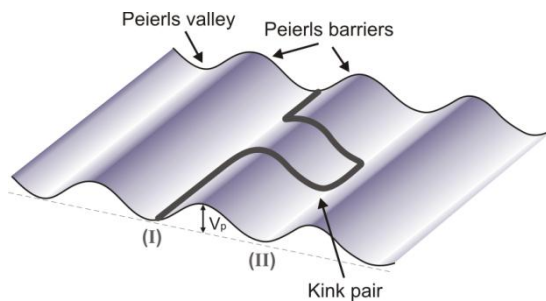


Fig. 2.14. Thermal activation of dislocation glide: schematic illustration of the kink-pair mechanism which allows the dislocation line to pass from one Peierls valley to the next one at finite temperature.

The kink-pair formation process can be described based on different models, such as the kink-kink (KK) interaction model (Seeger and Schiller 1962; Seeger 1981), the elastic interaction model (Koizumi *et al.* 1993, 1994) and the line tension (LT) model (Guyot and Dorn 1967). The first two models are only suitable at the low stress regime, where the

kink-pair shape is not much affected by the external stress. When the kinks are distant enough ($w \gg h$), their elastic interaction does not depend on the exact shape of the slope and, therefore, can be assumed to a simple rectangular kink shape model, where dislocation line segments represent pure screw and pure edge components. This approximation was first used for the KK interaction model, where the elastic interaction potential between such a kinks is simply $-\frac{\mu h^2 b^2}{8\pi w}$ (Hirth and Lothe 1982; Seeger 1981). Further, this model was developed into the elastic interaction model (Koizumi *et al.* 1993, 1994), which allows distinguishing the rectangular and trapezoidal kink shapes, but still applicable only at the low stress regime. In contrast to these two models, the LT model is also valid for the high stress regime and allows describing evolution of the kink-pair formation enthalpy with applied stress. This model is shown to be very effective for the low lattice friction materials (like metals) where self energy of a dislocation line is much higher than the Peierls barrier (Caillard and Martin 2003; Proville *et al.* 2013; Dezerald *et al.* 2015).

For all the models described above, the enthalpy ΔH of a kink pair can be generally defined as follows:

$$\Delta H = \Delta E_{el} + \Delta P - W_{\sigma}, \quad (2.16)$$

where ΔE_{el} is the increase in elastic energy of the dislocation line; ΔP is the change in Peierls energy of the line portion which leaves the Peierls valley; W_{σ} is the negative contribution due to the work of the applied stress. The ΔH value decreases from $\Delta H(\sigma_a=0)=H_{2k}$, the kink-pair formation enthalpy at zero applied stress, down to $\Delta H(\sigma_p)=0$ at the Peierls stress. This expression is uniform for all the kink models described above, which only differ by the way the ΔE_{el} term, resulted from the increase of the dislocation line, is defined. In contrast to the KK and the elastic interaction model, which provide the exact analytic expression for ΔE_{el} as a function of a kink-pair geometry (characterized by a given width w and height h), the LT model defines this term through the dislocation line stiffness corresponding to the line tension.

In dissociated dislocation cores, kink pairs nucleate on the partial dislocation lines. This process can occur in several different ways. Thus, the two kinks may nucleate simultaneously on the both partials; or one kink-pair can nucleate independently on one of the partials. Figure 2.15 illustrates the two extreme cases of the kink-pair nucleation on the dislocation partials, corresponding to the so-called "correlated" nucleation (Fig. 2.15a),

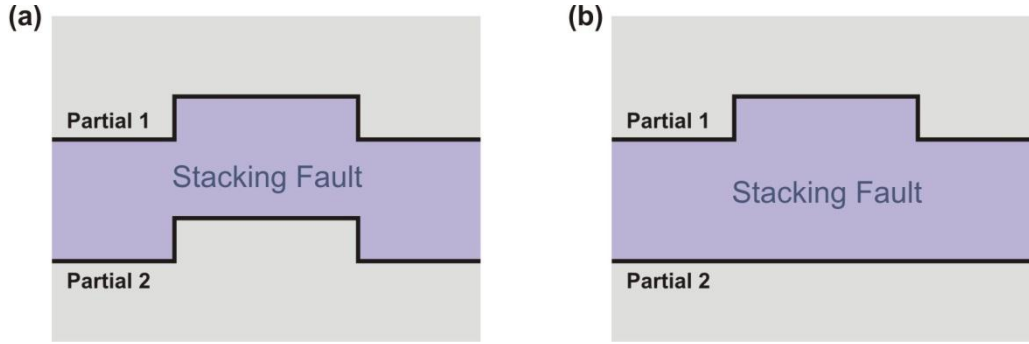


Fig.2.15. Schematic illustration of (a) correlated and (b) uncorrelated rectangular kink-pair nucleation on collinear partials of a dissociated dislocation.

where the stacking fault width remains invariant; and to the so-called "uncorrelated" nucleation (Fig. 2.15b), where one dislocation partial remains straight and the width of the stacking fault between the partials locally changes. Change in the stacking fault width results in additional ΔW_{sf} energy increase contributing into the kink-pair enthalpy ΔH . Different configurations of the kink-pair nucleation on dissociated dislocations were described within the elastic interaction model for MoS_2 and MgAlO_4 spinel by Mitchell *et al.* (2003) and for MgSiO_4 wadsleyite and ringwoodite by Ritterbex *et al.* (2015; 2016).

In this work, the full curve describing evolution of ΔH with applied stress σ_a is investigated based on the LT model in conjunction with atomic scale simulations for [100] screw dislocations. The detailed procedure is provided in the next section. For dissociated [001] dislocations, the kink-pair formation enthalpy $\Delta H(\sigma_a=0)$ is estimated using the elastic interaction model (Koizumi *et al.* 1993) for the rectangular kink-pair with large width w ($w \gg h$), relying on the exact characteristics of straight [001] dislocations (core geometry, γ -energy and Peierls barrier) inferred from the atomic-scale modeling.

2.4.2 LT model in conjunction with atomistic simulations

Within the line tension (LT) model, a dislocation is considered as an elastic string on a periodic substrate. Change in elastic energy ΔE_{el} during the kink-pair formation is calculated through the stiffness of the dislocation line, *i.e.* the line tension Γ . A dislocation can be represented as a 1D function $y(x)$ which describes its position y in the glide plane at

each x coordinate along the dislocation line. Assuming the line tension Γ to be stress independent and derivative of the $y(x)$ function to be small ($dy/dx \ll 1$), a linearized version of the LT model can be applied to compute the dislocation enthalpy H_{LT} :

$$H_{LT}(y(x), \sigma_a) = \int dx \left[V_P(y(x)) - \sigma_a b y(x) + \frac{\Gamma}{2} \left(\frac{dy}{dx} \right)^2 \right], \quad (2.17)$$

where Γ is the line tension (representing the stiffness of the dislocation line), and the term $V_P(y(x)) - \sigma_a b y(x)$ corresponds to the so-called “substrate enthalpy” in 1D-Frenkel-Kontorova model (Frenkel and Kontorova 1938; Joos and Duesbery 1997). To use this equation, the V_P term can be computed at atomic scale with the NEB method (as described in the section 2.1.3). The line tension Γ can be also estimated at atomic scale based on the procedure described below in detail. Once V_P and Γ are known, the critical kink-pair enthalpy H_{LT} and the corresponding equilibrium kink-pair shape at a given stress can be found from the eq. (2.17) as the saddle point on the H_{LT} energy landscape.

Computing line tension of a dislocation at atomic scale

The line tension Γ can be calculated at atomic scale as the energy cost associated with a dislocation bow-out consistent with the first stage of kink-pair formation. Bending a dislocation line requires breaking up $1b$ translational symmetry of the simulation cell. Thus, following the strategy proposed by Rodney and Proville (2009), the length of the supercell along the dislocation line is increased up to $2b$ (Fig. 2.16) and the dislocation line is considered as the two segments of length b : segment S_1 remains in the Peierls valley (I) while another segment S_2 starts bowing out towards to the next valley (II).

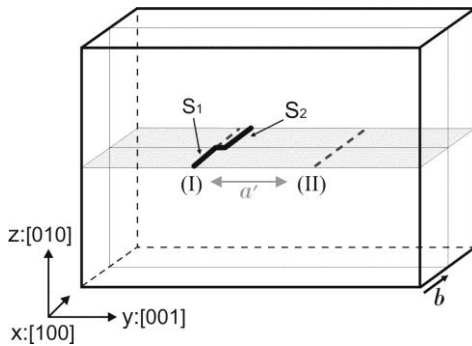


Fig. 2.16. Schematic illustration of a dislocation line bending, mimicking the very beginning a kink-pair formation, in $2b$ simulation cell. Glide plane is highlighted with gray.

In order to accurately compute this process at atomic scale, atoms around the dislocation segment S_2 are forced to follow the exact displacements Δx along the MEP derived from NEB simulations (see the section 2.1.3); while the corresponding atoms belonging to the segment S_1 are fixed to their regular positions in the valley (I). Practically, it means that for the selected atoms around the dislocation core, degrees of freedom along the dislocation line are constrained. The energy increase associated with the small gradual disposition (up to 3-5%) of the dislocation line segment S_2 (accounting for the periodic boundary conditions along the dislocation line): $\Delta E_{LT} = \Delta E - bV_P(Y_1) - bV_P(Y_2) = \frac{\Gamma}{b}(Y_2 - Y_1)^2$, can be used to extract the corresponding value of the line tension Γ .

CHAPTER 3

Generalized Stacking Faults

Atomistic simulations based on empirical potentials represent a very attractive technique for modeling defects as it allows employing large atomic arrays, beyond computational capabilities of *ab initio* calculations. However, the use of these potentials fitted to reproduce ground state properties of a material must be additionally validated for modeling defects which involve atomic configurations far from equilibrium. In this chapter transferability of the pairwise potential parameterization by Oganov *et al.* (2000) is examined for modeling defects in MgSiO₃ post-perovskite. For that purpose, the ability of this parameterization to accurately compute the excess energies of generalized stacking faults (GSF), also called γ -surfaces, is verified by comparing them with previous calculations from the first principles. The performed simulations of γ -surfaces are followed by a detailed analysis of the influence of crystal chemistry in the post-perovskite structure on its ability to be sheared. This chapter is intended to serve as a basis for the full atomistic modeling of dislocations in MgSiO₃ post-perovskite provided in the next three chapters.

3.1 Location of the shear planes

The base-centered orthorhombic C -lattice of the post-perovskite results in four potential shear vectors: $[100]$, $[010]$, $[001]$ and $\frac{1}{2}[110]$ which correspond to the shortest lattice repeats. For a given shear direction, potential glide planes are expected to be among those with the largest d_{hkl} distance, *i.e.* with the lowest Miller index of the (hkl) plane. Thus, there are five potential glide planes and ten slip systems to test: $[100](010)$, $[100](001)$, $[100](011)$, $[010](100)$, $[010](001)$, $[001](100)$, $[001](010)$, $[001](110)$, $\frac{1}{2}[110](001)$ and $\frac{1}{2}[110](1\bar{1}0)$.

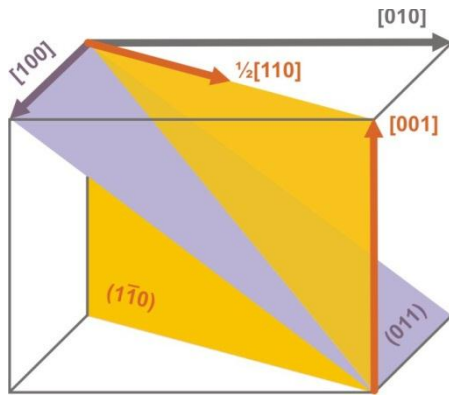


Fig. 3.1. Shear vectors $[100]$, $[010]$, $[001]$ and $\frac{1}{2}[110]$, and diagonal planes (011) and $(1\bar{1}0)$ in a base-centered orthorhombic C -lattice.

In contrast to metals, most minerals have complex crystal structures with interatomic bonds of significantly different nature. This fact requires a detailed consideration of bonding and makes the crystal chemistry dominant over the simple concept of close-packed atomic planes for predicting the most probable slip planes. Thus, for each (hkl) plane, we consider different possibilities of its location along z_{hkl} ² in order to analyze the effect of different types and number of bonds involved.

Atomic planes parallel to (100) are the most densely packed planes in the post-perovskite structure (see Chapter 1, section 1.1). All atoms in the structure are located at two levels along the shortest $[100]$ direction: $z_{100}=0$ and $z_{100}=0.5$ (Fig. 3.2a). Consequently, for the (100) , there is only one cutting level located at $z_{100}=0.25$ (equivalent to $z_{100}=0.75$ according to the symmetry of the structure).

² Here and hereafter, z_{hkl} corresponds to the Cartesian z normal to the (hkl) plane.

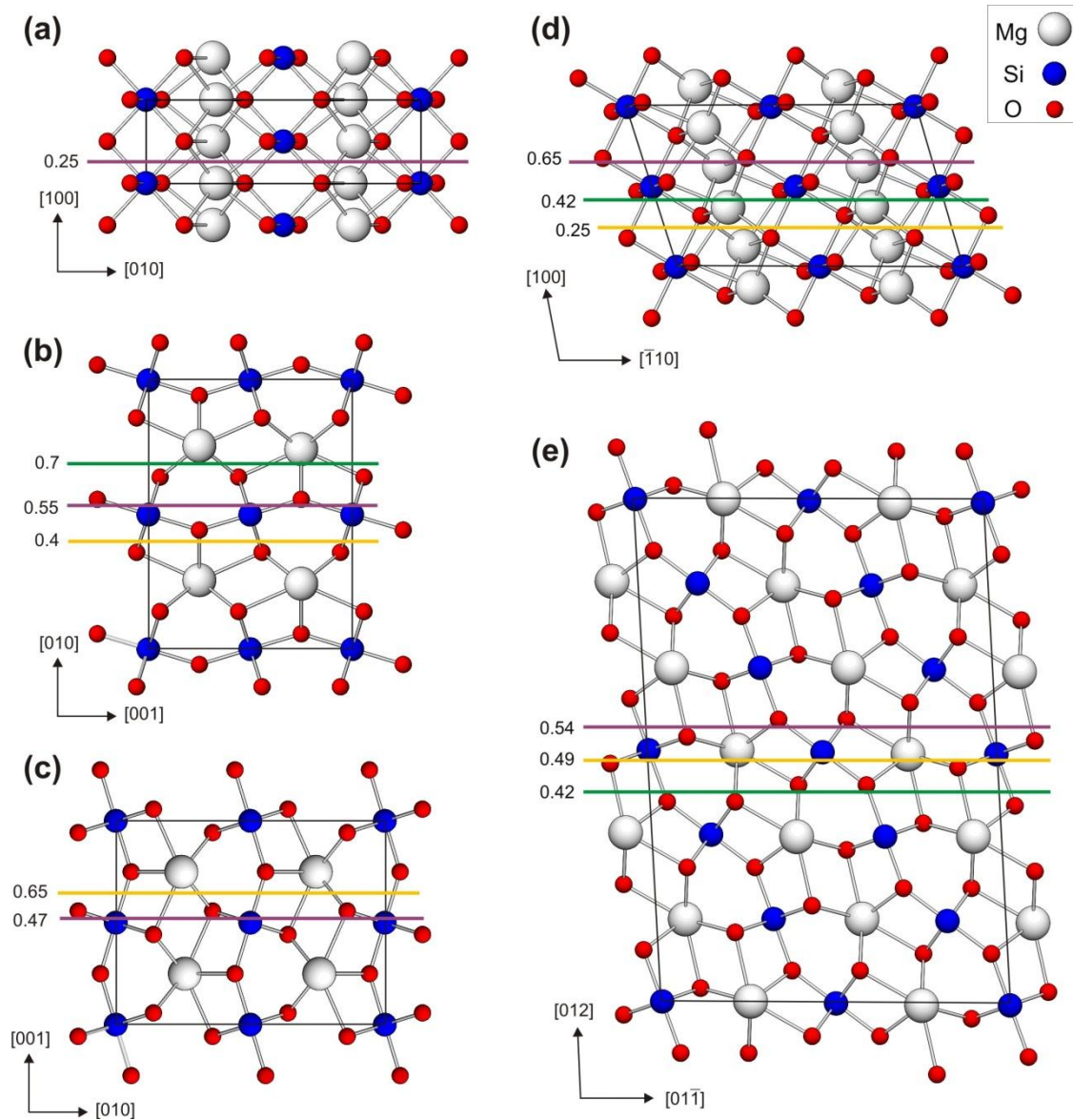


Fig. 3.2. Various non equivalent geometric locations of slip planes (100) (a), (010) (b), (001) (c), (110) (d) and (011) (e) in the post-perovskite structure.

The slip planes (010), (110) and (011) have three nonequivalent potential geometric locations for shear. In the (010) plane (Fig. 3.2b), shear can be imposed at the levels $z_{010}=0.7$ (equivalent to 0.2, 0.3 and 0.8), $z_{010}=0.4$ (equivalent to 0.1, 0.6 and 0.9) and $z_{010}=0.55$ (equivalent to 0.05, 0.45 and 0.95). For the (110) plane (Fig. 2d), shear can be applied at $z_{110}=0.25$ (equivalent to 0.75), 0.42 (equivalent to 0.08, 0.58 and 0.92) and 0.65 (equivalent to 0.15, 0.35 and 0.85). The (011) plane (Fig. 2e) can be sheared at $z_{011}=0.42$, 0.49 and 0.54 (equivalent to ± 0.08 , ± 0.01 and ± 0.04 , respectively, with

periodicity $1/6$ (3.64 \AA) along z_{011} since in the designed monoclinic cell there are twelve symmetrical replicas for each cutting level). For the (001) glide plane (Fig. 2c) there are two possibilities: $z_{001} = 0.65$ (equivalent to 0.15, 0.35 and 0.85) and 0.47 (equivalent to 0.03, 0.53 and 0.97). The number of the affected bonds per unit cell for each of the listed cutting levels is given in Table 3.1.

3.2 GSF excess energies

Previous *ab initio* studies of GSF in MgSiO_3 post-perovskite provided only γ -lines (Carrez *et al.* 2007a; Metsue and Tsuchiya 2013). In this work, full γ -surfaces are calculated for all possible slip planes and cutting levels. The shape of the obtained γ -surfaces clearly reflects the symmetry of the structure in a given glide plane for all configurations considered in this work (Figs. 3.3a-k). In agreement with the *Cmcm* space group, each γ -surface exhibits a mirror plane m perpendicular to the [100] and [001] directions. Due to the *C*-lattice, $\frac{1}{2}[110]$ translation vector is clearly seen in (001) and (110) γ -surfaces (Figs. 3.3a, b, h-j) such as all energy minimum valleys and maximum peaks are translated by $\frac{1}{2}\langle 110 \rangle$. For (010) with $z_{010} = 0.7$ and (110) with $z_{110} = 0.65$ γ -surfaces, there are metastable stacking faults (Figs. 3.3c,h) which presence is not caused by additional translation vectors of the lattice but by the favorable atomic arrangement in these configurations of faulted crystals. In case of (010), the stacking fault is located exactly in the middle of the γ -surface (Fig. 3.3c), while stacking faults on (110) are centered with respect to [001] and disposed at $\frac{1}{3}[110]$ with $\frac{1}{2}\langle 110 \rangle$ periodicity (Fig. 3.3h). Presence of such stacking faults may indicate simultaneous presence of $\frac{1}{2}[100]$ and $\frac{1}{2}[001]$ Burgers vector components for dislocations lying on (010) as well as $\frac{1}{3}[110]$ and $\frac{1}{2}[001]$ components for dislocations related to (110) as it is shown with arrows on (Figs. 3.3c,h). Among all examined γ -surfaces, the (010) plane with $z_{010} = 0.7$ (Fig. 3.3c) is characterized by the lowest excess energies, while the highest energy barriers are observed for (100) and (001) at $z_{001} = 0.47$ along the longest [010] direction (Table 3.1; Figs. 3.3a,k).

Glide along the [100] and $\frac{1}{2}\langle 110 \rangle$ directions are characterized by a single maximum peak while glide for all the other systems exhibit a camel hump shape with a local minimum at 50% along the shear vector (Figs. 3.4a-j). This indicates the presence of a

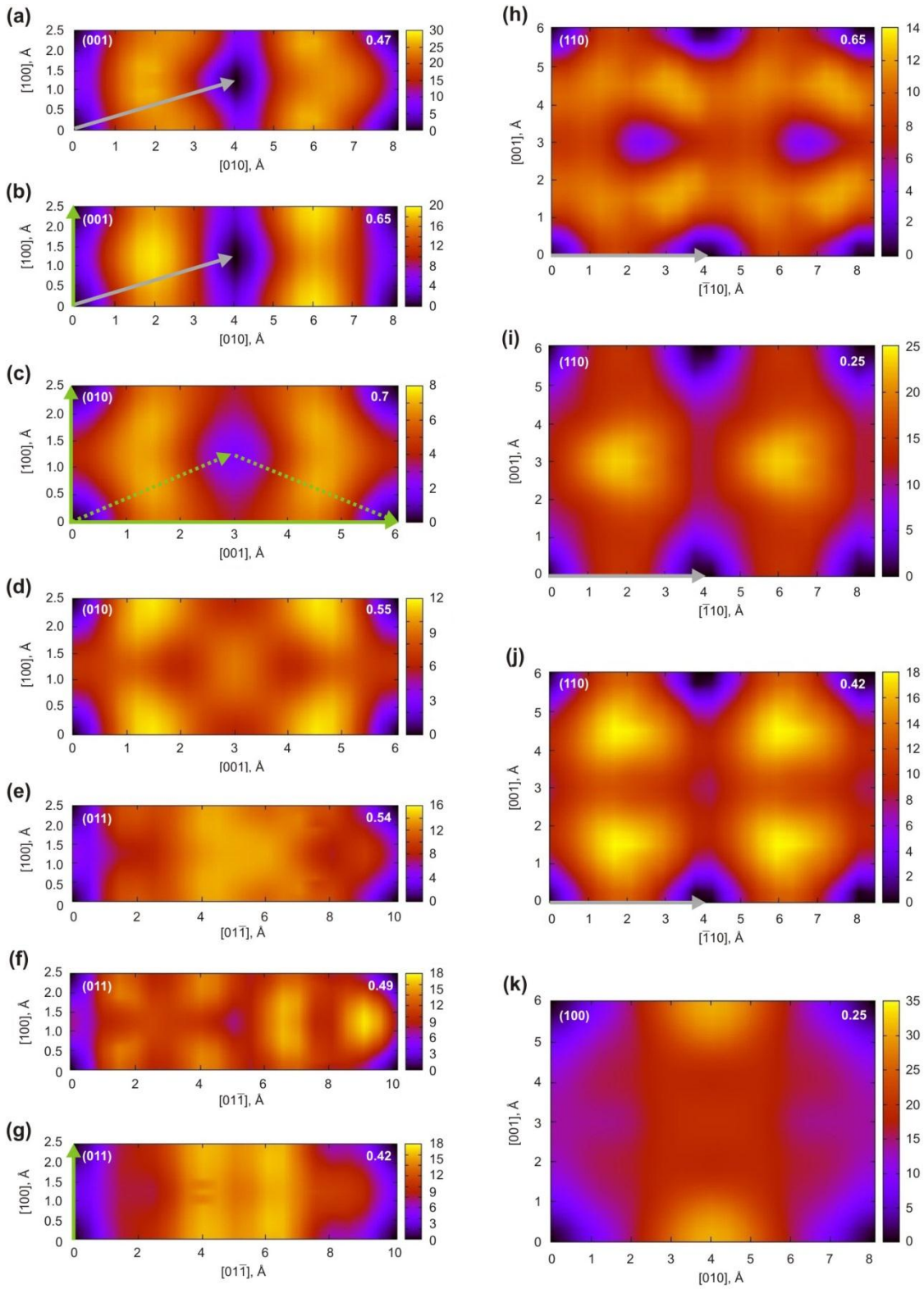
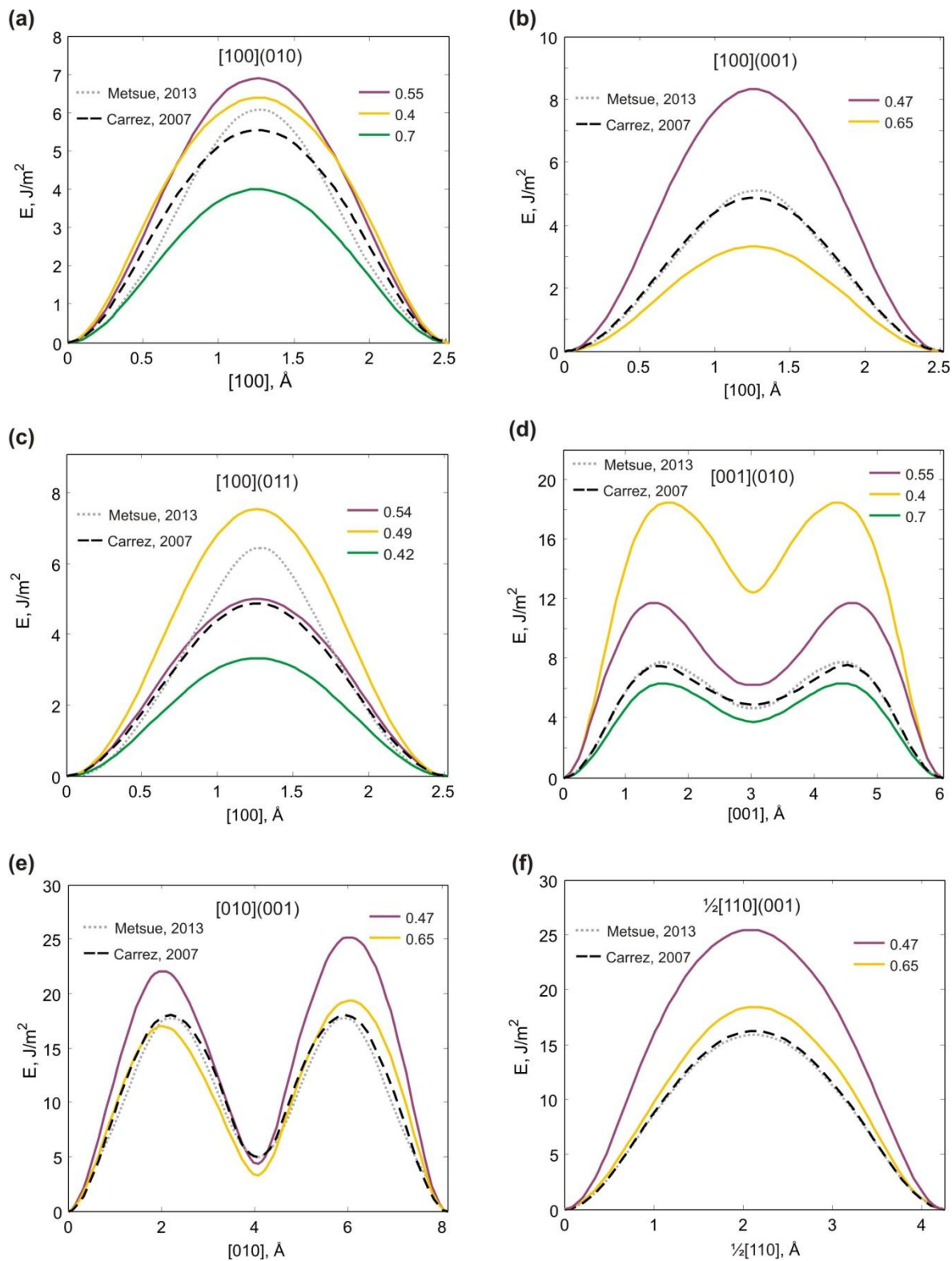


Fig. 3.3. 2D projections of γ -surfaces (in J/m^2). The corresponding shear levels z_{hkl} are given on each plot. Easy slip directions are indicated with green arrows; $\frac{1}{2}\langle 110 \rangle$ translation vectors are shown with grey arrows.



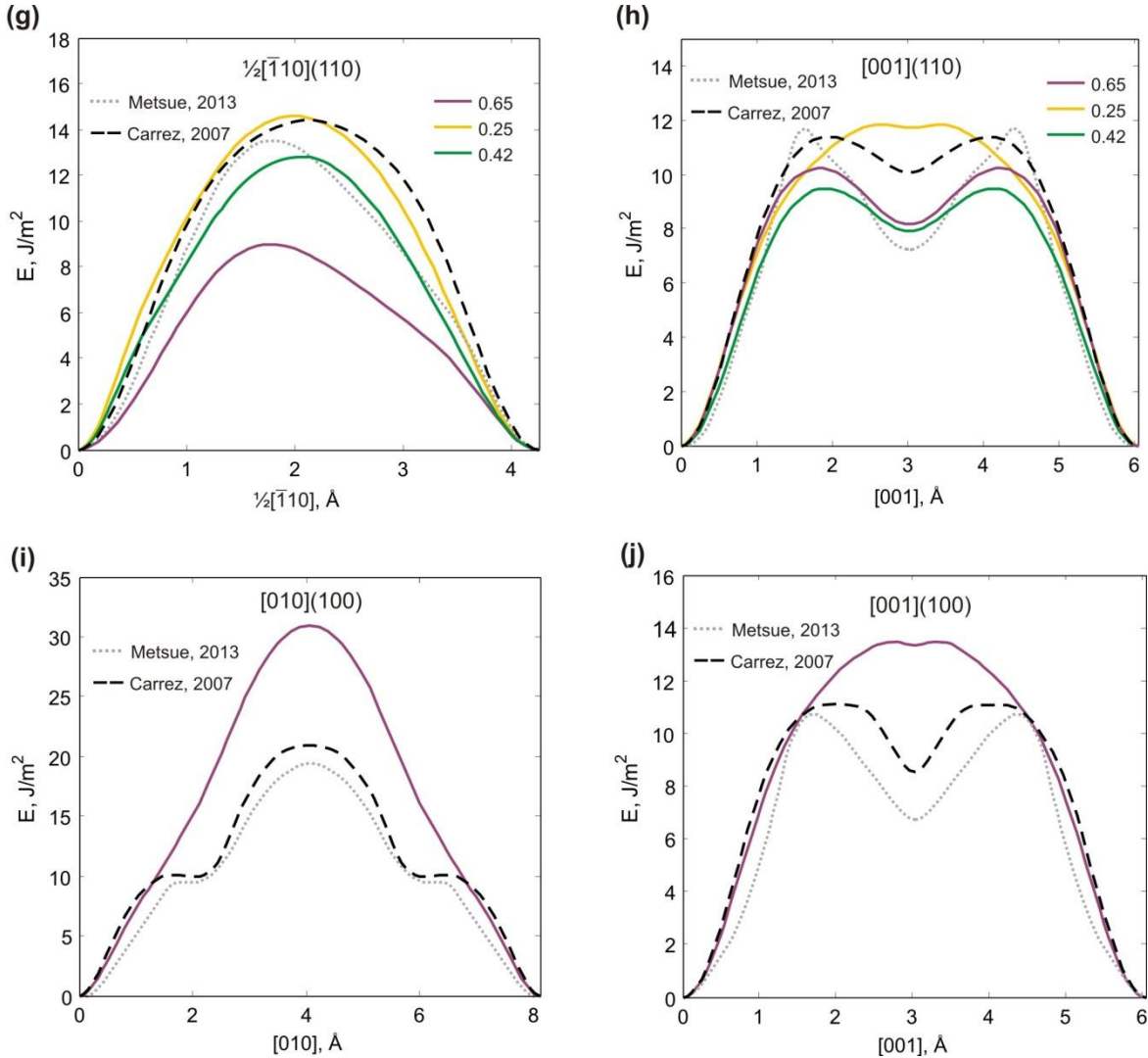


Fig. 3.4. γ -lines computed in this work with pairwise potential (Oganov et al. 2000) compared with previous DFT studies (Carrez et al. 2007a; Metsue and Tsuchiya 2013).

stable stacking fault suggesting the possibility of dissociation of $[001]$ and $[010]$ Burgers vectors into two partial dislocations with $\frac{1}{2}[001]$ and $\frac{1}{2}[010]$ Burgers vectors. The base-centered C -lattice affects the shape of the $[010](001)$ γ -line (Fig. 3.4e). In the (001) plane, translation of atoms and, consequently, of GSF excess energy maximum peaks and/or minimum valleys occur by vector $\frac{1}{2}[110]$ (Fig. 3.3a, b) which results in asymmetric shape of $[010](001)$ γ -lines. Both for $z_{001} = 0.65$ and $z_{001} = 0.47$, the maximum peaks located at $\frac{3}{4}[010]$ are about 2.5 J/m^2 (10-12%) higher than peaks at $\frac{1}{4}[010]$ which can be explained by differences in geometry of faulted crystals with $\frac{1}{4}[010]$ and $\frac{3}{4}[010]$ rigid shear. Thus, close to the slip plane, configuration with $\frac{3}{4}[010]$ shear is characterized by shorter Mg-Si

distances (by ~ 0.5 Å) and longer Si-O bonds with apical oxygens (by ~ 0.4 Å) than those with $\frac{1}{4}[010]$ shear. However, it should be noted that the observed asymmetric shapes are not so distinct for the DFT curves (Carrez *et al.* 2007a; Metsue and Tsuchiya 2013). The lowest energy barriers are related to the three slip systems which involve the smallest shear vector $[100]$ ($b = 2.521$ Å) and to the $[001](010)$ slip system with $z_{010} = 0.7$ (only Mg-O bonds are affected). The highest energy barrier corresponds to the $[010](100)$ system (Table 3.1).

3.3 Validity of the pairwise potential

The γ -surface energies computed in this work for the (010), (001), (011) and (110) glide planes are in good agreement with previous *ab initio* simulations by Carrez *et al.* (2007a) and Metsue and Tsuchiya (2013). For these shear planes, pairwise potential accurately reproduces the shape of DFT γ -lines and qualitatively provides 20-30% lower energy barriers with respect to those computed with DFT (see Table 3.1; Figs. 3.4a-h). Discrepancies of $\sim 30\%$ observed for $[100](010)$ and $[100](001)$ slip systems may be partly attributed to an overestimation of excess energies in DFT calculations resulting from a small size effect in DFT approach. Although the exact cutting levels are not explicitly specified in the works by Carrez *et al.* (2007a) and Metsue and Tsuchiya (2013), the shape of DFT γ -lines for (011) and (110) clearly indicates that, DFT simulations were performed for different cutting levels. Thus, the $[100](011)$ γ -line by Carrez *et al.* (2007) is related to $z_{011} = 0.42$, while the γ -line by Metsue and Tsuchiya (2013) reproduces the shape of the high-energy barrier obtained with $z_{011} = 0.49$ (Fig. 3.4c). Considering γ -lines for (110), the $\frac{1}{2}[\bar{1}10](110)$ asymmetric curve by Metsue and Tsuchiya (2013) is consistent with our lowest energy barrier obtained with $z_{110} = 0.65$, while results by Carrez *et al.* (2007a) agree with the high-energy symmetric curve obtained at $z_{110} = 0.42$ (Fig. 3.4g). However, the easiest cutting level is not the same for $\frac{1}{2}[\bar{1}10]$ and $[001]$ directions: along $[001]$, the lowest energy barrier in (110) corresponds to $z_{110} = 0.42$ (Fig. 3.4h). This phenomenon is considered below in detail.

For (100), the potential model leads to γ -lines with systematically higher energies and comparatively dissimilar shape (Table 3.1; Figs. 3.4i, j). The stacking fault along

[001](100) which appears in DFT curves is barely visible with the potential (Fig. 3.4j). Similarly, along 010, the shoulders at 25% of shear found with the DFT are not reproduced by the potential (Fig. 3.4i). However both DFT and potential model clearly show that (100) is one the most unfavorable planes for shear which involves very high-energy configurations.

Apart from the discrepancy observed for very unfavorable shear planes like (100); results on the γ -surfaces obtained from the potential model compare well with *ab initio* calculations. The empirical parameterization of pairwise potentials proposed by Oganov *et al.* (2000) can be thus considered as valid for modeling shear properties of MgSiO_3 post-perovskite and in particular crystal defects modeling involving atomic arrangements far from equilibrium.

3.4 Influence of crystal chemistry

Analyzing the computed γ -lines from different cutting levels for each (*hkl*) plane, it appears that the lowest and the highest energy barriers do not necessarily correspond to the same cutting levels for shear along different directions within the same plane. For instance, in the (010) plane, shear at $z_{010}=0.7$ cuts only Mg-O bonds (8 bonds per unit cell), whereas only Si-O bonds (6 per unit cell) are cut at $z_{010}=0.55$ and both Mg-O and Si-O bonds (2 Mg-O and 4 Si-O per unit cell) are cut at $z_{010}=0.4$ (Fig. 3.2b). While the lowest excess energy corresponds to $z_{010}=0.7$ for shear along [100] and [001] in (010), the highest energy barriers correspond to different cutting levels (Figs. 3.4 a, d). In (010), shear is easier at $z_{010}=0.55$ compared to $z_{010}=0.4$ along [001], whereas along [100], the energy barrier is higher at $z_{010}=0.55$, although the difference with $z_{010}=0.4$ is very small (Figs. 3.4 a, d; Table 3.1). A similar effect is observed for shear along $\frac{1}{2}[\bar{1}10]$ and [001] in (110) with cutting levels 0.42 (6 Mg-O and 4 Si-O) and 0.65 (8 Mg-O and 4 Si-O). But in this case, the easiest cutting level is not the same for both directions (Figs. 3.4 g, h; Table 3.1). This behavior illustrates that the number and nature of bonds is not enough to describe the ease of shear. The ability for building up new bonds after shear is likely to play an important role.

Table 3.1

Characteristic parameters of the investigated slip systems in MgSiO₃ post-perovskite from γ -surface calculations in comparison with previous theoretical studies

Slip system	Impacted bonds (per unit cell)	γ_{\max} (J/m ²)	γ_{sf} (J/m ²)	ISS (GPa)	
[100](010)	$z_{010} = 0.55$	6 Si-O	6.90	82.5	
	$z_{010} = 0.4$	2 Mg-O, 4 Si-O	6.37	78.3	
	$z_{010} = 0.7$	8 Mg-O	4.00	47.9	
	GGA ¹		5.55	71.7	
	LDA ²		6.01	78.1	
[100](001)	$z_{001} = 0.47$	4 Mg-O, 6 Si-O	8.32	102.2	
	$z_{001} = 0.65$	6 Mg-O, 2 Si-O	3.32	41.0	
	GGA ¹		4.86	61.8	
	LDA ²		5.04	63.4	
[100](011)	$z_{010} = 0.49$	8 Mg-O, 6 Si-O	7.53	93.9	
	$z_{010} = 0.54$	7 Mg-O, 4 Si-O	4.99	60.5	
	$z_{010} = 0.42$	6 Mg-O, 2 Si-O	3.33	40.6	
	GGA ¹		4.91	61.7	
	LDA ²		6.31	80.1	
[010](100)	$z_{100} = 0.25$	12 Mg-O, 8 Si-O	30.14	113.3	
	GGA ¹		21.02	115.8	
	LDA ²		19.25	82.4	
[010](001)	$z_{001} = 0.47$	4 Mg-O, 6 Si-O	25.14	4.31	178.1
	$z_{001} = 0.65$	6 Mg-O, 2 Si-O	19.33	3.32	137.0
	GGA ¹		18.11	4.89	131.2
	LDA ²		17.79	5.04	117.3

Table 3.1 continued

[001](100)	$z_{100} = 0.25$	12 Mg-O, 8 Si-O	13.56	13.23	95.2
	GGA ¹		11.66	9.01	107.1
	LDA ²		11.35	7.35	119.0
[001](010)	$z_{010} = 0.55$	6 Si-O	11.69	6.18	113.0
	$z_{010} = 0.4$	2 Mg-O, 4 Si-O	18.32	12.42	173.8
	$z_{010} = 0.7$	8 Mg-O	6.29	3.72	68.2
	GGA ¹		7.50	4.95	78.0
	LDA ²		7.49	4.56	71.4
[001](110)	$z_{110} = 0.65$	8 Mg-O, 4 Si-O	10.22	8.15	95.7
	$z_{110} = 0.25$	6 Mg-O, 4 Si-O	11.82	11.80	85.7
	$z_{110} = 0.42$	6 Mg-O, 4 Si-O	9.44	7.90	83.7
	GGA ¹		11.42	10.14	101.6
	LDA ²		11.54	7.42	120.6
$\frac{1}{2}$ [110](001)	$z_{001} = 0.47$	4 Mg-O, 6 Si-O	25.43		171.9
	$z_{001} = 0.65$	6 Mg-O, 2 Si-O	18.33		126.9
	GGA ¹		16.23		120.0
	LDA ²		15.81		120.1
$\frac{1}{2}$ $\bar{1}$ 10](110)	$z_{110} = 0.65$	8 Mg-O, 4 Si-O	8.95		82.9
	$z_{110} = 0.25$	6 Mg-O, 4 Si-O	14.39		111.9
	$z_{110} = 0.42$	6 Mg-O, 4 Si-O	12.54		92.2
	GGA ¹		14.44		133.4
	LDA ²		13.65		100.04

¹Carrez et al. 2007a; ²Metsue and Tsuchiya 2013

3.5 Searching for the easiest slip systems

In order to further describe the relative resistance to shear of the potential slip systems, the ideal shear stresses (ISS) are calculated (Table 3.1). ISS represents the upper limit of stress that a perfect crystal can sustain before yielding (Paxton *et al.* 1991). The lowest ISS values together with the lowest γ -surface excess energies can point to the easiest slip systems. The smallest ISS values, as well as the lowest γ -energies, correspond to the slip systems with the shortest [100] shear vector and to the [001](010) slip system with the glide plane located at the level 0.7 along the [010] direction (Table 3.1). In order to analyze an effect of the reduced C_{55} and C_{66} values predicted by the potential model (Table 2.2) on the calculated ISS for these slip systems, the ISS values can be normalized by the corresponding C_{ij} components and compared with those from DFT. Both DFT and semi-empirical values provide the same ISS/ C_{ij} ratios (0.25, 0.3 and 0.19 for [001](010), [100](001) and [100](010), respectively). This correlation between computed elastic constants and ISS indicates that underestimated C_{55} and C_{66} values inevitably result in smaller ISS values (~35%) for [100] slip systems predicted by the potential model (Table 3.1). However, even keeping in mind such an effect of reduced ISS for [100] systems, they clearly remain among the most probable slip systems together with [001](010) which is consistent with the *ab initio* studies by Carrez *et al.* (2007a) and Metsue and Tsuchiya (2013). The empirical potential model also shows that $\frac{1}{2}[\bar{1}10](110)$ (at $z_{110}=0.65$) and [001](110) (at $z_{110}=0.42$) are further possible slip systems. While considering all possible cutting levels in the post-perovskite structure, we show that the lowest and the highest energy barrier can correspond to different shear levels for different directions within the same glide plane. This effect was not taken into account in previous *ab initio* studies and therefore has affected the (011) and (110) γ -surface calculations. Possible relevance of the $\frac{1}{2}[\bar{1}10](110)$ system is in agreement with the slip predicted by Oganov *et al.* (2005) based on the first-principles metadynamics.

3.6 Summary

In this chapter, transferability of the pairwise potential parameterization by Oganov *et al.* (2000) was examined for modeling defects in MgSiO₃ post-perovskite. The ability of this parameterization to accurately compute γ -surfaces, describing the excess energies of generalized stacking faults, which involve atomic configurations far from the equilibrium, was verified by comparing them with previous DFT calculations by Carrez *et al.* (2007) and Metsue and Tsuchiya (2013). Calculations of the γ -surface energies were performed for all possible non-equivalent geometric locations of slip planes breaking different bonds in the post-perovskite structure. In agreement with the *ab initio* studies (Carrez *et al.* 2007; Metsue and Tsuchiya 2013), the slip systems involving the shortest [100] shear vector and the [001](010) system within the glide plane cutting only Mg–O bonds are characterized with very low γ -surface energies. Based on the performed γ -surface calculations, (110) could be considered as further possible slip plane. Reasonable agreement with previous theoretical and experimental results proves the pairwise potential parameterization by Oganov *et al.* (2000) to be valid for further fully atomistic modeling of dislocations in MgSiO₃ post-perovskite.

CHAPTER 4

Dislocations with [100] Burgers Vector

The shortest [100] Burgers vector in MgSiO_3 post-perovskite is expected to play an important role in plastic deformation of this material, and therefore [100] dislocations deserve a particularly detailed and thorough consideration. This chapter summarizes the results of the atomic scale modeling performed for [100] screw and edge dislocations. The dislocation core structures as well as the critical stresses opposed to their glide in (010), (011) and (001) planes in absence of thermal activation (*i.e.* the Peierls stresses) are first computed with the pairwise potential in order to reveal the most important slip systems with [100] Burgers vector. These simulations are followed by calculations of the Peierls barrier, dislocation line tension and kink pair formation enthalpy for the easiest slip system, relying both on the pairwise potential and DFT frameworks.

4.1 Stable dislocation cores

4.1.1 Screw dislocations

Core structure

The core structure of $[100]$ screw dislocations is computed using a quadrupole arrangement of dislocations in a fully periodic atomic array (see Chapter 2, section 2.3.2). The core configurations are obtained relying both on the pairwise potential (Oganov *et al.* 2000) and on the first principle DFT simulations. Both simulation techniques provide similar geometries of $[100]$ dislocation cores, which exhibit two possible configurations, labeled as (I) and (II) hereafter. Figure 4.1 shows the differential displacement (DD) maps (see Chapter 2, section 2.3.1) of these cores, where the relative displacements along $[100]$ between neighboring atoms are represented by arrows between those two atoms. Dislocations (I) and (II) represent pure screw cores without any edge component. The core configuration is centred between two neighbouring Mg atoms and mainly spread in $\{011\}$. In (010) , equivalent stable core configurations are found every $\frac{1}{2}[001]$ lattice repeat, *i.e.* distant by $a' \sim 3 \text{ \AA}$. The cores correspond to alternative variants: (I) - spread in (011) and (II) – spread in $(0\bar{1}1)$. In fact, these core configurations represent a mirror reflection of each other.

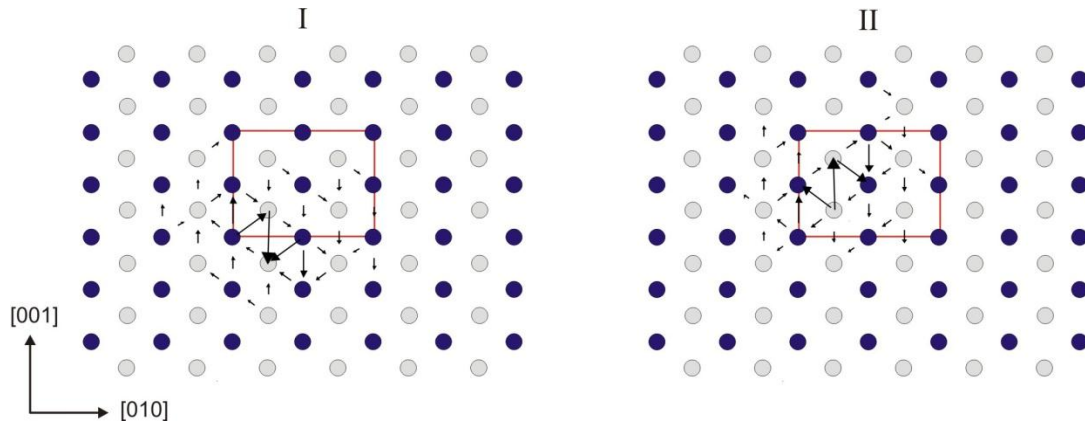


Fig. 4.1. DD maps of $[100]$ screw dislocations viewed along the Burgers vector direction. The anion sublattice is left out. Si atoms are shown with blue balls, Mg atoms – with gray balls; the unit cell – with red rectangle. The arrows between atoms correspond to the $[100]$ component of the relative displacement of the neighboring atoms produced by the dislocation. The length of the arrows is proportional to the magnitude of these components.

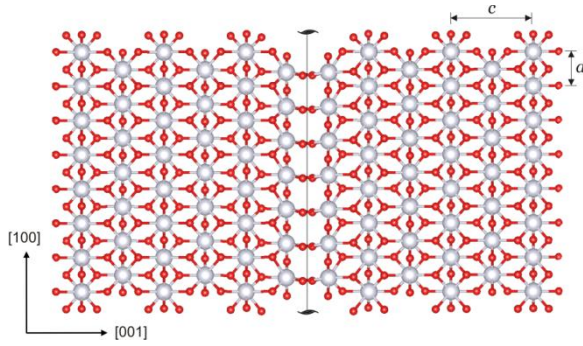


Fig. 4.2. Local structure produced by [100] screw dislocation in (010) MgO layer.

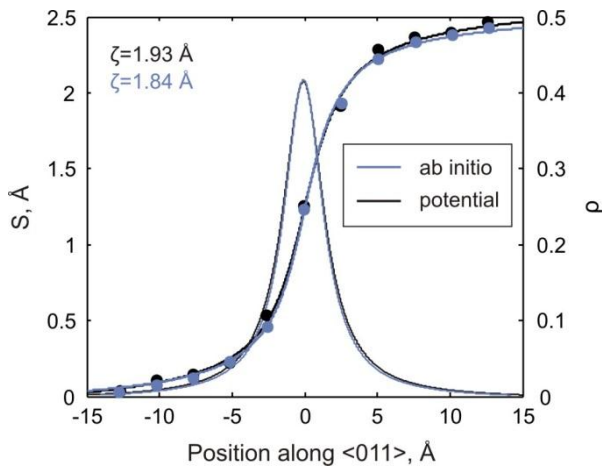


Fig. 4.3. Disregistry function $S(y)$ and the [100] Burgers vector density $\rho(y)$ of the stable screw dislocations (I) and (II) computed for the cation sublattice. Values of the dislocation core half-widths ζ are provided on the plot.

Locations of [100] screw dislocation lines in the PPV structure coincide with the positions of screw axis 2_1 disposed between Mg atoms. Superposition of these elements creates a local structure along the dislocation line similar to the action of a 2 axis instead of the original 2_1 (Fig. 4.2). The dislocation cores tend to spread towards the empty trigonal channels located between Si- and Mg-layers (Fig. 1.1, 4.8). The spreading of the cores is limited by two Si-layers and the distortion produced by the dislocation core notably affects interconnection of Mg-polyhedra only. Figure 4.3 shows the atomic disregistry $S(y)$ and the Burgers vector density $\rho(y)$ along $\langle 011 \rangle$ calculated for the cations sublattice (see Chapter 2, section 2.3.1) based on the structural data acquired from pairwise potential and DFT simulations. Relying on the $S(y)$ and $\rho(y)$ functions, the half-widths ζ of the dislocation cores are found to be 1.93 Å and 1.84 Å for pairwise potential and *ab initio* calculations, respectively (Fig. 4.3). These functions are identical for dislocations (I) and (II).

Dislocation core energy

For atomic systems containing a quadrupole of screw dislocations, the energy of a

dislocation core E_c per Burgers vector unit length can be extracted from the following equation (Ismail-Beigi and Arias 2000):

$$E = E_c + E_{el} = E_c(r_c) + \frac{\mu b^3}{4\pi} \left[\ln\left(\frac{d_1}{r_c}\right) + A\left(\frac{d_1}{d_2}\right) \right], \quad (4.1)$$

where E corresponds to the energy of a straight dislocation line (defined as the total energy of the atomic system once the energy of the perfect crystal is subtracted) which includes the elastic term E_{el} and the energy $E_c(r_c)$ of a dislocation core with radius r_c (commonly taken equal to $2b$) where elastic theory breaks down; μ is an anisotropic shear modulus; d_1 and d_2 are equilibrium distances between the dislocations along y and z axis (see Chapter 2; Fig. 2.11a); $A\left(\frac{d_1}{d_2}\right)$ is a coefficient which includes all dislocation pairwise interactions and which depends only on the $\frac{d_1}{d_2}$ ratio. In this work, for the pairwise potential calculations, all simulation cells are designed in such a way that this ratio remains invariant and equal to 1.007. Thus, all dislocations are equidistant and the $A\left(\frac{d_1}{d_2}\right)$ value is constant for all supercells. Relying on these conditions, eq. (4.1) is applied to evaluate the dislocation core energy using the energies E computed with the pairwise potential for ten different simulation cells, with the dimensions varying from 100 Å to 365 Å along the y and z axis (3840-54000 atoms).

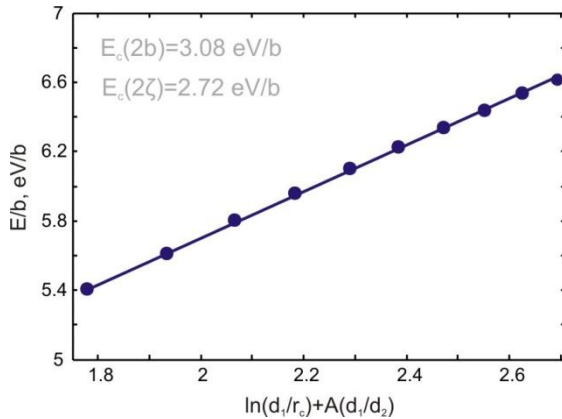


Fig. 4.4. Evolution of the [100] screw dislocations total energy E (including elastic energy E_{el} and the dislocation core energy E_c) as a function of $\ln(d_1/r_c) + A(d_1/d_2)$, deduced from the pairwise potential modeling.

The minimized energy of atomic systems of different sizes is shown on Fig. 4.4 as a function of $\ln(d_1/r_c) + A(d_1/d_2)$. The energies follow a linear trend as predicted by the elastic theory. The calculated value of the A coefficient (including all the effects of the infinite Ewald-like sums of dislocation interactions) is -0.89. The linear fit provides the

dislocation core energy $E_c(2b) = 3.08 \text{ eV/b}$ (1.23 eV/\AA) and the anisotropic shear modulus $\mu = 167 \text{ GPa}$. This value compares well with the modulus $\mu = 173 \text{ GPa}$ estimated from the elastic constants. Atomistic modeling of [100] screw dislocation cores predicts their full width $r_c = 2\zeta = 3.86 \text{ \AA}$, which is less than formal $r_c = 2b$, employed for evaluation of the dislocation core energy. Relying on the 2ζ value deduced from the atomistic modeling, the dislocation core energy is $E_c(2\zeta) = 2.72 \text{ eV/b}$ (1.08 eV/\AA) which is slightly lower than $E_c(2b)$.

For the first principles simulations we only employ the smallest possible atomic array with quadrupolar arrangement of dislocations, distant by 18 \AA along [001] and by 24 \AA along [010]. Since DFT calculations are much more computationally expensive than the pairwise potential approach, we don't increase the simulation cell size as it was described above, but directly define the core energy $E_c(2\zeta)$ from the eq.(4.1), relying on the computed energy $E = 6.76 \text{ eV/b}$, elastic interaction coefficient $A = -0.80$, and anisotropic shear modulus $\mu = 324 \text{ GPa}$. The corresponding dislocation core energy is found to be $E_c(2\zeta) = 4.79 \text{ eV/b}$ (1.93 eV/\AA), which is almost twice higher than that acquired from the pairwise potential modeling.

The core energy can be also generally described as $E_c = \eta \frac{\mu b^3}{4\pi}$, where η is a screening factor (Joós and Zhou 2001). Thus, the energetic characteristics of a dislocation core are strongly dependent on the shear modulus μ and the screening factor η , which significantly vary for different materials. For instance, in metals η is commonly taken as 0.5 (Joos and Zhou 2001). Relying on the computed core energies $E_c(2\zeta)$, deduced from the semi-empirical and *ab initio* calculations, one can find that the η value for [100] screw dislocations in MgSiO_3 post-perovskite is 2, regardless of the level of atomic description. Therefore, the observed discrepancy between the dislocation core energies computed based on the data from different simulation techniques rather results from the difference (characterized by the factor of 2) in the elastic moduli μ (173 GPa vs 324 GPa). The [100] dislocation core energy (normalized per angstrom) computed based on the pairwise potential for MgSiO_3 post-perovskite is comparable with the $\frac{1}{2}[110]$ dislocation core energy $E_c(b) = 1.28 \text{ eV/\AA}$ in MgO computed at 100 GPa with the similar approach (Carrez *et al.* 2015) using the pairwise potential by (Henkelman *et al.* 2005). The close values of the dislocation core energies in MgSiO_3 post-perovskite and in MgO periclase result from

the close values of the elastic moduli (173 GPa vs 195 GPa) and the identical values ($\eta = 2$) of the screening factors.

4.1.2 Edge dislocations

In this study, we mainly focus on [100](010), [100](001) and [100](011) edge dislocations within glide planes characterized with the lowest γ -surface energies, *i.e.*, corresponding to $z_{010} = 0.7$, $z_{001} = 0.65$ and $z_{011} = 0.42$, respectively (see Chapter 3). A dipole arrangement of edge dislocations with positive and negative Burgers vectors in a fully periodic supercell is commonly used for metals (Chang *et al.* 1999, Bulatov *et al.* 1999, Chang *et al.* 2002). However, in the post-perovskite structure, edge dislocations lying on the same glide plane with positive and negative Burgers vectors³ have different geometries. Thus, a fully periodic dipole cell containing two geometrically identical glide planes would incorporate two different dislocation cores. Reciprocally, a periodic dipole configuration containing two identical dislocation cores of opposite sign would not be charge neutral. Therefore, edge dislocations are modeled using slab geometries of simulation cells (see Chapter 2, section 2.3.2) employing the empirical potential.

Due to the location of the (010) glide plane at $z_{010} = 0.7$ (affecting only Mg-O bonds), all Si atoms in the dislocation core keep octahedral coordination (Fig. 4.5a). Edge dislocation with positive Burgers vector is characterized with a lack of O for Mg coordination in the dislocation core, which results in the presence of sixfold and sevenfold coordinated Mg along the dislocation line. On the contrary, in a dislocation core with negative Burgers vector, there are extra O atoms increasing coordination of some Mg atoms located along the dislocation line up to 10. Both dislocation cores are very symmetric.

Edge dislocations lying on the (001) plane ($z_{001} = 0.65$) are also very symmetric. The chosen (001) glide plane is located in the structure in such a way that all Mg-polyhedra below this plane remain eightfold coordinated for both dislocations with positive and negative Burgers vectors, whereas coordination of Mg above the glide plane is going to be incomplete. The edge [100](001) dislocations with positive Burgers vector retain the

³ Edge dislocation with positive Burgers vector corresponds to the configuration where atomic extra half plane is located above the glide plane, while dislocations with negative Burgers vector - below the glide plane.

favorable octahedral coordination of Si (Fig. 4.5b). Inside the dislocation core with negative Burgers vector, there are Si atoms with incomplete fivefold coordination which also can be described as $(5+2)$ while taking into account next two closest ($\sim 2.4 \text{ \AA}$) O atoms (Fig. 4.5b). Thus, for the dislocation cores with positive and negative b , distortions of Mg-polyhedra are quite similar, while Si changes coordination only in the dislocation core with negative Burgers vector.

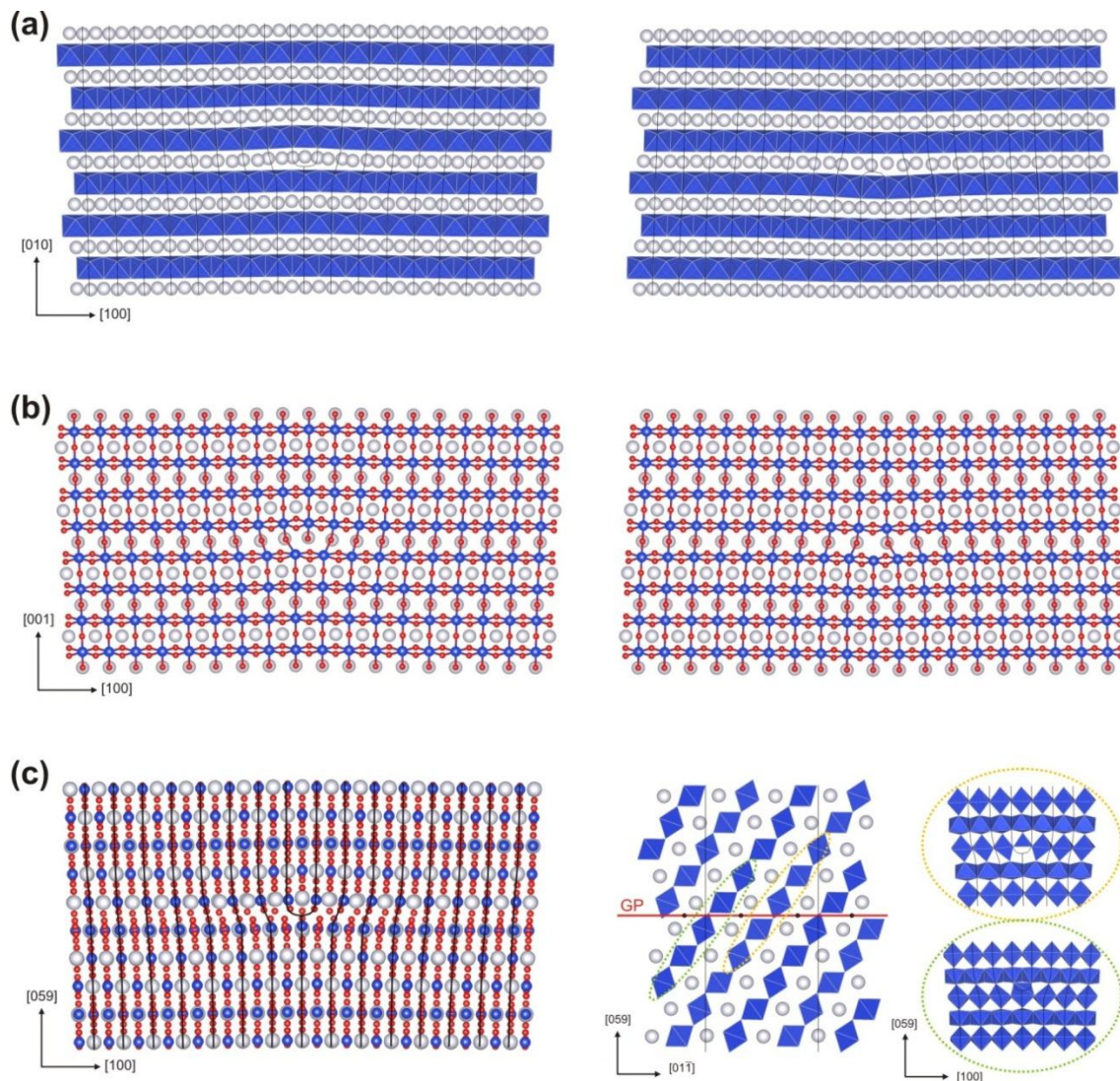


Fig. 4.5. Atomic structure of the relaxed $[100](010)$ (a), $[100](001)$ (b) and $[100](011)$ (c) edge dislocation cores. Right panel of (c) illustrates the location of (011) glide plane and inversion centers belonging to it.

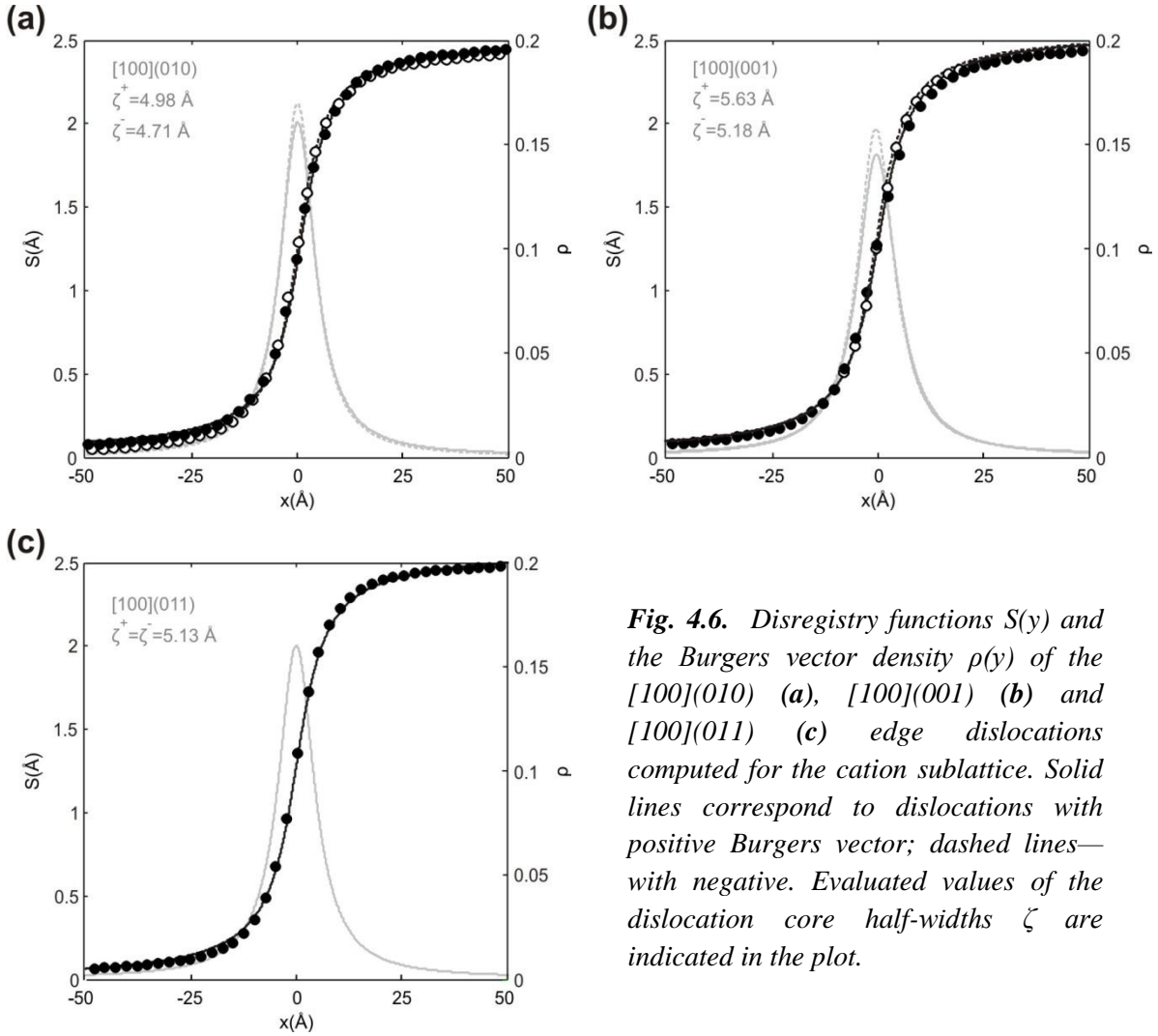


Fig. 4.6. Disregistry functions $S(y)$ and the Burgers vector density $\rho(y)$ of the [100](010) (a), [100](001) (b) and [100](011) (c) edge dislocations computed for the cation sublattice. Solid lines correspond to dislocations with positive Burgers vector; dashed lines—with negative. Evaluated values of the dislocation core half-widths ζ are indicated in the plot.

The chosen (011) glide plane located at $z_{011} = 0.42$ is the only plane considered in this work which has a symmetric position in the post-perovskite structure. This plane contains inversion centers (Fig. 4.5c), which results in identical core structures for dislocations with negative and positive Burgers vectors. Incorporation of atomic extra half-plane leads to appearance of an extra O ligand for the Si atom below the plane and lack of one O ligand for the Si atom above the glide plane (Fig. 4.5c). The incomplete fivefold coordination of the latest is similar to the one observed in the [100](001) dislocation core with negative Burgers vector.

The computed disregistry functions $S(y)$ and their derivatives $\rho(x)$ have symmetric shapes for all edge dislocations described above, consistent with their core structures. All [100] edge dislocations are characterized by the dislocation half-width ζ very close to $2b$

(Fig. 4.6a–c; Table 4.1) which is almost three times larger than for the [100] screw dislocations.

4.2 Anisotropic lattice friction: Peierls stress calculations

4.2.1 Glide of screw dislocations

Glide of the [100] screw dislocations is investigated relying on the pairwise potential modeling and triggered by applying a simple shear ε_{xy} in order to increase stress in a glide plane of interest normal to z axis (see Chapter 2, section 2.3.3). When stress reaches a critical value, *i.e.*, the Peierls stress value σ_p , the straight dislocations start gliding. Monitoring the system stress field and the disregistry function of the dislocation allows determining the Peierls stress value (Fig. 4.7a). Motion of all dislocations within the quadrupole system is observed to start simultaneously. Dislocations with opposite Burgers vectors move toward each other and eventually annihilate. Lattice friction (described by σ_p) displays a highly anisotropic behavior: Peierls stresses are 1 GPa and 17.5 GPa for glide in (010) and (001), respectively. The observed zigzag path of the [100](010) gliding (Fig. 4.8) explicitly

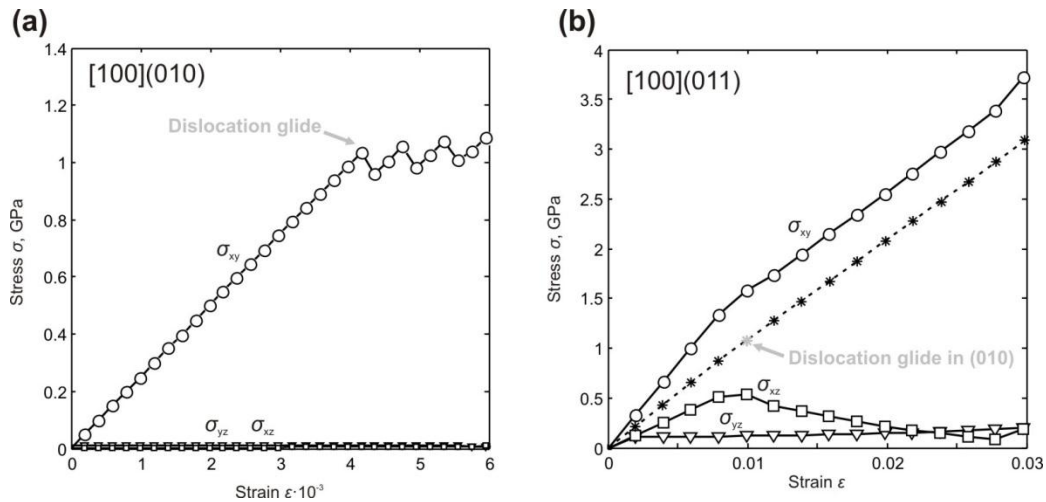


Fig. 4.7. Evolution of the σ_{xy} , σ_{xz} and σ_{yz} stress components (a) while applying a simple shear ε_{xy} to an orthorhombic cell in order to trigger [100] screw dislocation glide in (010); and (b) to a monoclinic supercell in order to activate [100](011) system. For the monoclinic configuration (b), the resolved stress on (010) is shown with the dashed line.

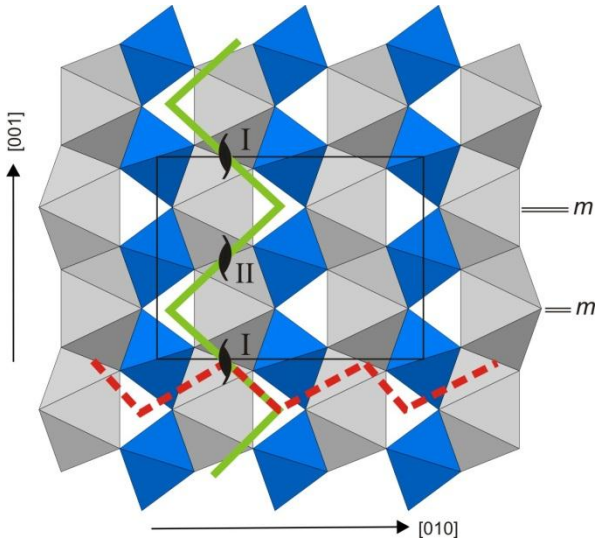


Fig. 4.8. Observed paths of $[100]$ screw dislocations glide in (010) and (001) . The easiest (010) glide is shown with a solid green line; the difficult (001) glide—with a dashed red line. Location of stable screw dislocations (I) and (II) in the structure are given with “screw” signs; location of mirror planes m_{001} between these dislocations are indicated as “m”.

reproduces the geometry of dislocation core spreading while switching from dislocation (I) spread in (011) to its symmetric replica (II) spread in $(01\bar{1})$ (Fig. 4.1). In this study, this path is not classified as a cross-slip mechanism because the general direction of glide remains the same and clearly corresponds to (010) . The remarkably easy $[100](010)$ glide occurs strictly within a Mg-O layer which is rather correlated with the $[100](010)$ low energy γ -line ($z_{010} = 0.7$) cutting only Mg-O bonds. The observed motion in (001) plane (Fig. 4.8) also matches the lowest energy γ -line for this system ($z_{001} = 0.65$).

Modeling dislocation glide in (011) , *i.e.*, in the plane where the dislocation core exhibits a tendency for spreading, requires rebuilding a simulation cell in such a way that lattice vectors a_1 , a_2 and a_3 are aligned with $[059]$, $[100]$ and $[01\bar{1}]$, respectively. There is a monoclinic angle 89.95° between $[059]$ and $[01\bar{1}]$ which is very close to an orthogonal configuration. Applying a strain component ε_{xy} to the monoclinic cell (characterized with an elastic tensor containing 13 independent components) results here in an increase in several stress components (Fig. 4.7b). During the deformation, the σ_{xy} component, needed to activate glide in (011) , increases much faster than the residual σ_{xz} and σ_{yz} components (Fig. 4.7b). However, whereas the system geometry is built to maximize the resolved shear stress in (011) , the close orientation of (010) results in a nonzero resolved shear stress in this plane as σ_{xy} increases. Due to the low lattice friction of the $[100](010)$ system, it turns out that the dislocations always start gliding in (010) instead of in the desired (011) plane when the resolved stress on (010) (resulting from σ_{xy} and σ_{xz}) reaches the critical value of

1 GPa (Fig. 4.7b). A lowest bound of the Peierls stress needed for glide in (011) can be evaluated from the resolved stress on (011) based on calculations for [100](001) glide. For this orientation, the resolved shear stress on (010) is null, preventing dislocations to glide in this plane. The resolved stress on (011) reached 10.4 GPa without promoting glide in (011). Our simulations clearly demonstrate that for [100] screw dislocations, the Peierls stress in (010) is much smaller than in (011) ($\sigma_p > 10.4$ GPa) and in (001) ($\sigma_p = 17.5$ GPa).

The conservative motion of [100] screw dislocations was also explored using simulation supercells with slab geometry (see Chapter 2, section 2.3.2). These calculations lead to a dislocation core geometry identical with that observed in a quadrupole cell, and Peierls stresses of 1.1 GPa and 17.5 GPa for [100](010) and [100](001), respectively. Modeling screw dislocation glide in (011) plane produces the same effect of activating [100](010) glide. These results compare well with the simulations performed using fully periodic atomic arrays which shows the slab-type simulation cells to be appropriate for dislocation modeling.

4.2.2 Glide of edge dislocations

The motion of the [100] edge dislocations is studied by applying a simple shear strain ε_{yz} in order to force a dislocation line lying along x to glide in the plane normal to z (see Chapter 2, section 2.3.3). As expected, [100] edge dislocations are much more mobile than screw dislocations. In general, they all are characterized by Peierls stresses one order of magnitude lower than those, estimated for [100] screw dislocations, which indicates that the latter will control plastic deformation along [100] in MgSiO₃ post-perovskite. Glide of [100](010) dislocations with both positive and negative Burgers vectors occurs at very low stresses $\sigma_p < 0.1$ GPa. The lattice friction of other dislocations is somewhat higher but still very low. Thus, the Peierls stresses estimated for the [100](001) edge dislocations with positive and negative Burgers vectors are 0.1 and 0.15 GPa, respectively. Clearly, this difference is mainly caused by different level of the Si-octahedra distortions in the dislocation cores. The [100](011) edge dislocations start gliding at $\sigma_p \sim 0.12$ GPa. In contrast to [100] screw dislocations, glide of [100] edge dislocations in (001) and (011) occurs as easily as in (010).

4.3 Peierls barrier and MEP of [100](010) screw dislocation glide

Based on the anisotropic lattice friction in MgSiO_3 post-perovskite computed with the pairwise potential (section 4.2), we focus further on the [100](010) screw dislocation glide, which will account for the most of the plastic strain, and combine empirical potential and DFT simulation techniques.

4.3.1 Pairwise potential calculations

Although DFT represents high accuracy calculations, we first employ the pairwise potential to compute the minimum energy path (MEP) between two stable core configurations (I) and (II) in (010). The MEP between them is computed using the a (NEB) method, as described in Chapter 2, section 2.1.3. In the initial quadrupole configuration, all four dislocations are equidistant and located at Peierls valleys (I); in the final state two dislocations of the opposite sign remain in the initial Peierls valleys (I) while two other dislocations are displaced to the next valleys (II). For such a configuration, the performed NEB calculations indicate successive motion of the two displaced dislocations. The corresponding energy barrier is provided on Fig. 4.9.

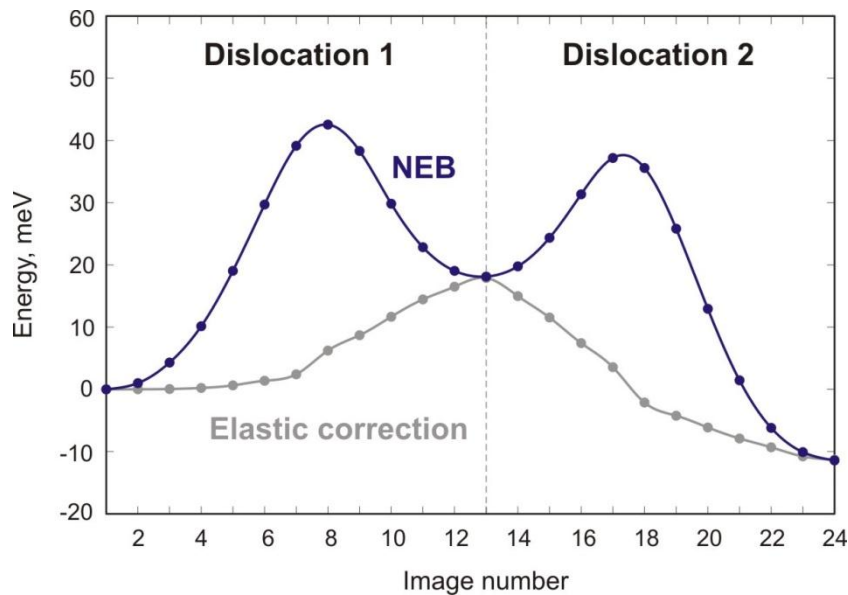


Fig. 4.9. Energy barriers deduced from the NEB calculations and the corresponding elastic interaction energy.

For each atomic configuration along the MEP, the elastic interaction term is estimated from the anisotropic elastic theory (Clouet 2011) and subtracted from the energy computed with the NEB method (Fig. 4.9). In order to account for the effect of applied stress σ_a and increase the corresponding σ_{xz} stress component in the xy glide plane, a strain component ε_{xz} resulting in a certain σ_a value is applied. Figure 4.10a illustrates the resulting energy barriers $\Delta H_p = V_p - \sigma_a b a'$, opposed to the motion of one dislocation, as a function of a dislocation line reaction coordinate in projection on (010) glide plane along $\frac{1}{2}[001]$. For each energy curve, reaction coordinates 0 and 1 correspond to the initial and final positions of a stable dislocation configuration at a given stress σ_a and intermediate reaction coordinates are defined by extracting the exact position of each dislocation line image from its disregistry function (eq. 2.13).

With no stress applied, the MEP reproduces the peculiar $\langle 011 \rangle$ zig-zag trajectory reported in the previous section (see Fig. 4.8). The maximum peak of the Peierls potential of 39 meV/b is related to the MEP dislocation image when trajectory in (011) switches to $(0\bar{1}1)$. Due to the very low lattice friction, once $\sigma_a \geq 400$ MPa is applied, the dislocation

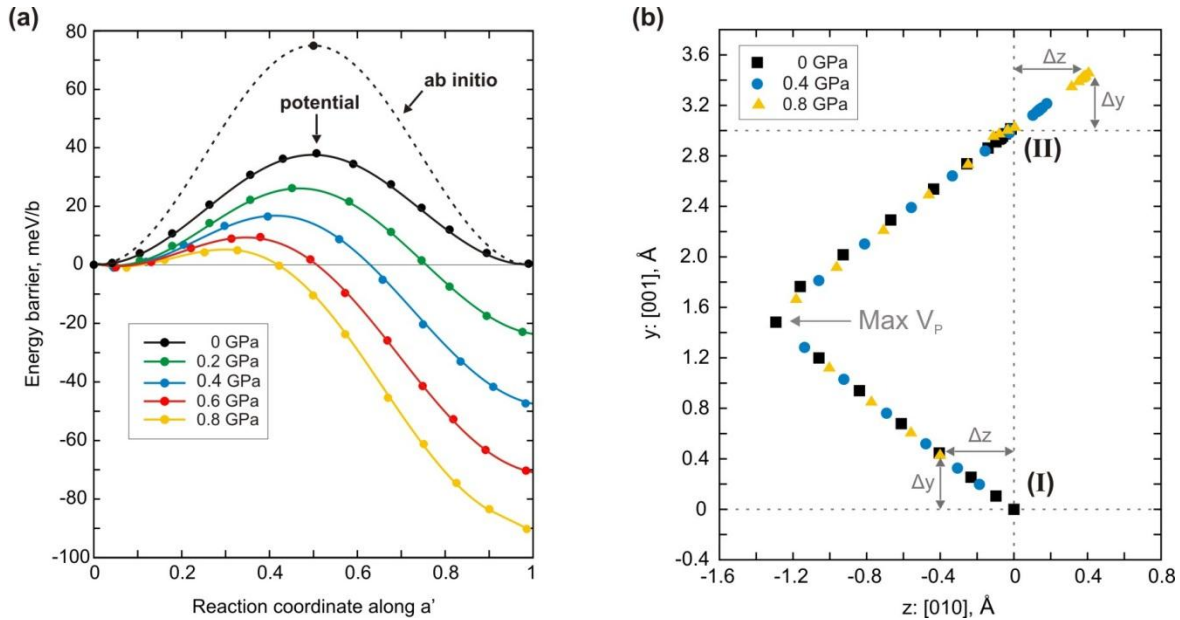


Fig. 4.10. (a) Peierls barrier V_p (black line) calculated for $[100](010)$ with the pairwise potential (solid line) and DFT (dashed line). Evolution of the energy barrier with applied stress $\Delta H_p = V_p - \sigma_a b a'$, deduced from NEB calculations with pairwise potential, is provided in colour. (b) MEP of a straight $[100]$ screw dislocation gliding from the Peierls valley (I) to (II) and its evolution with applied stress.

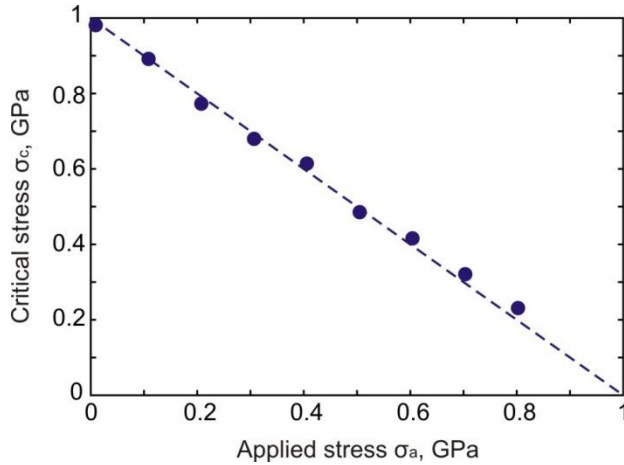


Fig.4.11. Evolution of the critical stress σ_c with applied stress σ_a .

starts climbing the potential and the equilibrium position of the dislocation line is displaced from the valley (I) towards (II) by Δz along [010] and by Δy along [001] (Fig. 4.10b). This means, that under an applied stress, the path followed by the dislocation in (011) is not any more symmetric to that in (0 $\bar{1}$ 1).

The critical stress σ_c required to overcome the energy barrier ΔH_P , which includes contributions of the Peierls potential V_P and of the work of the applied stress σ_a , can be calculated as maximum of $dH_P/b^2 dy$. With no stress applied, $\sigma_c \sim 1$ GPa corresponds to the Peierls stress and compares well with the σ_p value computed as the critical stress needed to trigger [100] dislocation glide in (010) (see section 4.2.1). The estimated σ_c are shown as a function of applied stress σ_a on Fig. 4.11. The linear relation between σ_c and σ_a indicates that the observed asymmetry of MEP trajectory at applied stress does not have a strong effect on the critical stress needed to overcome the energy barrier.

4.3.2 DFT calculations

In order to estimate the Peierls barrier V_P from the first principles, we reconstruct the high-energy dislocation core associated with the maximum of the Peierls barrier (deduced from NEB simulations with empirical potential) and employ it for DFT simulations (Fig. 4.12). This high energy configuration is associated with 77.7 meV/b energy barrier (Figure 4.9a). Based on these results, the Peierls stress σ_p can be estimated from the maximum slope of the sinusoidal Peierls potential. Thus, DFT calculations lead to $\sigma_p = 2.1$ GPa, which is twice larger than the corresponding stress estimated with empirical potential.

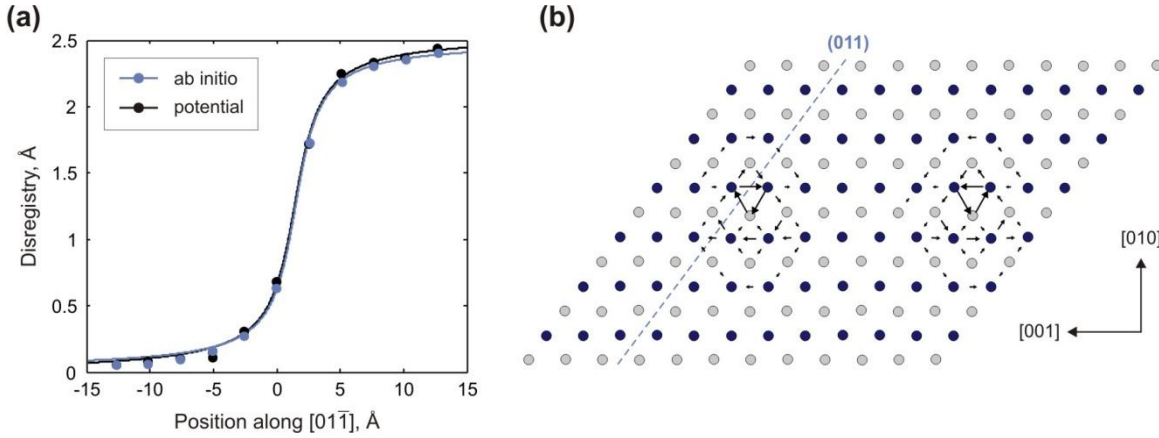


Fig.4.12. (a) Disregistry functions $S(y)$ of the high energy [100] screw dislocation core computed for the cation sublattice in (011) plane based on the structural data acquired from DFT and pairwise potential simulations (performed for atomic arrays of the same size).

(b) DD-plot map of the high energy [100] dislocation core computed with DFT. Si atoms are shown in blue; Mg atoms – in gray; anion sublattice is left out (for clarity). The arrows between atoms correspond to the [100] component of the relative displacements of the neighboring atoms. The length of the arrows is proportional to the magnitude of these components.

Based on the pairwise potential modelling, the optimum size of a quadrupole simulation cell is found to be $1b \times 100 \text{ \AA} \times 100 \text{ \AA}$ (*i.e.* the dislocation cores are distant by 50 \AA), which is large enough to avoid ineligible size effects on the computed Peierls barrier V_P and Peierls stress σ_p . However, for DFT simulations, we are restricted to the smallest atomic array ($1b \times 36 \text{ \AA} \times 48 \text{ \AA}$ quadrupole reduced into a twice smaller dipole containing 360 atoms) where the dislocations are distant by only 18 \AA along [001] and by 24 \AA along [010]. Relying on the size effect deduced from the pairwise potential modeling, one can expect that the energy barrier V_P and, consequently, the corresponding Peierls stress σ_p , computed with DFT for such a small atomic array is $\sim 10\%$ underestimated.

The apparent discrepancy (the factor of two) between the Peierls stress σ_p computed with the pairwise potential and DFT is likely related to the drawback of the potential parameterization used in this study. Indeed, both simulation techniques provide very close dislocation core structures both for stable and high energy configurations (Fig. 4.3; 4.12), but the empirical potential underestimates the elastic stiffness coefficients C_{55} and C_{66} by a factor of 2 (see Chapter 2, Table 2.2), and consequently, the corresponding anisotropic

shear modulus μ (173 GPa vs 324 GPa) of the post-perovskite. Qualitatively, one still finds the ratio $\sigma_p/\mu \sim 5 \cdot 10^{-3}$, regardless of the level of atomic description.

4.4 Line tension of [100](010) screw dislocations

To compute the line tension Γ describing the stiffness of a dislocation line, the energy cost associated with a dislocation bow-out consistent with the first stage of kink-pair formation should be evaluated. Bending a dislocation line requires breaking up the $1b$ translational symmetry of the simulation cell. Thus, the length of the supercell along the dislocation line is increased up to $2b$. We consider a dislocation line which consists of two segments of length b : the segment S_1 remains in the Peierls valley (I) while another segment S_2 starts bowing out towards to the next valley (II) as it is shown on Fig. 4.13c. In order to compute this process at the atomic scale, the evolution of atomic displacements Δx along [100] during the dislocation glide from (I) to (II) is analysed relying on the MEP structural information obtained from the NEB calculations (see section 4.3.1). Since DFT and pairwise potential modelling provide very close configurations of dislocation cores (Fig. 4.3; 4.12), we employ the same MEP trajectory to mimic a dislocation line bending both with DFT and pairwise potential. Dealing with a complex material, we mostly focus on cation sublattice and allow anions to adapt to the local displacement of cations.

Along the MEP, one Mg and four Si atoms exhibit the largest displacements Δx along the dislocation line compared to other cations in the crystal (Fig. 4.13a, b). The selected Mg atom is located right between the two Peierls valleys and bears the maximum displacement amplitude (about 0.8 Å). Maximum Δx amplitude of the four Si atoms is twice smaller (Fig. 4.13b). Once the evolution of atomic positions along the MEP is defined, one can create the dislocation bow-out while applying the exact displacements Δx consistent with the MEP (under zero applied stress) to the selected atoms belonging to the segment S_2 of a dislocation line (Fig. 4.13d). The corresponding cations of the segment S_1 are fixed to their regular positions in the Peierls valley. Practically, it means that for these atoms, the degrees of freedom along the dislocation line are constrained. After structural relaxation, the exact location of segments S_1 and S_2 are defined through computing the disregistry function $S(y)$ (eq. 2.13) at each step of the line “bending”. The computed change

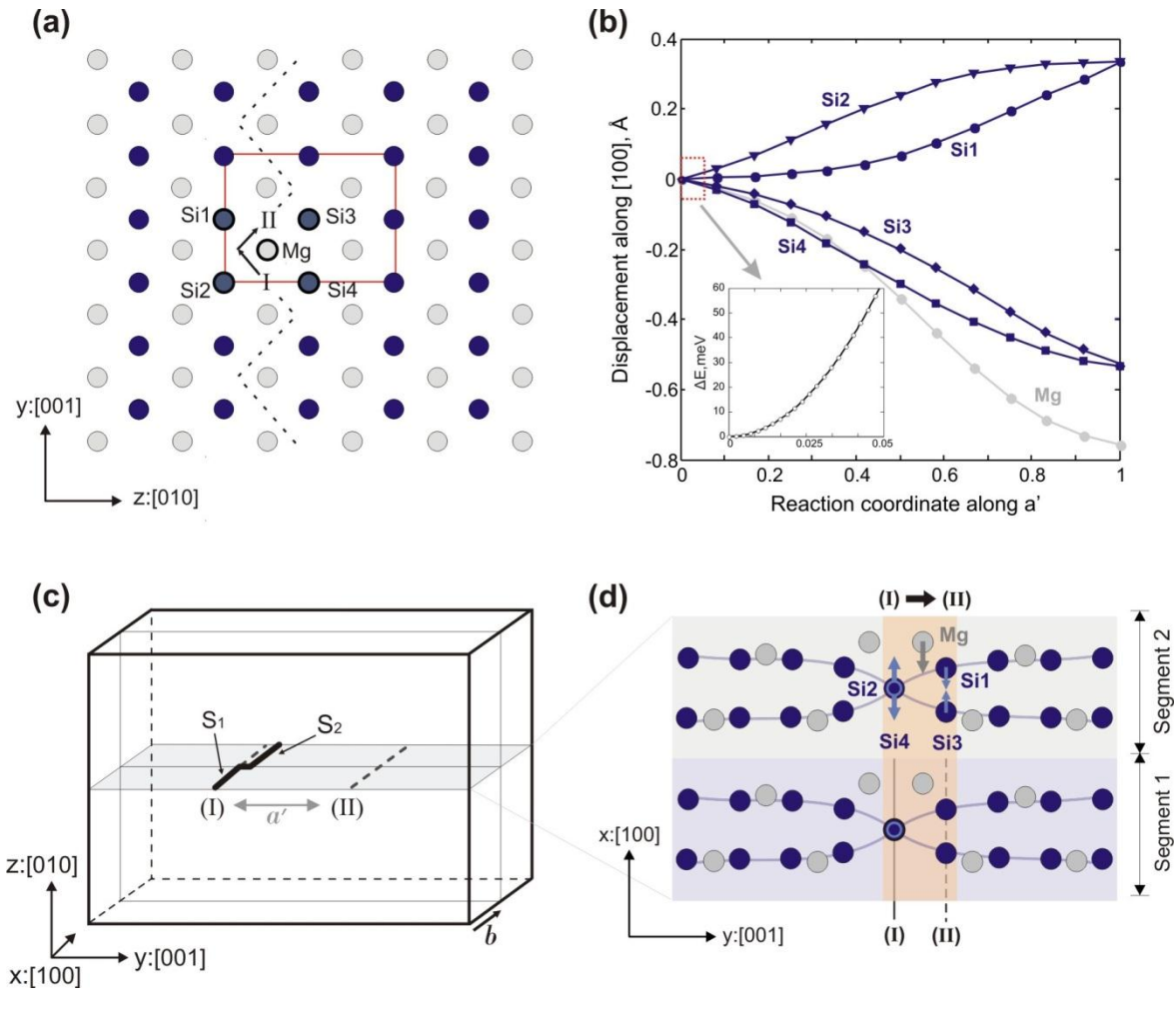


Fig.4.13. Line tension calculation scheme:

- (a) The five cations, four Si and one Mg, that exhibit the biggest displacements along [100] during dislocation glide are labelled here. Si atoms are indicated by blue spheres, Mg by grey, the anion sublattice is left out for clarity, the dashed line indicates the MEP followed by the dislocation during its glide, and the unit cell is indicated by the red rectangle.
- (b) Atomic displacements along [100], deduced for the five selected cations from NEB simulations. The plot provides displacements for a screw dislocation with positive Burgers vector; in the case of negative Burgers vector, atomic displacement occurs in the inverse way.
- (c) Schematic illustration of dislocation line bending, mimicking the instant of kink-pair formation, in a $2b$ simulation cell. Glide plane (010) is highlighted in grey.
- (d) Local structure of the cation sublattice produced by the screw dislocation (I) in the (010) plane. To create a bow-out, degrees of freedom along [100] are restricted for the cations located in the pink area: in segment S_1 , the selected atoms are fixed to their regular positions in the Peierls valley (I), while the corresponding atoms of segment S_2 are forced to follow up to 5% of the MEP along a' towards the next Peierls valley (II), as indicated by the arrows. The associated increase in elastic energy ΔE is provided in (b)

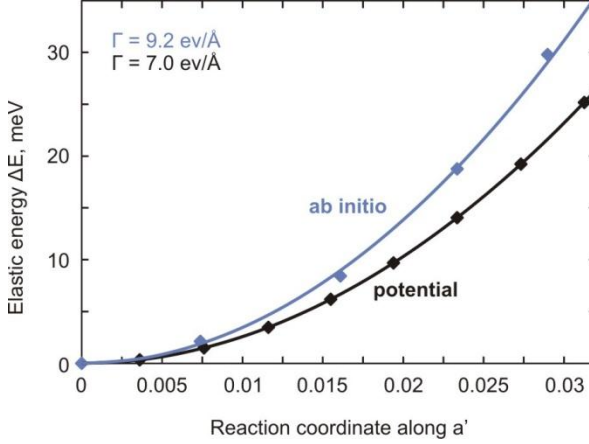


Fig.4.14. Elastic energy ΔE_{LT} inferred from the pairwise potential and DFT simulations performed for the reduced $2b$ dipole cell containing 720 atoms. The corresponding line tension Γ values are provided on the plot.

in energy, $\Delta E_{LT} = \Delta E - bV_P(Y_1) - bV_P(Y_2) = \frac{\Gamma}{b}(Y_2 - Y_1)^2$ related to the gradual disposition of the line segment S_2 is shown on Fig. 4.13b and Fig. 4.14 as a function of the reaction coordinate along [001]. For the large simulation cell ($2b \times 100 \text{ \AA} \times 100 \text{ \AA}$) employed for the pairwise potential simulations, fitting the curvature of quadratic function ΔE_{LT} (Fig. 4.13b) provides the line tension $\Gamma = 7.1 \text{ eV/\AA}$. Similar simulations performed for the reduced dipole cell (720 atoms) provide 9.2 eV/\AA for DFT simulations and 7.0 eV/\AA for empirical potential (Fig.4.14). Thus, based on the values deduced from the pairwise potential modelling, the size effect for larger atomic arrays is about +2%.

The anisotropic line tension $\Gamma_{el} = 2.08 \text{ eV/\AA}$, calculated within Stroh formalism (Stroh 1958) using the set of elastic constant C_{ij} of PPV (Carrez *et al.* 2007) computed with the same GGA pseudopotentials as we employ in this work, is notably lower. Previous studies of bcc metals based on a similar simulation approach for computing LT at atomic scale (Proville *et al.* 2013; Dezerald *et al.* 2015) report comparable discrepancies between the LT values predicted atomistically and from the elastic theory. Indeed, the latter does not account for the large effect of the dislocation core contribution which leads to drastically underestimated Γ_{el} values.

4.5 Kink-pair formation on [100] screw dislocations

The performed atomic scale simulations clearly demonstrate that [100] screw dislocation glide in MgSiO_3 post-perovskite is associated with a very low Peierls stress ($\sigma_p/\mu \sim 5 \cdot 10^{-3}$) and that the corresponding Peierls barrier is small compared to the

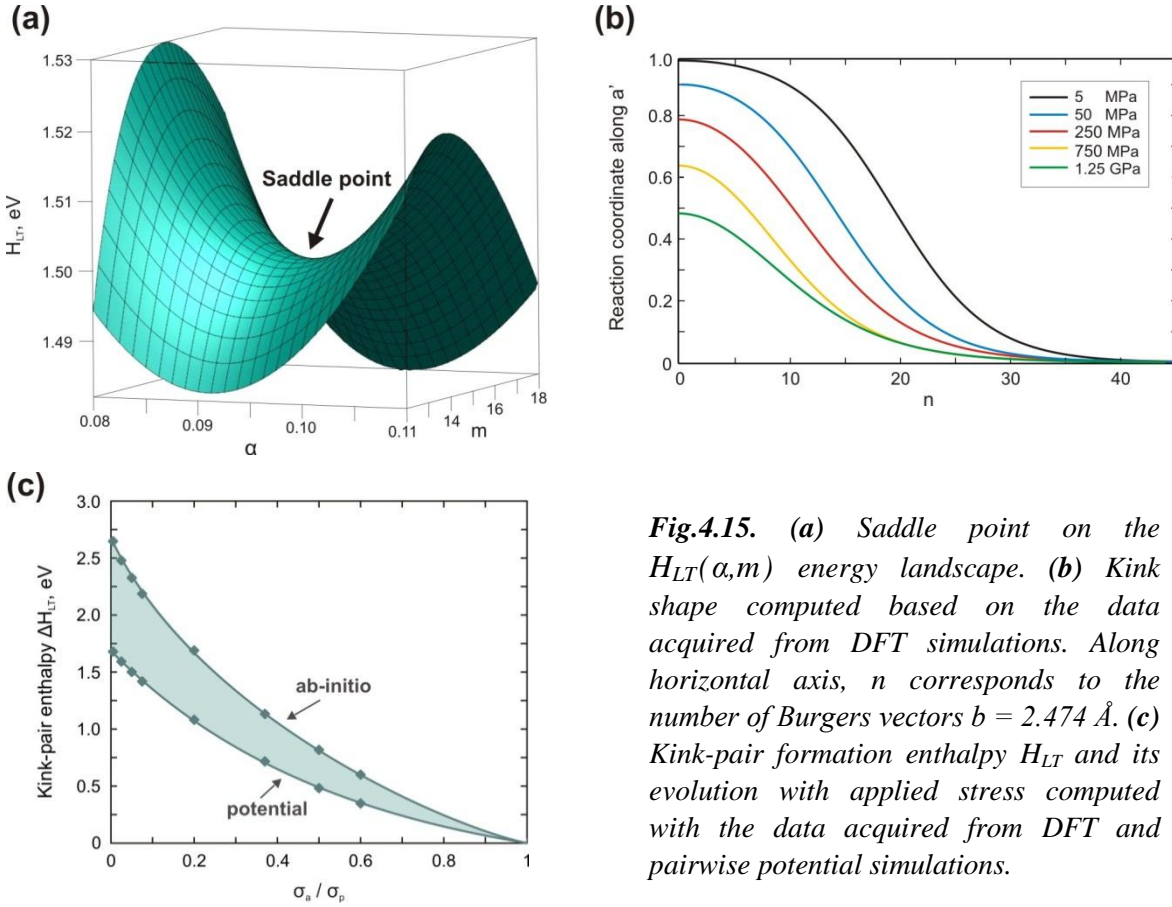


Fig.4.15. (a) Saddle point on the $H_{LT}(\alpha, m)$ energy landscape. (b) Kink shape computed based on the data acquired from DFT simulations. Along horizontal axis, n corresponds to the number of Burgers vectors $b = 2.474 \text{ \AA}$. (c) Kink-pair formation enthalpy H_{LT} and its evolution with applied stress computed with the data acquired from DFT and pairwise potential simulations.

dislocation self-energy ($V_P^{max}/E_c(2\zeta) \sim 1.5 \cdot 10^{-2}$). These characteristics suggest employing the linearized line tension (LT) model (see Chapter 2, section 2.4.2) to describe the kink-pair formation mechanism on [100](010) dislocations.

Once line tension Γ is computed at atomic scale and the Peierls barrier V_P is known, the equilibrium kink-pair shape at a given stress and the corresponding critical kink-pair enthalpy H_{LT} can be calculated using eq. (2.17). To solve eq. (2.17), we rely on a trial function $y(x)$ that describes the equilibrium shape of a symmetric kink-pair based on a combination of hyperbolic tangents (Joós and Duesbery 1997):

$$y(x) = \frac{1}{2}a'[\tanh(\alpha(x+m)) - \tanh(\alpha(x-m))], \quad (4.2)$$

where a' is the periodicity of the Peierls potential and α and m are variable parameters, defining the widths and the height of the kink slope. The saddle point on $H_{LT}(\alpha, m)$ energy landscape (Fig.4.15a) ultimately defines both the enthalpy H_{LT} and the equilibrium kink-pair configuration $y(x)$. The equilibrium kink shape (Fig.4.15b) is characterized by

extremely large width of about $35-40b$ (~ 100 Å) resulting from the very low Peierls barrier. Under applied stress, this width changes moderately while the height of the kink-pair decreases rapidly as the straight part of the dislocation line is moved upwards on the Peierls barrier. It should be pointed out that such wide kink shape fully justifies our choice of using the LT model with respect to unreasonable direct atomistic computation of bowed configuration lines which would require extremely large simulation cells. Figure 4.15c shows the evolution of the computed enthalpy H_{LT} as function of the applied stress σ_a . As one expects from dislocation theory (Hirth and Lothe 1982), the kink-pair enthalpy is maximum under zero stress with a value below 3 eV, corresponding to twice the energy of a single kink H_k , and it vanishes when the applied stress is equal to the Peierls stress. The normalized kink-pair enthalpy $2H_k/\mu b^3$ is found to be $\sim 3 \cdot 10^{-6}$, confirming the relatively low lattice friction born by the [100](010) slip system in MgSiO₃ post-perovskite, despite the high confining pressure of 120 GPa.

4.6 Summary

In this chapter we characterized atomic structure, anisotropic lattice friction and computed the key parameters describing thermally activated mobility of [100] dislocations. In order to reveal the most important slip system, calculations were first performed relying on the chosen pairwise potential parameterization (Oganov *et al.* 2000). The [100] screw dislocations have compact dislocation cores with a slight tendency for spreading in {011} plane (half-width $\zeta = 1.9$ Å). The [100] edge dislocation cores exhibit compact cores with a half width close to $2b \sim 5$ Å, regardless the spreading plane. Lattice friction opposed to the [100] dislocation glide in (010), (001) and (110) planes is found to be highly anisotropic. Remarkably low value of Peierls stress $\sigma_p = 1$ GPa is found for [100] screw dislocation glide in (010) within MgO layer, while glide in (001), normal to the structural layering, requires almost 18 times bigger stress values. Mobility of the [100] edge dislocations is systematically higher than that of the screw dislocations. The Peierls stress opposed to the [100] edge dislocation glide is found to be in the order of 0.1 GPa, regardless of the glide plane orientation. Thus, based on the performed pairwise potential modeling, [100](010) screw dislocation glide should play an important role for plastic deformation along [100].

Relying on this conclusion, further simulations were performed for the [100] screw dislocations both within pairwise potential and DFT frameworks in order to address the essential parameters (kink-pair shape and kink-pair formation enthalpy H_{2k}) describing thermally activated [100](010) glide. For that purpose, the associated Peierls barrier V_P and line the tension Γ (describing stiffness of [100] screw dislocation line) were calculated at the atomic scale. These parameters were further integrated into the one-dimensional line tension (LT) model, commonly used for low lattice friction materials. Under zero stress, $V_P = 77.7$ meV/ b and $\Gamma = 9.2$ eV/Å from DFT simulations lead to a kink-pair enthalpy $H_{2k} = 2.69$ eV and equilibrium kink shape characterized by a very large width of ~ 100 Å.

CHAPTER 5

Dislocations with [001] Burgers Vector

This chapter describes the results of the atomic scale modeling performed for dissociated [001] screw and edge dislocations in MgSiO_3 post-perovskite with the pairwise potential. Full atomistic modeling provides insights into the complex atomic structure of the dislocation cores and peculiarities of their dissociation, which allows estimating the associated γ -energies. Stable dislocation core configurations are further employed to compute the lattice friction opposed to the glide of straight [001] dislocations at 0 K and to estimate the energy of an isolated kink-pair, *i.e.* the kink pair formation enthalpy at zero applied stress.

5.1 Structure of stable [001] dislocation cores

5.1.1 Screw dislocations

Dislocation core structures of [001] screw dislocations are investigated using the so-called “slab” simulation cell geometries (Fig. 2.11b in Chapter 2), fully periodic along the x and y axis aligned with the dislocation line and with the core spreading directions, respectively, and characterized by the fixed borders along the third direction. Structural relaxation of perfect [001] Volterra dislocations systematically results in their spontaneous dissociation into two symmetric partials in the (010) plane separated by a stacking fault. The atomic structure of the relaxed screw dislocation core along [010] direction is illustrated on Fig. 5.1 where the stacking fault between the two partials can be clearly distinguished.

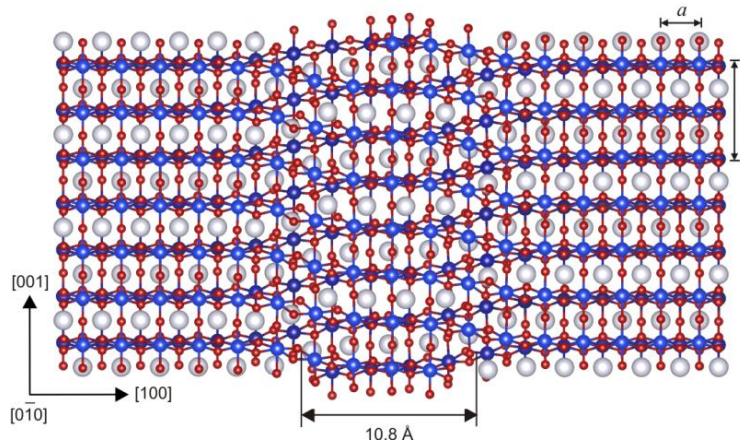


Fig. 5.1. Atomic structure of the stable [001] screw dislocation core in the (010) plane. Si atoms are shown with blue balls, Mg – with white, and O – with red. The distance R between the two partials and the unit cell parameters a and c are indicated with arrows.

The corresponding differential displacement (DD) map (viewed along the dislocation line direction) is presented on Fig. 5.2. The largest atomic displacements are localized in (010) plane between the Mg- and Si-layers. Quantitative characteristics of the dislocation core are derived from its disregistry function $S(y)$ computed with eq. (2.13) for the cation sublattice and its derivative $\rho(y)$ describing distribution of the [001] Burgers vector density in the glide plane. Symmetric shapes of both functions (Fig. 5.3a) indicate

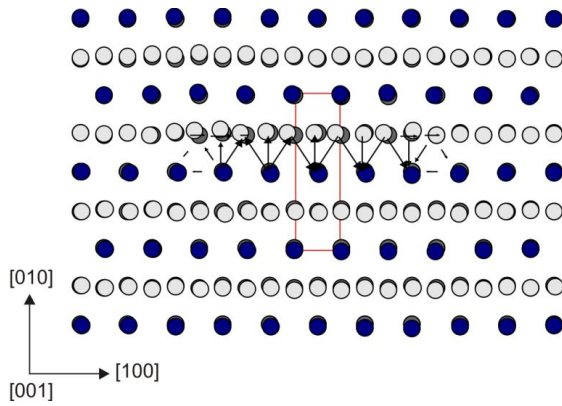


Fig. 5.2. Differential displacement map of the stable [001] screw dislocation core. The anion sublattice is left out; Si atoms are shown with blue balls; Mg atoms – with light grey balls; the unit cell – with red rectangle. Atomic positions in a perfect crystal are displayed in dark grey. The lengths of arrows are proportional to the magnitude of the corresponding atomic displacements along [001].

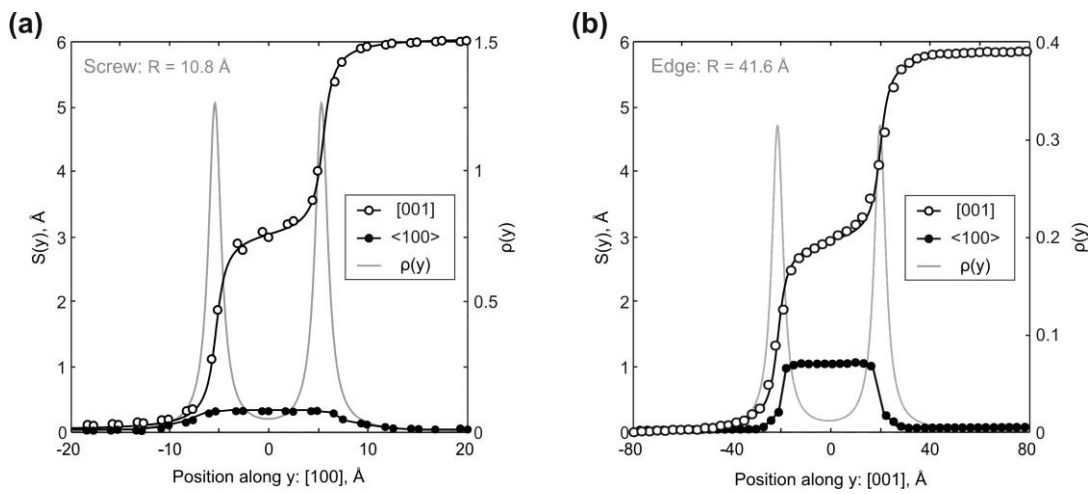


Fig. 5.3. Disregistry function $S(y)$ and the [001] Burgers vector density $\rho(y)$ of stable screw (a) and edge (b) dislocations computed for the cation sublattice.

that splitting occurs into two geometrically identical partials. The core spreading of each partial is very narrow and characterized by the half-width ζ close to 1 Å. The distance R between the partials is estimated as the distance between the two maximum of the peaks $\rho(y)$ and found to be 10.8 Å which is close to $4 \times a$ unit cell parameters. It should be noted that in addition to the [001] screw component, the dislocation core exhibits the presence of $\sim 15\%$ $\langle 100 \rangle$ edge component (Fig. 5.3a), *i.e.* the presence of small displacements in the plane of core spreading, but perpendicular to the dislocation line. On the DD-plot map (Fig. 5.2), such atomic displacements in the dislocation core can be clearly seen within the Mg-sublattice by superposing atomic layout in the dislocation core with that in a perfect crystal. Alternatively, from Figure 5.1, one can notice that, out of the dislocation core, Mg

atoms are perfectly aligned along the [100] direction with vertical bonds between silicon and apical oxygen atoms (in the perfect crystal both Mg and apical O occupy $4c$ Wyckoff positions), while within the stacking fault area, the Mg sublattice is slightly displaced towards empty spacing between the Si-O bonds due to the presence of the small $\langle 100 \rangle$ edge component.

5.1.2 Edge dislocations

Taking into account that [001] screw dislocations dissociate in (010) plane and that their dissociation in any other planes has been never observed, only [001](010) edge dislocations are considered in this work. From the atomic structure of the relaxed [001](010) edge dislocation core (Fig. 5.4), one can notice that it also splits into two symmetric partials separated by a widespread stacking fault where orientation of Si-octahedra located below and above the stacking fault (indicated with dashed red line on Fig. 5.4) resembles a mirror reflection of each other. Such a configuration can be produced by shearing the upper (or lower) part of the crystal by $\frac{1}{2}\langle 101 \rangle$ in (010). In other words, this atomic arrangement explicitly reproduces the structural geometry of the metastable stacking fault in the middle of the (010) γ -surface with $z_{010} = 0.7$ (see Fig. 3.3c).

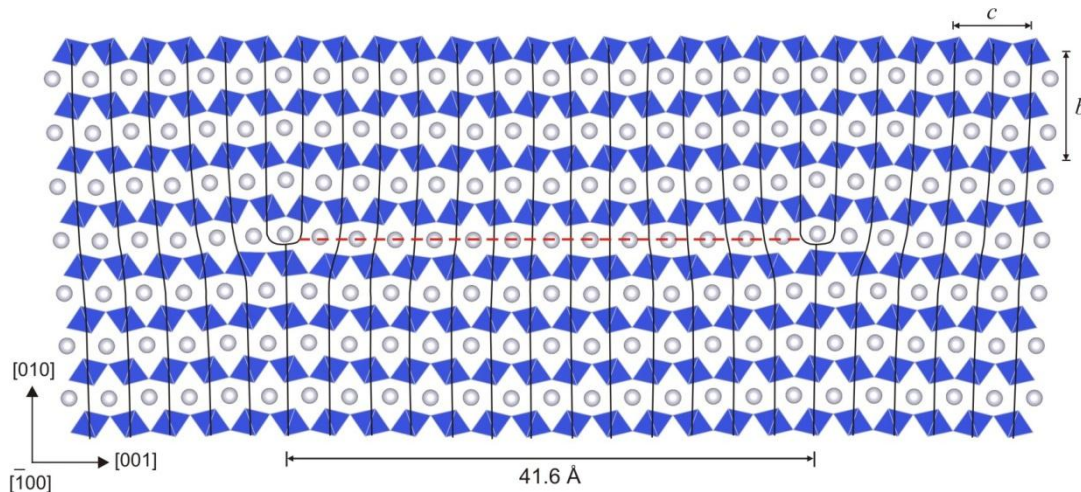


Fig. 5.4. Atomic structure of the stable [001] edge dislocation core viewed along [100] direction. SiO_6 octahedra are shown in blue; Mg atoms – with white balls. Distance R between the two partials and the unit cell parameters b and c are indicated with arrows. Location of the stacking fault is shown with dashed red line

The disregistry function $S(y)$ of the observed dislocation core (Fig. 5.4b) confirms its mixed character and indicates simultaneous presence of both $\frac{1}{2}[001]$ edge and $\frac{1}{2}\langle 100 \rangle$ screw components. The estimated distance R between the partials is 41.6 Å which [001] screw dislocation. The half-width ζ of each partial is found to be about 3 Å, which is close to $\frac{1}{2}b$.

5.2 Evolution of dislocation core characteristics with dissociation distance

In this work, we also seek for structural optimization of several metastable configurations of [001](010) dislocation cores with different separation distance between the partials. For that purpose, [001] screw dislocations are also designed by imposing separately the two $\frac{1}{2}[001]$ pure screw or mixed $\frac{1}{2}\langle 101 \rangle$ partials in such a way that the distance between them along [100] varies from 5 Å to 50 Å. In case of edge dislocation, the initial building scheme (see Chapter 2, section 2.3.1) restricts the search for metastable configurations to those encountered during the molecular static minimization steps.

In case of [001](010) edge dislocations, the metastable core configurations investigated correspond to a planar dissociation of [001] Burgers vector into two partial dislocations separated by a fault of width R varying from 30 Å to 50 Å. All configurations are characterized by the presence of an invariant $\frac{1}{2}\langle 100 \rangle$ component (Fig. 5.5a). This indicates that all these dislocation cores are associated with the same γ -energy corresponding to the $\frac{1}{2}\langle 101 \rangle(010)$ stacking fault. The observed configurations of [001] screw dislocations are less extended. The estimated separation distance R between the screw partials varies from 8.5 Å to 18 Å. In contrast to the edge dislocations with the regular stacking fault geometry (Fig. 5.5a), $\langle 100 \rangle$ component in [001] screw dislocation cores increases linearly with R and varies from 10% to 35% (Fig. 5.5b) in the range considered. This means that all detected screw dislocation cores are characterized by different γ -energies, *i.e.* associated with various stacking fault configurations.

Dealing with significantly extended dislocation cores prevents us from using fully periodic atomic arrays for estimating their energies. Thus, we verify the atomic structure of the boundary “frozen” area (see Chapter 2, the section 2.3.2) to be strictly the same for all configurations (but different for screw and edge dislocation cores) and compute potential

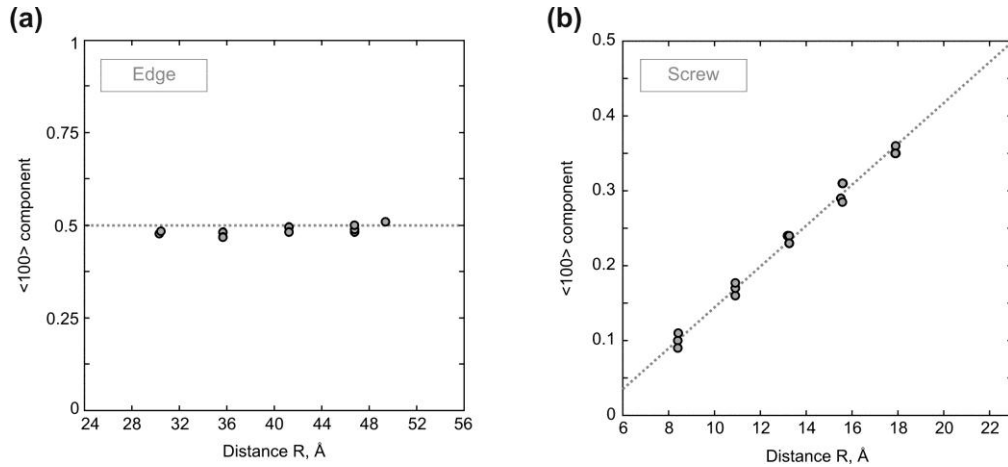


Fig. 5.5. Evolution of the $\langle 100 \rangle$ component in $[001]$ edge (a) and screw (b) dislocation cores with increasing distance R between the partial dislocation lines.

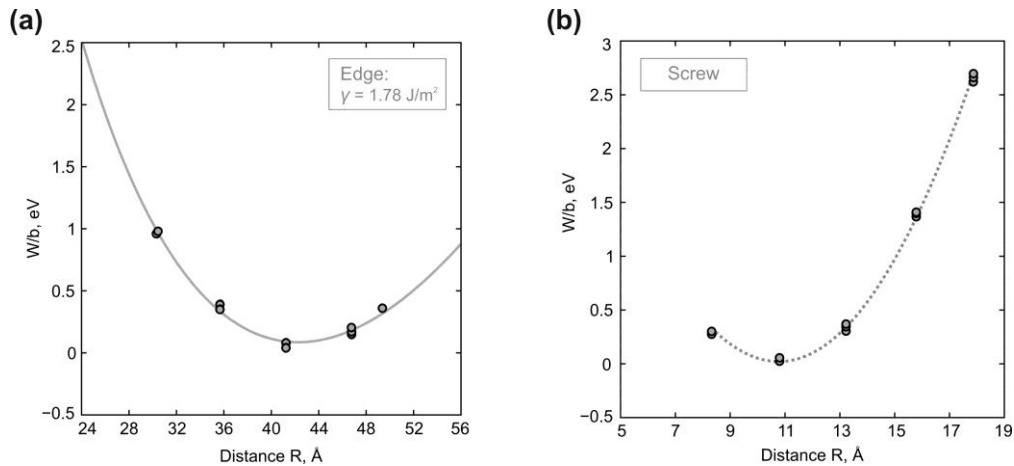


Fig. 5.6. Estimated energies of $[001]$ edge (a) and screw (b) dislocation cores (once the minimum energy is extracted) shown as a function of the dissociation distance R between the partial dislocation lines. Energies of the edge dislocation cores (a) are fitted with the elastic equilibrium equation (5.1) illustrated with the solid grey line.

energy of the atomic array not included into this region. Dimensions of the supercells were gradually increased until there is no size effect on the computed energies. In order to ensure that the chosen configuration of the boundary area has no effect on the structure of the screw dislocation cores and the associated energies, three different geometries of the “frozen” zone were tested. The displacement field in these areas corresponds to the displacement field produced by a Volterra screw dislocation, designed to be symmetric with respect to the geometric center of the core configurations whose size scales with (i)

odd number or (ii) with the even number of [100] lattice repeats, or (iii) represents the intermediate configuration of those two. For large enough simulation cells (in excess of 350 Å along the dislocation core spreading and 180 Å in the direction normal to the glide plane), the computed energies of the system are not sensitive to the chosen configuration of the “frozen” zones. The estimated energy values (once the minimum energy is extracted) for edge and screw dislocations are presented on Fig. 5.6a,b as a function of the separation distance R between the partials. The minimum energy configurations correspond to the edge and screw dislocations with $R=41.6$ Å and 10.8 Å, respectively, *i.e.* to the stable dislocation cores described above.

5.3 Stacking fault energies

In case of dissociated dislocations, stacking fault energies represent an essential parameter influencing their dissociation width. Accounting for a change in dissociation width R in various metastable configurations with respect to that in the stable dislocation core, the associated energy increase ΔW should scale with the following expression (Hirth and Lothe 1982):

$$\begin{aligned} \frac{\Delta W}{L} = & \gamma |R_{SF} - R_{SF}^{eq}| - \frac{\mu}{2\pi} (\vec{b}_1 \cdot \vec{l}_1) (\vec{b}_2 \cdot \vec{l}_2) \ln \frac{R}{R^{eq}} - \\ & - \frac{\mu}{2\pi(1-\nu)} [(\vec{b}_1 \times \vec{l}_1) \cdot (\vec{b}_2 \times \vec{l}_2)] \ln \frac{R}{R^{eq}}, \end{aligned} \quad (5.1)$$

where $\Delta W/L$ is the increase in energy per dislocation unit length with respect to the equilibrium configuration characterized by dissociation width R_{eq} ; R_{SF} is the width of a perfect stacking fault between the two partials; μ is the anisotropic shear modulus; ν is the Poisson ratio; \vec{b}_i , and \vec{l}_i are the partial Burgers vectors and the dislocation line vectors, respectively. According to eq. (5.1), the change in energy $\Delta W/L$ results from misbalance between the elastic interaction energy of partial dislocations (the last two terms) and the stacking fault ribbon energy (the first term). It should be noted, that the separation distance R defined in this work as the spacing between the two maximum peaks of the Burgers vector density $\rho(y)$ actually describes the spacing between the two partial dislocation lines.

The width of a perfect stacking fault for each dislocation core configuration can be defined as $R_{SF} = R - 2\zeta$, where ζ is a half width of each partial (Fig. 5.7).

Based on the observed geometric and energetic characteristics of dissociated edge dislocation cores associated with the $\frac{1}{2}\langle 101 \rangle (010)$ stacking fault, one can estimate the corresponding γ -energy from the elastic equilibrium equation (5.1). Fitting the dislocation core energies computed at atomic scale (Fig. 5.6a) with equation (5.1) employing the $R_{SF} = R - 2\zeta$, $\mu = 184$ GPa calculated from elastic constants and anisotropic Poisson ratio $\nu = 0.454$ determined using GULP (Gale and Rohl, 2003) provides $\gamma = 1.78$ J/m². In case of screw dislocations, all the dislocation cores with different dissociation width are characterized by different γ -energies and, therefore, the latest cannot be accurately calculated through fitting the dislocation core energies with equation (5.1).

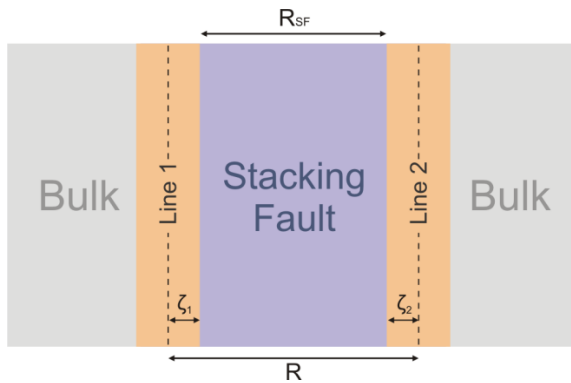


Fig. 5.7. Schematic illustration of the relation between the distance R (separating the two dislocation lines) and the width of a perfect stacking fault R_{SF} in a dissociated dislocation core.

Alternatively, relying on structural information derived from atomic-scale dislocation modeling, the related γ -energies can be computed with anisotropic elasticity using DISDI code (Douin *et al.* 1986) based on the Stroh formalism (Stroh 1958). The estimated energies for five different configurations of [001] screw dislocations with $\langle 100 \rangle$ edge component varying from 10 to 35 % and for the stable configuration of $\frac{1}{2}\langle 101 \rangle$ edge dislocation are presented on Fig. 5.8 in comparison with those from GSF calculations. The computed γ -energies for stable screw (15% of $\langle 100 \rangle$ component) and edge dislocations (50% of $\langle 100 \rangle$ component) are 2.85 J/m² and 1.86 J/m², respectively. The γ -energy of the edge dislocations is in a good agreement with 1.78 J/m² from the dislocation energy fit (Fig. 5.6a).

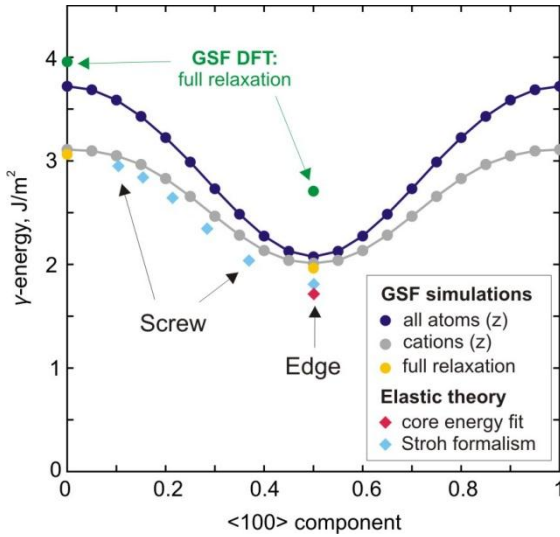


Fig.5.8. Evolution of the $\frac{1}{2}[001](010)$ stacking fault γ -energy with increasing $\langle 100 \rangle$ component estimated with the γ -surface (GSF) simulations and from elastic theory (relying on the dislocation core geometries detected in this study). All the points provided in the legend are computed based on the data acquired from the pairwise potential modeling.

Conventional GSF simulations provide higher γ -energies (blue line on Fig. 5.8) than that estimated with elastic theory, especially for the atomic configurations with low $\langle 100 \rangle$ component. In the performed GSF simulations (Chapter 3) all atoms are allowed to move perpendicular to the glide plane only (in order to avoid the perfect crystal recovery) which inevitably leads to overestimation of energies. In order to reduce this effect, we additionally perform the same kind of simulations where degrees of freedom are restricted only for cations while oxygen atoms are allowed to relax fully in all directions. This leads to a decrease in γ -surface energy associated with $\frac{1}{2}[001](010)$ stacking fault by $\sim 0.6 \text{ J/m}^2$ (Fig. 5.8), however, while $\langle 100 \rangle$ component increases (following the dashed gray line on Fig. 5.9), this effect subsists and almost vanishes for $\frac{1}{2}\langle 101 \rangle(010)$ configuration (Fig. 5.8). Allowing full relaxation for all atoms in highly symmetric configurations with $\frac{1}{2}[001]$ and $\frac{1}{2}\langle 101 \rangle$ shift provides the energies very close to that obtained while restricting only cations (Fig. 5.8). Therefore, the latest can be considered as the reference γ -energy to compare with. For the stable screw dislocation core geometry (with $2\zeta = 2 \text{ \AA}$), the difference between the γ -energies deduced from the GSF calculations and from elasticity is 5%. This discrepancy increases up to 15% for the edge dislocation core configurations (characterized by 2ζ close to 6 \AA). Thus, discrepancy between the γ -energy defined from GSF simulations and that from the elastic theory increases with increasing dislocation core extension and the width of dislocation partials, which is not taken into account by elasticity.

5.4 Dissociation process

Atomistic modeling of both [001] screw and edge dislocations show that they dissociate in (010) into two symmetric partials separated by a stacking fault. Both dislocations exhibit mixed characters and are characterized by the presence of $\langle 100 \rangle$ components. However, in case of edge dislocations, dissociation occurs into two $\frac{1}{2}\langle 101 \rangle$ partials, while for the screw dislocations, dissociation $[001] \rightarrow \frac{1}{2}[101] + \frac{1}{2}[-101]$ involves high energy configurations (Fig. 5.6b) and, therefore, it has been never observed. The dissociation path of stable screw and edge dislocation cores is presented on Fig. 5.9 on top of the corresponding (010) γ -surface energy map (see Chapter 3). Increasing $\langle 100 \rangle$ component up to $\frac{1}{2}\langle 100 \rangle$ along the $\frac{1}{2}[001](010)$ stacking fault (which corresponds to the γ -line energy profile from Fig. 5.8, also indicated with dashed gray line on Fig. 5.9) results in decrease in stacking fault energy and, consequently, to an increase of the stacking fault width between the partials. Such dependence between the stacking fault energy and dissociation distance explains the observed relation between the $\langle 100 \rangle$ component and the distance R in various metastable configurations of dissociated [001](010) screw dislocation cores (Fig. 5.5b). At the same time, dissociation of the edge dislocations appears to be large enough to incorporate the invariant $\frac{1}{2}\langle 100 \rangle$ component (Fig. 5.5a).

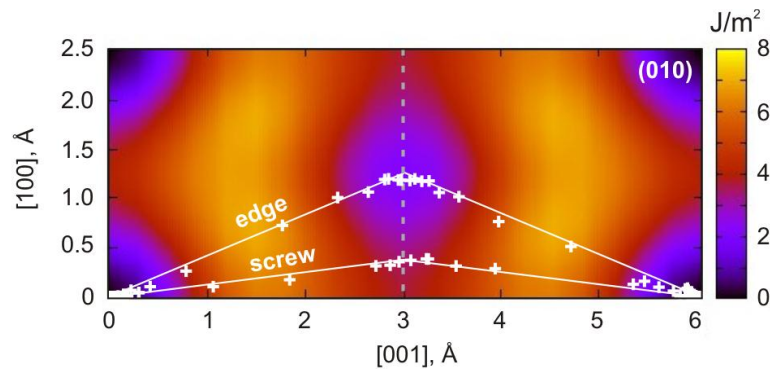


Fig.5.9. Dissociation path of the stable [001] edge and screw dislocations in (010) plane shown in projection to the corresponding γ -surface map.

According to the elastic theory, being characterized with the same stacking-fault energy γ , the size of screw and edge dislocations should scale with a ratio of $1/(1-\nu)$. Thus, [001] screw dislocations with $\frac{1}{2}\langle 100 \rangle$ edge component would be characterized by R close

to 23 Å which agrees well with the linear trend (Fig. 5.5b) describing evolution of $\langle 100 \rangle$ component in [001] screw dislocations with increasing distance R between the partials.

Previous *ab initio* studies of GSF in MgSiO₃ post-perovskite (Carrez *et al.* 2007; Metsue and Tsuchiya 2013) did not consider the presence of $\frac{1}{2}\langle 101 \rangle(010)$ stacking fault. In order to ensure stability of such a stacking fault configuration, we additionally performed γ -surface simulations with DFT where full relaxation is allowed to the highly symmetric $\frac{1}{2}\langle 101 \rangle(010)$ and $\frac{1}{2}[001](010)$ configurations (green points on Fig. 5.8), *i.e.* calculations, similar to that described in the previous section for the pairwise potential (yellow points on Fig. 5.8). As expected, γ -energies from the *ab initio* calculations are higher (by ~25%) than those computed with the pairwise potential. However, both simulation techniques consistently indicate that presence of $\frac{1}{2}\langle 100 \rangle$ component results in 35% reduction of the stacking fault energy. This implies that qualitative prediction from the pairwise potential modeling on the mixed character of [001] dislocations is rather plausible.

5.5 Lattice friction

In this work, the critical stress opposed to the [001](010) dislocation glide is computed at atomic scale while applying a simple shear in order to increase the stress in the glide plane as predicted by the Peach-Koehler equation (2.15). Under applied stress, both [001](010) screw and edge dislocation exhibit similar behavior, *i.e.* the two partials glide together while keeping the stacking fault width constant. Dislocation glide starts at 3 GPa and 2 GPa and proceeds by successive steps of [100] and $\frac{1}{2}[001]$ lattice repeats for screw and edge dislocations, respectively. Being characterized by a larger Peierls stress, the mobility of screw dislocations is expected to govern plastic strain for this slip system. However, it's worth noticing that, in contrast to [100] dislocations in post-perovskite (Chapter 4), where the Peierls stress σ_p is found to be one order of magnitude lower for edge dislocations than for screw, σ_p of edge dislocations is only 33% lower in case of the [001](010) system.

Relying on the observed characteristics of dislocation cores and their response to applied shear, one can estimate the corresponding Peierls energy barrier. Dislocation

motion by successive steps of [100] and $\frac{1}{2}$ [001] lattice repeats suggests that the periodicity of the Peierls potential, denoted hereafter as a' , is equal to $a = 2.5 \text{ \AA}$ and $c/2 = 3 \text{ \AA}$ unit cell parameters for screw and edge dislocations, respectively. Both partials climb the Peierls barrier together. Assuming a simple sinusoidal shape of the potential, the maximum energy barrier for each partial can be defined as (Koizumi *et al.* 1993): $V_p^{max} = \frac{1}{\pi} a' b_p \sigma_p$, where b_p is the partial Burgers vector length. The estimated V_p^{max} values are 46 meV/Å for screw dislocations and 39 meV/Å for edge dislocations.

5.6 Kink-pair formation enthalpy

Atomistic modeling of [001](010) dislocations gives access to dislocation core geometries, associated γ -energies and to the opposed lattice friction at 0 K. At finite temperature, dislocation motion involves nucleation and propagation of kink-pairs. For a dissociated dislocation, the enthalpy ΔH related to a kink-pair nucleation process involves four terms: (i) ΔE_{el} - the increase in elastic energy caused by the increase in length of the dislocation line; (ii) ΔP - the change in the Peierls energy of the line portion which leaves the Peierls valley; (iii) ΔW_{sf} - the energy cost associated with the change in the stacking fault energy γ due to increase/decrease in the equilibrium distance R between the partials; (iv) W_σ - the work of the applied stress.

For [001] dislocations, fully atomistic modeling of kink-pairs will be extremely challenging to perform due to the very complex structure of dissociated dislocation cores, which will also require unreasonably large atomic arrays. Therefore, in this study, kink pair formation enthalpy for [001](010) dislocations is estimated with the elastic interaction model (Koizumi *et al.* 1993) employing the derived characteristics of straight screw dislocations, controlling plastic deformation for this system.

As it has been shown by Koizumi *et al.* (1993), for low lattice friction materials with a ratio σ_p/μ close to 10^{-2} , the ΔP term contributes only about 1% to the total kink-pair formation enthalpy ΔH . For the [001] screw dislocations, this ratio is equal $1.6 \cdot 10^{-2}$, which allows neglecting the positive contribution of ΔP to the Peierls potential V_p .

The energy term ΔW_{sf} is relevant only in case of the so-called uncorrelated nucleation when kink-pairs nucleate independently on leading and trailing partials which locally changes the stacking fault width and, consequently, its energy. Involving additional energy cost, this process is likely to occur only above a critical stress σ^{crit} , while below this value only correlated nucleation (both kink-pairs nucleate simultaneously such as their centers coincide) takes place without changing the stacking fault width along the partials. The critical stress can be estimated as (Möller 1978): $\sigma^{crit} = \frac{\pi\gamma^2 a'}{\beta\mu b_p^3}$, where β is a function of the angle θ_i between the partial Burgers vector \vec{b}_i , and the dislocation line \vec{l}_i defined as $\beta = \cos\theta_1 \cos\theta_2 + \sin\theta_1 \sin\theta_2 / (1-\nu)$, where ν is the Poisson ratio. Employing previously defined $\nu=0.454$, $\gamma=2.85$ J/m² and $\theta=\sim 7^\circ$ for the [001] screw dislocations, the critical stress σ^{crit} is found to be close to 1.3 GPa which is well above the stresses expected in the lower mantle. Therefore, in case of the [001](010) screw dislocations only correlated kink-pair nucleation is expected to occur in mantle conditions and, therefore, the ΔW_{sf} term can be disregarded.

Based on all these assumptions, with no stress applied, the formation enthalpy $H_{2k}(\sigma=0)$ of a rectangular kink-pair with large width w (such as $w \gg h$, where $h=a'$ is the kink height) on each partial can be estimated as (Möller 1978; Hirth and Lothe 1982):

$$H_{2k} = \frac{\mu a'}{2\pi} \left[b_s^2 \left(\frac{1}{1-\nu} \ln \frac{a'}{e\rho} - 1 \right) + b_e^2 \left(\ln \frac{a'}{e\rho} - \frac{1}{1-\nu} \right) \right], \quad (5.2)$$

where μ is the anisotropic shear modulus; a' is the periodicity of the Peierls Potential; b_s and b_e are the screw and edge components of b_p , respectively; ν is the Poisson ratio; e is the Euler's number; and ρ is the cut-off distance commonly taken as 5-10% of the Burgers vector. However, the H_{2k} value defined using eq. (5.2) is very sensitive to the choice of ρ (Koizumi *et al.* 1993). Thus, varying the cut-off ρ from 5 to 10 % of the partial Burgers vector b_p results in deviation of the H_{2k} values from 9.7 to 4.2 eV. It should be noted that independently of ρ , contribution of the edge component into H_{2k} does not exceed 0.2% due to the very small $b_e = b_p \sin \theta$, hence, the second term in eq. (5.2) is neglected. Based on the model of Koizumi *et al.* (1994) and results of the recent atomic-scale simulations in conjunction with the elastic interaction model (Kraych *et al.* 2016a), the kink-pair enthalpy H_{2k} at zero stress can be approximated as $\mu b_p^3 \sqrt{\sigma_p / \mu}$, which provides $H_{2k} = 4.15$ eV

consistent with $\rho = 0.1b_p$ in eq. (5.2). Relying on this value, the estimated $V_p^{max} = 46 \text{ meV}/\text{\AA}$ is indeed close to 1% of H_{2k} in agreement with (Koizumi *et al.* 1993). As it was shown above, motion of a dissociated [001] screw dislocations is expected to occur through correlated kink-pair nucleation, therefore, the energetic cost associated with the kink-pair formation on both partials can be set as $H_{4k} = 2H_{2k} = 8.3 \text{ eV}$. As expected from the dislocation core structure and the Peierls stress, this value is notably higher than $H_{2k} = 1.71 \text{ eV}$ for [100](010) dislocations in MgSiO₃ post-perovskite (see Chapter 4), however it is still more than twice lower than the H_{2k} values (*c.a.* 20 eV) calculated for MgSiO₃ bridgmanite (Kraych *et al.* 2016a,b).

5.7 Summary

In this chapter, we characterized atomic structure of dissociated [001] dislocation cores in MgSiO₃ post-perovskite relying on the chosen pairwise potential model. Both [001] screw and edge dislocations dissociate in (010) plane into two symmetric partials separated by a stacking fault of $\sim 11 \text{ \AA}$ and $\sim 42 \text{ \AA}$, respectively. Detailed analysis of the dislocation cores reveals their mixed character and the presence of a $\langle 100 \rangle$ component. In case of edge dislocations, dissociation occurs into two $\frac{1}{2}\langle 101 \rangle$ partials, while the $\langle 100 \rangle$ component for the screw dislocation core is only 15%. Under applied stress, both [001](010) screw and edge dislocations behave similarly. Above the Peierls stress, the two partials glide together while keeping their stacking fault widths constant. Lattice friction opposed to the [001](010) screw dislocation glide is found to be 3 GPa, while that of edge dislocations is 2 GPa. Consequently, plastic deformation within this slip system is expected to be governed by the screw dislocations. The computed characteristics of the straight [001] screw dislocations (stacking fault energy, Peierls stress, and periodicity of the Peierls potential), were used to estimate the kink-pair formation enthalpy $\Delta H_{4k} = 8.3 \text{ eV}$ at zero applied stress based on the elastic interaction model by Koizumi *et al.* (1993).

CHAPTER 6

Dislocations and Deformation Twinning with $\frac{1}{2}[110]$ Burgers Vector

Results of the atomic scale modeling performed for defects governing plastic deformation of MgSiO_3 post-perovskite along $\langle 110 \rangle$ direction are summarized in this chapter. Screw and edge $\frac{1}{2}[110]$ dislocations and their behavior under applied stress at 0 K are investigated based on the chosen pairwise potential model. These simulations are followed by *ab initio* and semi empirical modeling of $\frac{1}{2}\langle 110 \rangle\{110\}$ deformation twinning, commonly observed with TEM for CaIrO_3 post-perovskite low-pressure analogue. Atomistic modeling of twinning gives an access to the energy of twin boundary through generalized planar fault energy (GPFE), also called twinning energy landscape. Computed GPFE is further integrated into a mesoscale description of the total energy E_{tot} associated with $\frac{1}{2}\langle 110 \rangle\{110\}$ twinning in MgSiO_3 post-perovskite, which allows determining the equilibrium twin configuration and the critical twin nucleation stress.

6.1 Structure of $\frac{1}{2}[110]$ dislocation cores

6.1.1 Screw dislocations

Dislocation cores with $b = \frac{1}{2}[110]$ are investigated in the so-called “slab” simulation cell geometry (Fig. 2.11b in Chapter 2) relying on the pairwise potential. Structural relaxation systematically leads to dislocation cores spreading in $(1\bar{1}0)$. Computing disregistry $S(y)$ of $\frac{1}{2}[110](1\bar{1}0)$ screw dislocation cores shows an asymmetric dissociation in $(1\bar{1}0)$ plane into $\frac{1}{3}[110]$ and $\frac{1}{6}[110]$ partials. However the equilibrium distance between the partials is not well defined. Indeed, increasing the size of the simulation cell along $[001]$, corresponding to the direction of the dislocation core spreading, always results in an increase of the stacking fault width while keeping geometric characteristics of the two partials invariant. Thus, a $1b \times 300\text{\AA} \times 160\text{\AA}$ simulation cell of slab geometry (see Chapter 2) contains a dislocation core of $\sim 18\text{\AA}$, while $1b \times 450\text{\AA} \times 160\text{\AA}$ – a core of $\sim 30\text{\AA}$. Such a behavior indicates very low γ energy associated with the stacking fault between the two partials.

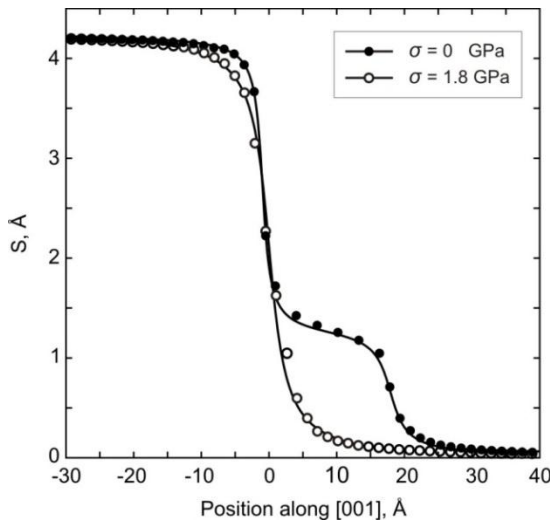


Fig. 6.1. Disregistry functions $S(y)$ of $\frac{1}{2}[110](1\bar{1}0)$ screw dislocation cores (presented on Fig. 6.2) computed for the cation sublattice in $1b \times 300\text{\AA} \times 160\text{\AA}$ simulation cell with no stress applied ($\sigma = 0$) and under applied stress of 1.8 GPa, when the two dislocation partials collapse into a compact dislocation core.

Figure 6.1 illustrates the disregistry function $S(y)$ computed for the dislocation core (with no applied stress), denoted as $\sigma = 0$ GPa, with a stacking fault of 18.2\AA , close to $3 \times c$ lattice parameters (defined as the distance R between the two maximum peaks of $\rho(y)$, further provided on Fig. 6.4). The estimated half-widths ζ of the partials are 0.9\AA and 1.8\AA for $\frac{1}{3}[110]$ and $\frac{1}{6}[110]$, respectively. In other words, the Burgers vector of the second partial is twice shorter and its core is twice wider than the first one.

The corresponding DD-plot map of the $\sim 18 \text{ \AA}$ $\frac{1}{2}[110]$ screw dislocation is provided on Fig. 6.2a. To better understand the atomic structure of the dislocation core, the latter is cut perpendicular to its spreading into several (001) atomic layers of $\frac{1}{2}[001]$ width as it is shown on Fig. 6.2a. The extracted (010) atomic layers (which experience the largest distortions) can be classified into 3 distinct types illustrated on Fig. 6.2c.

The first one, denoted hereafter as *bn*, incorporates local bending of SiO and MgO layers without changing the general character of polyhedral interconnections along $[100]$ by the edges. The second, indicated as *pv*, – clearly corresponds to the stacking fault configuration containing perovskite-like octahedral interconnections by corners (shown

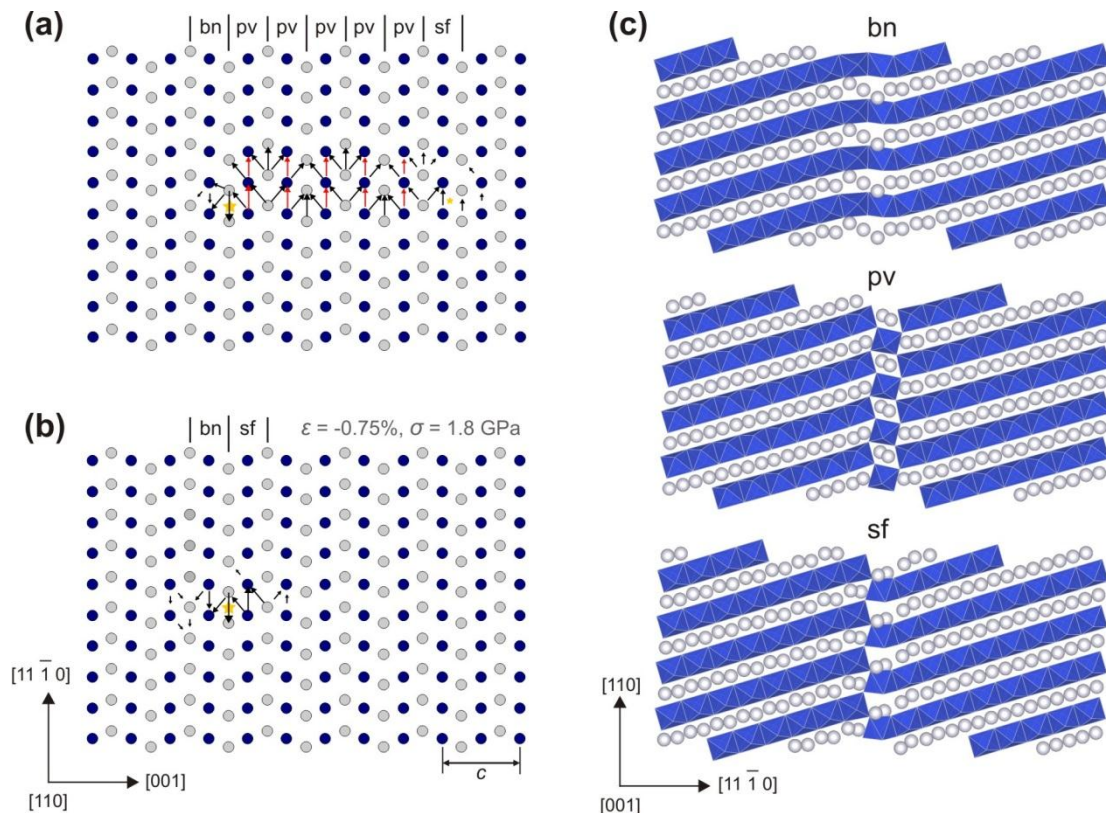


Fig. 6.2. DD-plot map of $\frac{1}{2}[110]$ screw dislocation core with $R=18.2 \text{ \AA}$ (a) with no stress applied and (b) under an applied stress $\sigma = 1.8 \text{ GPa}$. The anion sublattice is left out. Si atoms are shown with blue balls; Mg atoms—with gray balls. The arrows between atoms correspond to the $\frac{1}{2}[110]$ component of the relative displacement of the neighboring atoms produced by the dislocation. Red arrows indicate interconnection by corners of Si-octahedra. Location of the $\frac{1}{3}[110]$ and $\frac{1}{6}[110]$ partials are indicated with big and small stars, respectively. (c) Atomic structure of the three distinct (001) atomic layers, denoted as “bn”, “pv” and “sf”, characterized by maximum distortion inside of the $\frac{1}{2}[110]$ screw dislocation core. Location of this layers in the core structure is specified in (a) and (b).

with double red arrows on Fig.6.2a). The third type of the distorted (010) atomic layers, marked as *sf*, reproduces the atomic structure which can be produced by applying $\frac{1}{3}[110]$ rigid shear in $(1\bar{1}0)$ plane. Superposing the structural information, extracted from the disregistry function $S(y)$ and distorted (010) layers, one can find, that the $\frac{1}{3}[110]$ partial is located in the *bn* layer; the $\frac{1}{6}[110]$ partial – within the *sf* layer; and the 5 *pv* layers between them correspond to the stacking fault separating the partials.

6.1.2 Edge dislocations

Similarly to the observed $\frac{1}{2}[110]$ screw dislocation core splitting, $\frac{1}{2}[110](1\bar{1}0)$ edge dislocations dissociate into $\frac{1}{3}[110]$ and $\frac{1}{6}[110]$ partials (Fig.6.3) separated by a widespread stacking fault where Si-octahedra are interconnected by corners creating a 1-octahedron thin lamella of perovskite phase in post-perovskite matrix (Fig. 6.4). From the disregistry function $S(y)$, the half-width ζ of the partials are 2.1 Å and 3.2 Å for $\frac{1}{3}[110]$ and $\frac{1}{6}[110]$, respectively. Even using simulation cells of size up to 450 Å along the dislocation core spreading direction (*i.e.* along [110] for edge dislocations), one cannot find size independent dislocation core configurations. By analogy with $\frac{1}{2}[110]$ screw dislocations, the dissociation width of edge dislocations increases with increasing size of designed atomic arrays. For the $6\text{ Å} \times 300\text{ Å} \times 160\text{ Å}$ simulation cell size, the distance R between the two partials is found to be 57.2 Å, which is three times larger than that for $\frac{1}{2}[110]$ screw dislocations observed in a simulation cell of the same dimensions.

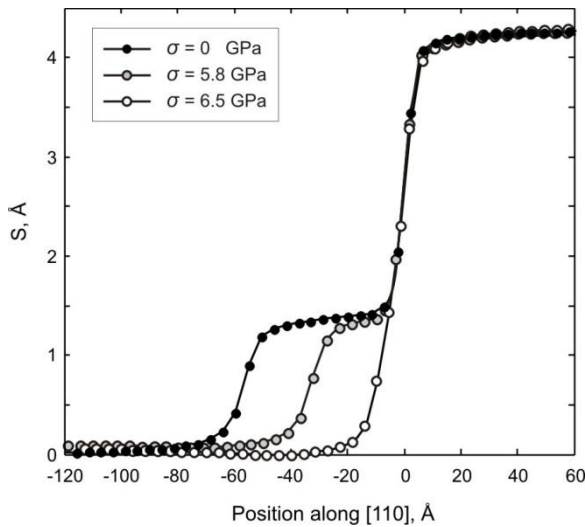


Fig. 6.3. Disregistry functions $S(y)$ of $\frac{1}{2}[110](1\bar{1}0)$ edge dislocation cores (illustrated on Fig.6.4) computed for the cation sublattice in $6\text{ Å} \times 300\text{ Å} \times 160\text{ Å}$ simulation cell.

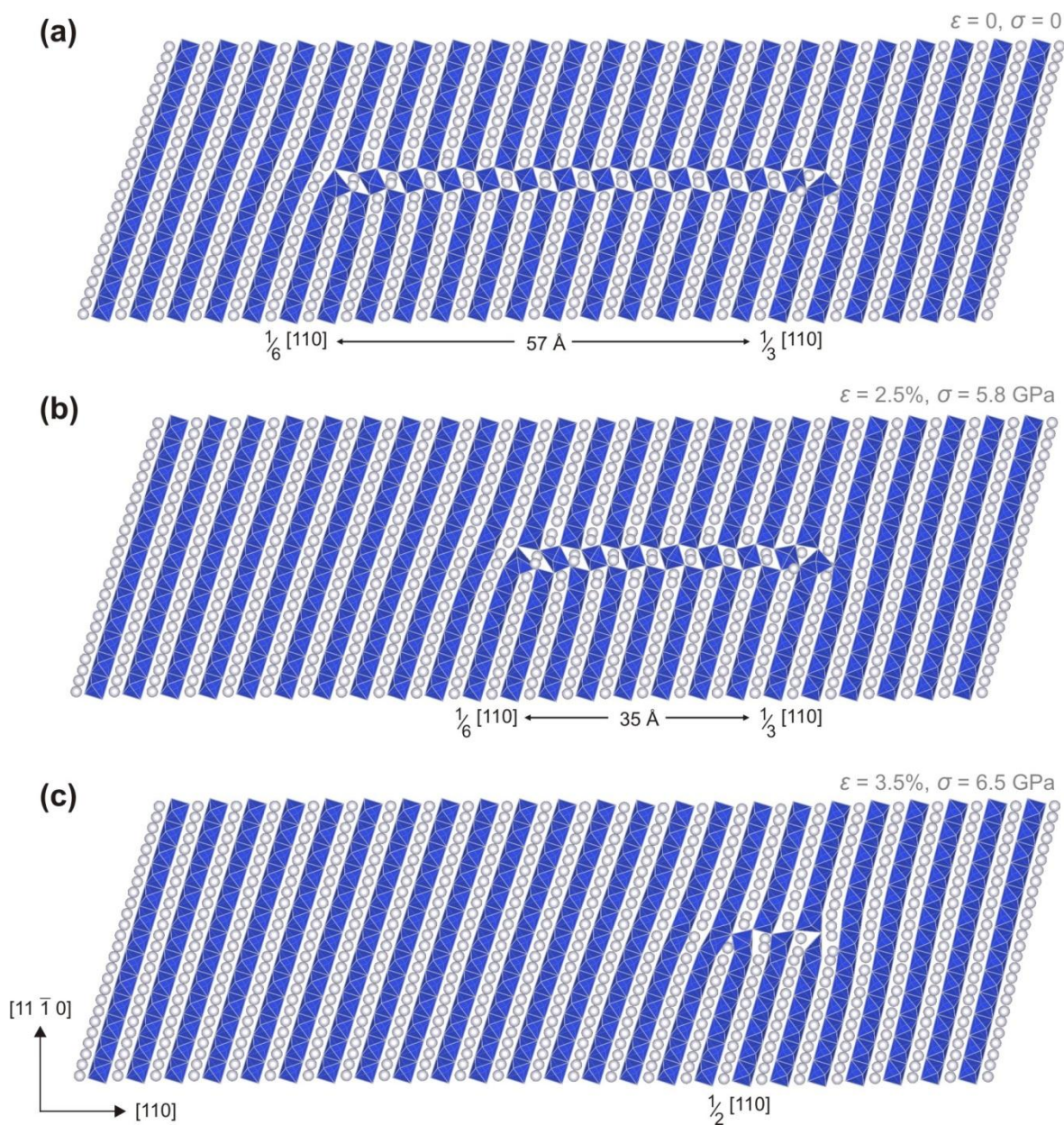


Fig. 6.4. Atomic structure of the $\frac{1}{2}[110](\bar{1}\bar{1}0)$ edge dislocation core observed in $6\text{\AA} \times 300\text{\AA} \times 160\text{\AA}$ simulation cell (a) and its evolution with applied stress (b, c). Mg atoms are shown with grey balls; Si-octahedra –in blue.

6.2 Evolution of $\frac{1}{2}\langle 110 \rangle\{110\}$ dislocation cores under applied stress

The behavior of dissociated $\frac{1}{2}[110](1\bar{1}0)$ screw and edge dislocations under applied stress is studied by applying a simple shear, increasing the shear stress in the glide plane (see Chapter 2, section 2.3.3). Under applied stress, the two partials exhibit significantly different behavior. Moreover, this behavior changes while applying a shear in opposite directions, addressed hereafter through “+” and “-” signs of the shear strain ϵ .

Dislocation glide of $\frac{1}{2}[110]$ screw dislocation along $[001]$ direction aligned with y in the $(1\bar{1}0)$ plane normal to z is triggered by applying ϵ_{xz} strain component. Monitoring disregistry function $S(y)$ of the dislocation core during this process allows detecting the effect of shear stress on the core structure. The evolution of the $\sim 18 \text{ \AA}$ screw dislocation core (Fig. 6.2a) under an applied stress is illustrated in Fig.6.5 through evolution of the Burgers vector density $\rho(y)$ computed as the derivative of the disregistry function $S(y)$.

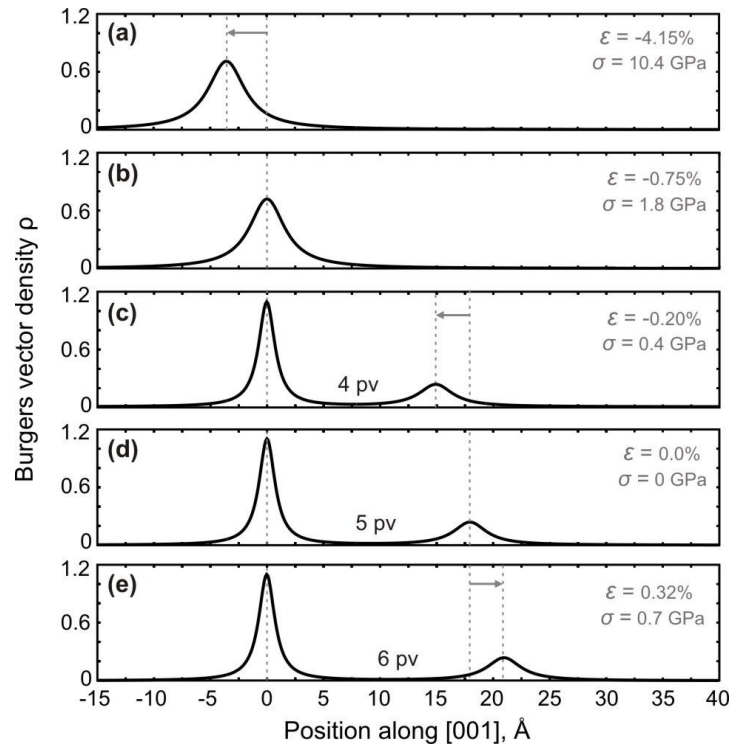


Fig. 6.5. Evolution of the Burgers vector density of $\frac{1}{2}[110](1\bar{1}0)$ screw dislocations under applied stress. On the plots with two $\rho(y)$ peaks, the smaller peak corresponds to the location of $1/6[110]$ partial and the bigger one –to the $1/3[110]$ partial; N pv between them indicates the number of the pv-type layers (Fig. 6.2c) in the stacking fault.

Under positive shear, the leading $\frac{1}{6}[110]$ partial starts moving apart from the $\frac{1}{3}[110]$ partial at $\sigma=0.7$ GPa (Fig. 6.5e). Its further propagation through the crystal structure (by successive steps of $\frac{1}{2}[001]$ lattice repeat) results in expansion of the pv layers in the stacking fault along $[001]$. During this process, motion of $\frac{1}{3}[110]$ partial has never been observed up to stresses of ~ 10 GPa. Applying shear in the opposite direction forces the leading partial to move towards the trailing one and gradually decreases the width of the the pv -stacking fault between them. When the stress reaches 1.8 GPa (corresponding to $\varepsilon_{xz}=-0.75$), the two partials collapse and form a compact $\frac{1}{2}[110]$ dislocation core with the half-width $\zeta=2$ Å (Fig. 6.1, Fig. 6.2b, Fig. 6.5b) which remains immobile until the stress reaches 10.4 GPa (Fig. 6.5a). Screw dislocations with negative Burgers vector exhibit the opposite behavior with respect to positive and negative applied strain, *i.e.* the pv -stacking fault increases with negative strain and decreases with positive.

To initiate motion of the ~ 57 Å edge dislocations (Fig. 6.4a) with $\frac{1}{2}[110]$ Burgers vector aligned with y axis in the $(1\bar{1}0)$ plane normal to z , ε_{yz} strain component is gradually increased. Under shear stress, $\frac{1}{2}[110](1\bar{1}0)$ edge dislocations behave similarly with screw dislocations, however, uncommonly for edge dislocations, critical stress values required for the onset of dislocation motion are higher for edge dislocations than that for screw dislocations. Thus, the leading $\frac{1}{6}[110]$ partial starts moving apart from the $\frac{1}{3}[110]$ trailing partial when the stress reaches 2.8 GPa. Increase or decrease of the stacking fault by one pv -type octahedra occurs by displacement of the leading dislocation line partial by 4.25 Å, *i.e.* by $\frac{1}{2}[110]$ lattice repeat. When the two partials collapse into a compact $\frac{1}{2}[110](1\bar{1}0)$ dislocation core with the half-width $\zeta=4.1$ Å (Fig. 6.3; Fig. 6.4c) at 6.5 GPa, pv -lamella in the dislocation core disappears. This core configuration remains immobile until the stress reaches ~ 19 GPa when it starts moving as entire compact core.

The onset of motion (in both directions) of the mobile $\frac{1}{6}[110]$ partial is found to be insensitive to the initial stacking fault width of dissociated $\frac{1}{2}[110]$ screw and edge dislocations. However, appearance of the compact dislocation core, resulting from the gradual closure of the perovskite stacking fault, clearly depends on the original width of the dislocation core. Thus, for the ~ 30 Å screw dissociated core (observed in $1b \times 450$ Å \times 160 Å simulation cell), the compact core configuration appears when the stress reaches 2.5 GPa. The critical stress values needed to initiate the motion of compact

$\frac{1}{2}\langle 110 \rangle \{110\}$ screw and edge dislocations do not depend on the initial width of the stacking fault. Dislocations with positive and negative Burgers vectors exhibit inverse behavior when positive or negative shear is applied.

6.3 Stacking fault structure and γ -energy

For dissociated $\frac{1}{2}[110](1\bar{1}0)$ screw and edge dislocations, the stacking fault between $\frac{1}{3}[110]$ and $\frac{1}{6}[110]$ partials represents one-octahedron thin lamella of perovskite structure. Keeping in mind previous works by Oganov *et al.* (2005) and Zahn (2011), which indicate the close relation between the $\frac{1}{2}\langle 110 \rangle \{110\}$ slip system in post-perovskite with the perovskite structure, its appearance does not seem to be surprising. However, taking into account the fact that the pairwise potential model employed in this study was initially derived for MgSiO_3 perovskite phase, we additionally verify that appearance of the perovskite lamella is not an artifact of the chosen potential parameterization. Being restricted to few hundred of atoms for DFT simulations, it is impossible to directly reproduce full atomistic modeling of $\frac{1}{2}\langle 110 \rangle$ dislocations in post-perovskite, which requires more than 40,000 atoms. Alternatively, to find the energy of the stacking fault, atomic configurations employed for $\frac{1}{2}[110](1\bar{1}0)$ γ -line calculations (see Chapter 3, Fig. 3.2d, Fig. 3.4g) are relaxed with the pairwise potential and DFT frameworks while allowing full relaxation to all the atoms in the system. For the atomic configuration, fully relaxed after applying a rigid shear of $\frac{1}{6}[110]$ in $(1\bar{1}0)$ to the upper part of the supercell, both simulation techniques demonstrate spontaneous appearance of the perovskite lamella characterized by very low excess energy with respect to the post-perovskite perfect crystal. However, the energy of the stacking fault computed with the interatomic potential is found to be almost seven times lower than that from DFT calculations (0.10 J/m^2 vs 0.69 J/m^2), indicating that in this case the pairwise potential tends to significantly overestimate the dislocation core spreading.

Although the exact dissociation width was not defined from the full atomistic modeling of $\frac{1}{2}[110]$ dislocations with the pairwise potential, one can compute the equilibrium dissociation width R_{SF} based on the Stroh formalism (Stroh 1958) using DISDI code (Douin *et al.* 1986), using the procedure similar to that, employed for dissociated

$[001](010)$ dislocations (see Chapter 5). Relying on the computed energies γ_{isf} of the $\frac{1}{6}[110](1\bar{1}0)$ intrinsic stacking fault of 0.69 J/m^2 and 0.10 J/m^2 for DFT and the pairwise potential, the corresponding stacking fault widths are 29.5 \AA and 160.7 \AA for screw dislocations, and 42.5 \AA and 209.4 \AA for edge dislocations, respectively. Thus, drastically underestimated stacking fault energy and 20% underestimated anisotropic shear modulus μ provided by the pairwise potential results in five times overestimated dissociation widths of $\frac{1}{2}[110](1\bar{1}0)$ dislocations with respect to those from the DFT modeling. Taking into account the large dissociation widths estimated using the γ -energy computed with the pairwise potential, it's not surprising that equilibrium dissociation width was not determined from the performed atomistic modeling of $\frac{1}{2}[110](1\bar{1}0)$ dislocations, where dimensions of the simulation cells did not exceed 450 \AA .

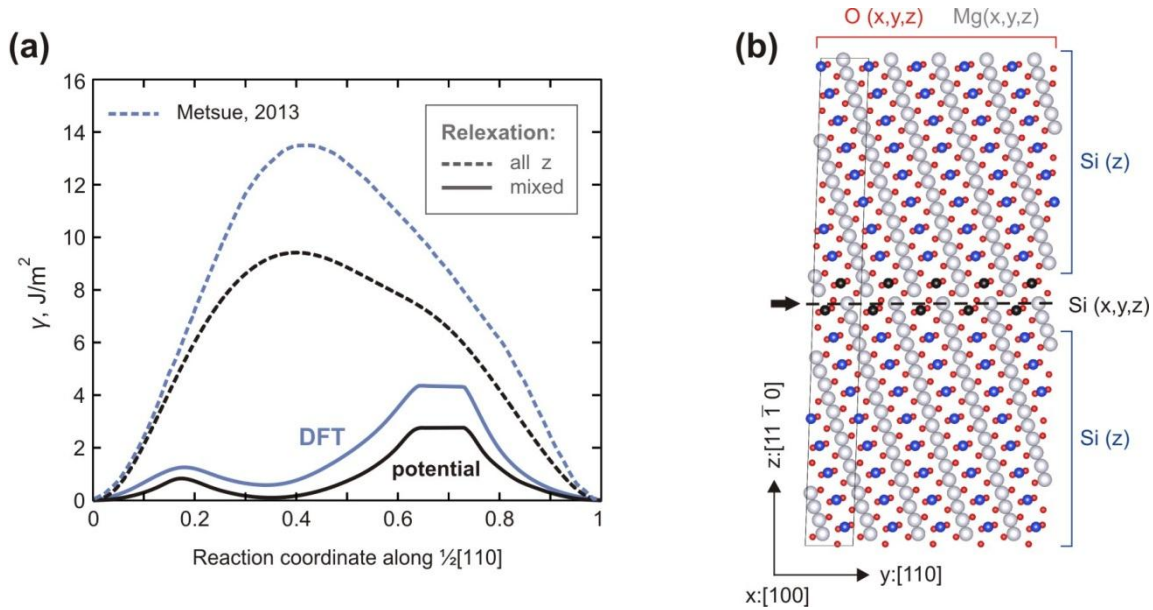


Fig. 6.6. (a) $\frac{1}{2}[110](1\bar{1}0)$ γ -line computed using (b) mixed scheme of atomic relaxation for DFT and pairwise potential simulations in comparison with previous conventional GSF simulations described in Chapter 3.

Conventional GSF simulations (described in Chapter 3), where all the atoms in the simulation cell are only allowed to relax along the direction normal to the shear plane, do not allow appearance of the p_v -lamella. Therefore, from the performed γ -surface calculations, dissociation of $\frac{1}{2}\langle 110 \rangle$ dislocations in $\{110\}$ plane was not expected. To better understand the actual shape of the corresponding $\frac{1}{2}\langle 110 \rangle \{110\}$ γ -line, additional γ -

surface simulations where degrees of freedom along $\{110\}$ shear plane are restricted only for Si atoms out of the stacking fault band. In order to allow additional shuffling of atoms close to the shear plane, necessary for appearance of the pv -lamella, one atomic Si-layer above and one layer below the shear plane are allowed to relax fully (Fig.6.6b). The resulting pairwise potential and DFT excess energy curves are provided on (Fig.6.6a) in comparison with the conventional GSF calculations. Indeed, allowing additional atomic shuffling results not only in general decrease of the γ -energy, but also in drastic change of its shape due to appearance of the apparent local energy minimum at $\frac{1}{6}[110]$ shear, indicating asymmetric dissociation of $\frac{1}{2}[110]$ dislocations, consistent with the dislocation core geometries described above. Such a scheme of mixed atomic relaxation (Fig.6.6b) provides 3% overestimated γ -energy of the $\frac{1}{6}[110](1\bar{1}0)$ stacking fault with respect to that computed while allowing full relaxation to all the atoms in the simulation cell.

6.4 Modeling $\frac{1}{2}\langle 110 \rangle \{110\}$ deformation twinning

Dislocation glide and deformation twinning often represent complementary mechanisms contributing to plastic deformation of a material. For both processes, nucleation of a leading partial occurs first. If a trailing partial can further nucleate and glide, deformation occurs through dislocation motion within the glide plane. Alternatively, if nucleation of a leading partial is followed by further successive development of similar partials in parallel adjustment planes, (micro) twinning takes place. Several TEM experimental studies of CaIrO_3 post-perovskite low pressure analogue (Miyajima *et al.* 2010; Niwa *et al.* 2012) indicate presence of $\{110\}$ twin domains in deformed CaIrO_3 samples. In this study, we also examine the efficiency of $\frac{1}{2}\langle 110 \rangle \{110\}$ deformation twinning in silicate post-perovskite at 120 GPa. Atomistic modeling of $\frac{1}{2}\langle 110 \rangle \{110\}$ dislocations indicates the importance of highly mobile $\frac{1}{6}[110]$ partials. Based on these results, we further consider $\frac{1}{6}[110]$ as a twinning dislocation. At atomic scale, deformation twinning is investigated through computing generalized planar fault energy (GPFE) landscapes (see section 2.2.2 in Chapter 2).

6.4.1 Generalized planar fault energy

The twinning energy landscape, also called generalized planar fault energy (GPFE), is computed in this work relying both on DFT and pairwise potential simulation techniques as the energy cost per unit area required to form N -layer twin by shearing N consecutive atomic layers along $[110]$ direction in $(1\bar{1}0)$ plane (Fig. 6.7). This process of lattice shearing represents successive nucleation of N stacking faults, in such a way that each of them is characterized by maximum shear displacement b_p (see Chapter 2, section 2.2.2), corresponding to the twinning Burgers vector $\frac{1}{6}[110]$. For each sequential shear displacement of the magnitude b_p (resulting in energy minimum configurations on GPFE landscape), full atomic relaxation is allowed, including directions parallel and normal to the shear plane, in order to correctly reproduce the faulted structure and the associated energy cost. All intermediate faulted configurations are relaxed using the mixed scheme described in the previous section and presented on Fig. 6.6b.

The first shear displacement by $b_p = \frac{1}{6}[110]$ in $(1\bar{1}0)$ plane creates the intrinsic stacking fault (*isf*), representing one-octahedra thick pv -lamella (Fig. 6.8), similar to that observed in $\frac{1}{2}[110](1\bar{1}0)$ dislocation cores (Fig. 6.4; Fig. 6.2). The associated energy

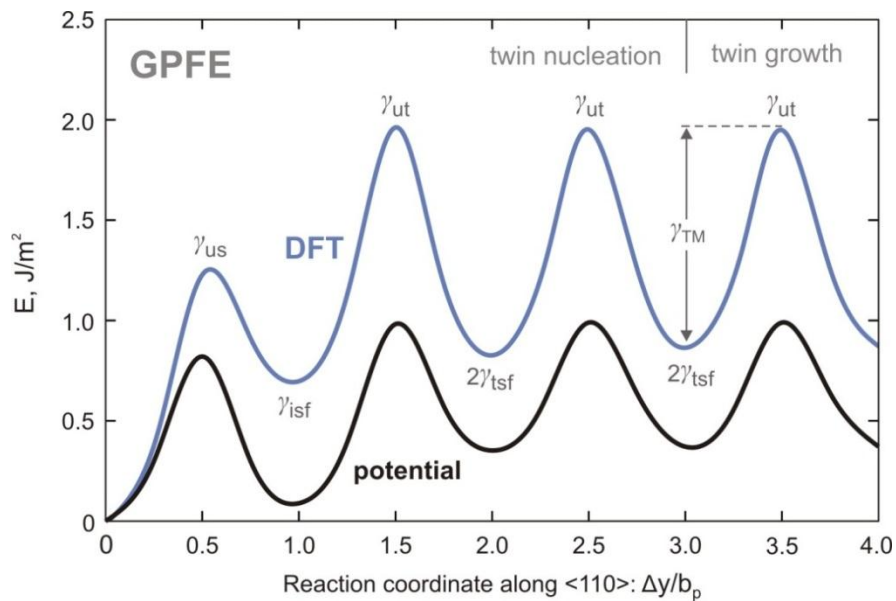


Fig. 6.7. GPFE landscape of $\frac{1}{2}\langle 110 \rangle \{110\}$ 3-layer twin with $b_p = \frac{1}{6}\langle 110 \rangle$ computed from the first principles and with the pairwise potential.

Table 6.1

Essential characteristics of $\frac{1}{2}\langle 110 \rangle \{110\}$ deformation twinning in $MgSiO_3$ post-perovskite derived from the performed atomic scale modeling

	Pairwise Potential	DFT (GGA)
$b_p = \frac{1}{6}[110], \text{Å}$	1.417	1.413
μ, GPa	247	312
s	0.588	0.597
$\gamma_{us}, \text{J/m}^2$	0.82	1.23
$\gamma_{isf}, \text{J/m}^2$	0.10	0.69
$\gamma_{ut}, \text{J/m}^2$	0.98	1.95
$2\gamma_{tsf}, \text{J/m}^2$	0.36	0.86
$\gamma_{TM}, \text{J/m}^2$	0.62	1.09
$\zeta, \text{Å}$	3.2	3.2

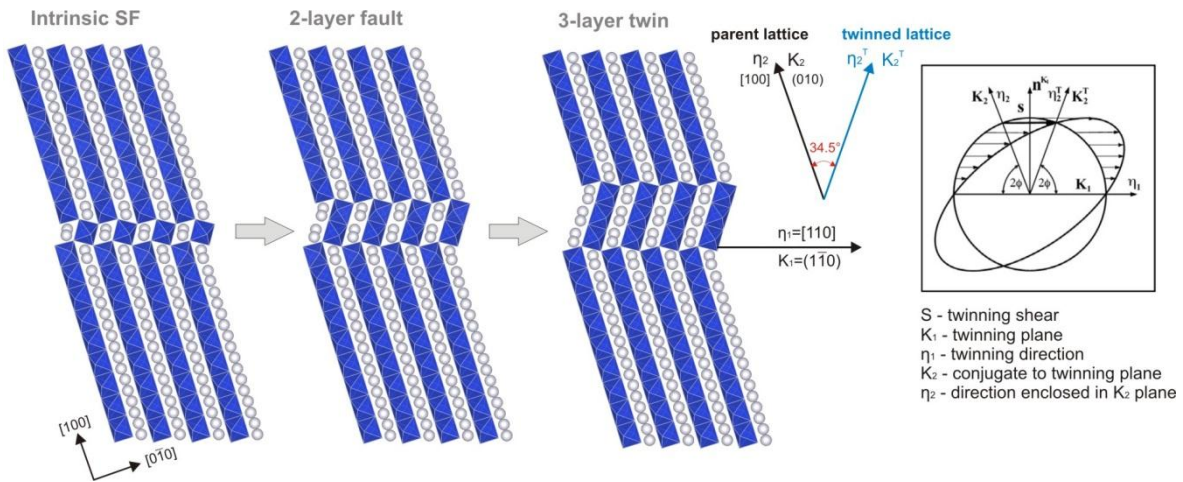


Fig. 6.8. Formation of $\frac{1}{2}\langle 110 \rangle \{110\}$ twinning in $MgSiO_3$ post-perovskite from the performed atomic-scale modeling. Each atomic configuration corresponds to the energy minimum on GPFE energy landscape presented on Fig. 6.7.

barrier γ_{us} and the first layer intrinsic stacking fault energy γ_{isf} reproduce the corresponding portion of the γ -line provided on the Fig. 6.6a. Nucleation of the second, third and subsequent $\frac{1}{6}[110]$ dislocations creates two-, three- and further N -layer stacking faults. The energy barrier opposed to appearance of each N -layer fault ($N > 1$) and twice the

energy of the twin stacking fault (*i.e.* accounting for the upper and lower twin boundary) are indicated on the GPFE landscape (Fig. 6.7) as γ_{us} and $2\gamma_{tsf}$, respectively. Energy difference between these two values defines the twin migration energy γ_{TM} . For the investigated twinning system in MgSiO₃ post-perovskite, convergence in γ_{TM} energy is reached after nucleation of the third twinning partial, resulting in total shear displacement by full 1/2[110] lattice repeat. Therefore, further nucleation and propagation of successive 1/6[110] dislocations represents twin growth on the developed three-layer twin nucleus. The geometry of 1/2<110>{110} twinning in MgSiO₃ post-perovskite can be described by rotation of the parent lattice by 34.5° around [001] axis as it is shown on Fig.6.8.

6.4.2 Twin nucleation model

At the mesoscale, morphology of a twin domain is considered as a lens characterized by thickness h and half-length l (Fig. 6.9). Boundaries of such a lenticular twin contain loops or half-loops of dislocations belonging to twinning planes equidistant from each other by Δh . A twin lens grows longer (along the twinning direction) by dislocation glide, while growing thicker (in the direction normal to the twinning plane) occurs through successive nucleation of new dislocation loops.

Total energy E_{tot} of a lenticular twin nucleation (Fig. 6.9) can be defined as:

$$E_{tot} = E_{GPFE} + E_{int} + E_{line} - W, \tag{6.1}$$

where E_{GPFE} is the twin boundary energy; E_{int} is the energy term resulting from interaction

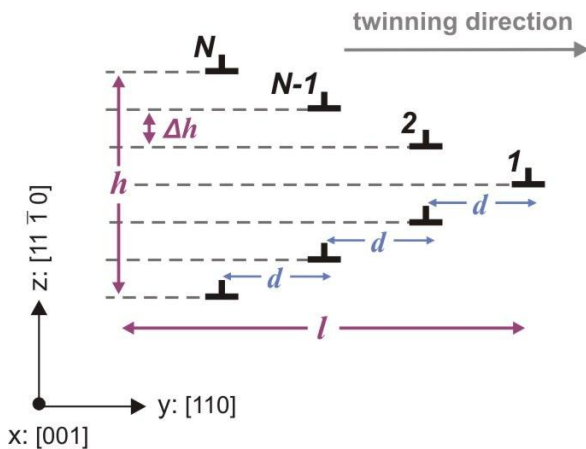


Fig. 6.9. Schematic illustration of a semi lenticular twin morphology characterized by thickness h , length l and invariant spacing d between each two neighboring twinning dislocations. Crystallographic directions correspond to the <110>{110} twinning in PPV considered in this work.

of twinning partials; E_{line} is the twin dislocation line energy; and W – the work of applied stress. Relying on the observed $\frac{1}{2}[110](\bar{1}\bar{1}0)$ dissociated dislocation core geometries and the corresponding γ -line energy, the mobile $\frac{1}{6}[110]$ dislocation partial is considered as the twinning dislocation with Burgers vector b_p . Being characterized by large twinning shear $s = b_p/\Delta h = \sim 0.6$ (Table 6.1; Fig. 6.7), twins in post-perovskite will be very thin compared to their length, by analogy with bcc metals where s is close to 0.7. As it has been shown by Cooper (1965, 1966), total energy of an extended twin lamella with $l \gg h$ can be considered as the energy of two flat surfaces containing twinning dislocations, *i.e.* contribution of $\{110\}$ interplanar spacing Δh of $\sim 2.4 \text{ \AA}$ into the distance between twinning dislocations can be neglected. In this study, distance between the i^{th} and the $(i+1)^{\text{th}}$ twinning dislocations belonging to one flat surface is assumed to be invariant and equal to d (Fig. 6.9).

Twin boundary energy E_{GPFE}

The main parameters needed to compute the energy E_{GPFE} of a twin boundary are extracted from the computed GPFE landscape (see section 6.4.1). The twin boundary energy E_{GPFE} consists of the two contributions: (i) the energy γ_{SF} , required to create the intrinsic stacking fault, and (ii) γ_{twin} , required to nucleate a twin. Relying on the acquired characteristics of the GPFE landscape (Table 6.1), these two terms can be defined as:

$$\begin{aligned} \gamma_{SF} &= \gamma_{isf} + \left(\frac{\gamma_{us} - \gamma_{isf}}{2} \right) \left[1 - \cos \left(2\pi \frac{f(y)}{b_p} \right) \right] \\ \gamma_{twin} &= \left(\frac{2\gamma_{tsf} + \gamma_{isf}}{2} \right) + \frac{1}{2} \left(\gamma_{ut} - \frac{2\gamma_{tsf} + \gamma_{isf}}{2} \right) \left[1 - \cos \left(2\pi \frac{f(y)}{b_p} \right) \right] \end{aligned} \quad (6.2)$$

with
$$f(y) = \frac{b_p}{2} + \frac{b_p}{N\pi} \left[\text{atan} \left(\frac{y}{\zeta} \right) + \text{atan} \left(\frac{y-d}{\zeta} \right) + \dots + \text{atan} \left(\frac{y-(N-1)d}{\zeta} \right) \right],$$

where $f(y)$ describes the disregistry function of N twinning dislocations characterized by the uniform half width ζ and distant from d along the twinning direction (Fig. 6.9). The half-width $\zeta = 3.2 \text{ \AA}$ is taken from the geometric characteristics of $\frac{1}{6}[110]$ edge dislocation partial, derived from the fully atomistic modeling of $\frac{1}{2}[110](\bar{1}\bar{1}0)$ edge dislocations (see

the previous section 6.1.2). For γ_{SF} , $f(y)$ is considered in the range $0 \leq f(y) \leq b_p$, corresponding to the pv -stacking fault region; while γ_{twin} is computed for $0 < f(y) \leq Nb_p$ with $N > 1$, describing the disregistry function of the twin nucleated on the existing stacking fault configuration.

Relying on the defined γ_{SF} and γ_{twin} analytic expressions (eq.6.2), the twin boundary energy can be computed as:

$$E_{GPF E}(d) = \int_0^d \gamma_{SF} dy + (N - 1) \int_0^d \gamma_{twin} dy, \quad (6.3)$$

where d is the distance between the twinning dislocations (Fig. 6.9).

Interaction energy E_{int} between twinning partials

As described above, a twin lamella in the post-perovskite can be considered as two flat surfaces composed of uniformly spaced dislocations, therefore the term E_{int} can be expressed through the summation of elastic interaction energies between parallel dislocations (similar to the approach for dislocation pile-ups). Thus, energy of the i^{th} twinning dislocation interacting with the $(i + 1)^{\text{th}}$ or $(i - 1)^{\text{th}}$ dislocation in a twin lamella is:

$$E_{i,i+1} = E_{i,i-1} = \frac{\mu b_p^2}{2\pi(1 - \nu)} \ln \frac{L}{d}, \quad (6.4)$$

where b_p is the twinning Burgers vector; μ is anisotropic shear modulus, L is the size of a crystal; ν is the Poisson ratio; and d is the spacing between the twinning dislocations.

In a twin lamella with $l \gg h$, where dislocations are assumed to belong to two flat surfaces which don't interact with each other, the total interaction energy of all twinning dislocation can be defined as:

$$E_{int} = \frac{\mu b_p^2}{2\pi(1 - \nu)} \left\{ N^2 \ln \frac{L}{d} - \ln(N - 2)! + \sum_{i=2}^{N-1} [\ln(N - i)! + \ln(i - 1)!] \right\}, \quad (6.5)$$

where N is the number of twinning dislocations; L is the size of a crystal; ν is the Poisson ratio; and d is the distance between the twinning dislocations. The limits of the sum

exclude the first and the last dislocations in order to avoid artificial accounting for interactions of these dislocations with themselves.

Dislocation line energy E_{line}

The dislocation line energy E_{line} does not depend on the spacing d between twinning dislocations. For N twinning dislocations, one finds:

$$E_{line} = N \frac{\mu b_p^2}{2\pi(1-\nu)}. \quad (6.6)$$

Work of applied stress

Assuming the applied stress σ_a to be uniform within the twin, the work of the applied shear stress is:

$$W = s\sigma_a hl = 2N^2\sigma_a b_p d. \quad (6.7)$$

6.4.3 Twin morphology and critical twinning stress

When all the energy terms contributing into E_{tot} (eq.6.1) are defined, the total energy of a twin lamella, with a constant number of twin layers N , can be represented as the function of the spacing d between the twinning dislocations (Fig. 6.10a). For twin nucleation in PPV, we have previously shown that $N=3$ corresponds to the stable twin nucleus. Therefore, in our calculations, we rely on this value. The minimum energy configuration corresponds to the equilibrium distance d_{eq} , which increases with applied stress due to the growth of the twin lamella along the $\langle 110 \rangle$ twinning direction. Thus, for the applied stress in the range of 10-100 MPa, d_{eq} varies from 37.5 Å to 41.8 Å and from 130.4 Å to 235.7 Å, while computing E_{GPFE} energy term relying on GPFE from DFT and pairwise potential, respectively. Based on these d_{eq} values, the ratio of thickness to length $\frac{h}{2l} = \frac{\Delta h}{d_{eq}}$ in a twin lamella is close to $6 \cdot 10^{-2}$ and $1.5 \cdot 10^{-2}$ for DFT and pairwise potential, respectively. Overall, similarly to the estimates done for the extension of $\frac{1}{2}[110](\bar{1}\bar{1}0)$ dislocation cores (see section 6.3), pairwise potential predicts $\langle 110 \rangle \{110\}$ twin domains to be ~ 5 times more extended (along the twinning direction) with respect to the twin morphology derived using data from DFT simulations.

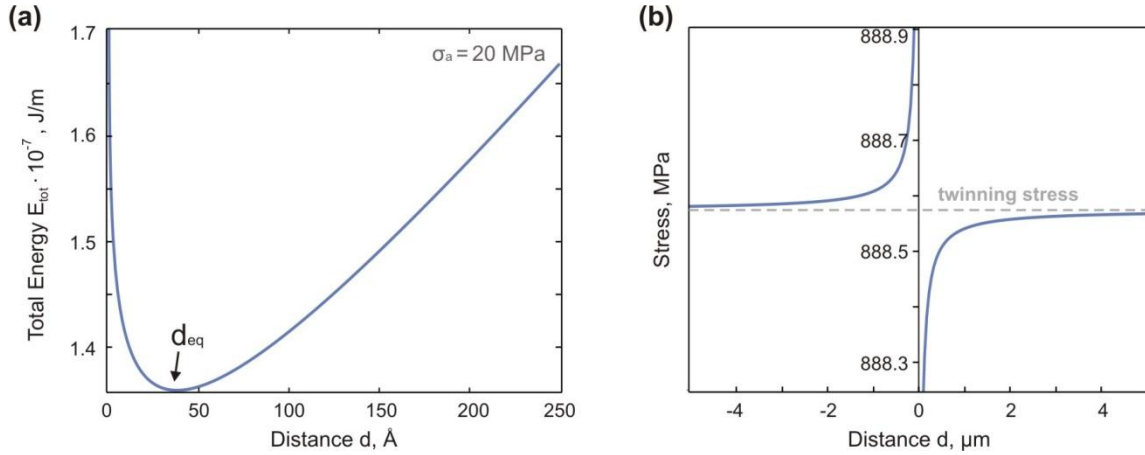


Fig. 6.10. (a) Total energy E_{tot} as a function of d computed at $\sigma_a=20$ MPa. (b) Critical twinning stress σ_{crit} . Both plots are produced relying on the data from DFT simulations.

Based on the computed energies, one can calculate the critical twin nucleation stress σ_{crit} while minimizing the total energy E_{tot} with respect to distance d : $\frac{\partial E_{tot}}{\partial d} = 0$. Thus, for the $\frac{1}{2}\langle 110 \rangle \{110\}$ deformation twinning, we find σ_{crit} of ~ 889 MPa (Fig. 6.10b) and ~ 212 MPa, relying on the data from DFT and the pairwise potential, respectively. These relatively low σ_{crit} values indicate that deformation twinning represents an important mechanism of plastic deformation within $\frac{1}{2}\langle 110 \rangle \{110\}$ system in MgSiO_3 post-perovskite.

In the literature, the twinning stress is also commonly referred as the so-called ideal twinning stress, which can be simply calculated as the maximum slope of the GPFE curve (Fig. 6.7) with respect to the shear displacement, *i.e.* as $\sigma_{ideal} = \pi \frac{\gamma_{TM}}{b_p}$ (Ogata *et al.* 2005). For the considered $\frac{1}{2}\langle 110 \rangle \{110\}$ system in MgSiO_3 PPV, the ideal stress σ_{ideal} is 13.8 GPa and 24.2 GPa, relying on the parameters acquired from the semi-empirical and *ab initio* GPFE curves (Fig. 6.7, Table 6.1). These values are almost 30 times larger than the corresponding critical twin nucleation stresses σ_{crit} . computed from the mesoscale model described above. Similarly, very high unrealistic values of σ_{ideal} , with at least one order of magnitude of difference with respect to σ_{crit} . (calculated with the twin nucleation model similar to that, used in this study) were reported for metal alloys, *e.g.* in L1_0 and 14M Ni_2FeGa (Wang and Sehitoglu 2013), Fe-based bcc alloys (Ojha *et al.* 2014) *etc.* Furthermore, for this metal alloys σ_{crit} was shown to be very close (few MPa of difference)

to the corresponding twinning stresses measured experimentally (Sutou *et al.* 2004; Timofeeva *et al.* 2012; Ojha *et al.* 2014). For MgSiO_3 post-perovskite, stable only at very high P - T conditions, there is no available experimental data on critical twinning stresses which could serve as the reference values to compare with. The only evidence of twinning in the post-perovskite structure was provided by TEM studies of deformed CaIrO_3 low pressure analogue material (Miyajima *et al.* 2010; Niwa *et al.* 2012), however the critical twinning stress for this phase was not measured.

6.5 Summary

In this chapter, we performed atomic-scale modeling of $\frac{1}{2}[110]$ defects in MgSiO_3 post-perovskite. Pairwise potential modeling of $\frac{1}{2}[110]$ screw and edge dislocations reveals their asymmetric dissociation in $(1\bar{1}0)$ plane into $\frac{1}{3}[110]$ and $\frac{1}{6}[110]$ partials separated by a widespread stacking fault forming a thin perovskite lamella. The employed pairwise potential parameterization (Oganov *et al.* 2000) was originally fitted for MgSiO_3 perovskite (bridgmanite) phase, therefore, it significantly underestimates (seven times) the energy of such a stacking fault configuration and, consequently, overestimates (about five times) the spreading of $\frac{1}{2}[110](1\bar{1}0)$ dislocation cores. Although the exact equilibrium width of the cores was not found, DFT calculations confirm such a perovskite lamella to be a stable stacking fault configuration for the $\frac{1}{2}\langle 110 \rangle\{110\}$ system. Both for the screw and edge dislocation cores, the short $\frac{1}{6}[110]$ partial is found to be mobile, while the longer $\frac{1}{3}[110]$ partial – immobile. The critical stress, needed to initiate the motion of $\frac{1}{6}[110]$ partial is 0.7 GPa and 2.8 GPa for screw and edge dislocations, respectively. Thus, in contrast to previously considered $[100]$ and $[001]$ Burgers vectors, edge dislocations will account for most of the plastic strain produced during plastic deformation along $\frac{1}{2}\langle 110 \rangle$.

Following observations from the TEM studies of CaIrO_3 PPV low pressure analogue (Miyajima *et al.* 2010; Niwa *et al.* 2012), we also examined the efficiency of $\frac{1}{2}\langle 110 \rangle\{110\}$ deformation twinning in high pressure MgSiO_3 PPV, considering mobile $\frac{1}{6}[110]$ partial as a twinning dislocation. At atomic scale, deformation twinning was investigated via generalized planar fault energy (GPFE) landscapes, which were further integrated into mesoscale twin formation model, providing $\frac{1}{2}\langle 110 \rangle\{110\}$ critical twin formation stress of ~ 0.9 GPa, relying on the data from DFT simulations.

CHAPTER 7

Discussion and Implications

Knowledge about intrinsic microscopic deformation mechanisms is essential for understanding macroscopic rheological properties of a material. This chapter outlines the main results inferred from the performed atomic-scale modeling of defects in MgSiO_3 post-perovskite and describes some aspects of the macroscopic behavior which can be directly deduced from them. Comparing dislocation mobility in different slip systems at 0 K allows describing anisotropic lattice friction of the layered post-perovskite structure. In order to further describe thermally activated dislocation glide at the D'' conditions, evolution of the critical resolved shear stress (CRSS) with temperature is computed based on the kink-pair formation enthalpies acquired from the atomic-scale modeling. Relying on the computed rheological characteristics of the post-perovskite phase, we also discuss some important geophysical implications, highlighting the weakness of D'' layer and possibility of seismic waves attenuation and energy dissipation in this region.

7.1 Structures of dislocation cores in MgSiO₃ post-perovskite

In this study we investigate the structures of [100], [001] and $\frac{1}{2}\langle 110 \rangle$ dislocation cores based on the full atomistic modeling approach, *i.e.* while directly introducing the corresponding displacement field into atomic arrays. Compared to the Peierls-Nabarro (PN) model (Peierls 1940; Nabarro 1947), this method allows avoiding the uncertainties which possibly may be inherited from the γ -surface calculations and/or from the choice of the Peierls potential periodicity a' . Also, direct atomistic modeling of dislocation cores requires using large atomic arrays which are not always affordable for high accuracy *ab initio* calculations, but can be rather investigated relying on empirical pairwise potentials. In this work, only [100] screw dislocations, characterized with the shortest Burgers vector of 2.5 Å, are modeled both from the first principles and with the semi-empirical approach. Full atomistic modeling of all edge dislocations and of the $\frac{1}{2}\langle 110 \rangle$ and [001] screw dislocations in the post-perovskite can only be performed with the pairwise potential because these dislocations are characterized by widespread dislocation cores, which require using simulation cells containing in excess of 40,000 atoms, *i.e.* far beyond computational capabilities of the first-principle simulations.

[100] dislocations

Computed at atomic scale both with DFT and pairwise potential, screw dislocations with [100] Burgers vector exhibit compact planar cores centered between two neighboring Mg atoms and spread in {011}. In the Mg-layer, the stable core configurations are distant by $a' = \frac{1}{2}[001]$. This distance defines the periodicity of the Peierls potential in (010) plane. The dislocation core spreading, characterized by a half-width ζ of ~ 1.9 Å, is limited by the Si-layers (Fig.4.1). The geometrical characteristics of the core produced by the two simulation techniques are in good agreement (less than 5% of difference in the dislocation core spreading). Thus, the chosen pairwise potential parameterization chosen appears to reproduce well the core structures, *i.e.* configurations far from the equilibrium where the potential was originally fitted (Oganov *et al.* 2000). This further confirms the transferability of the pairwise potential for modeling defects in post-perovskite which was inferred from the γ -surface calculations, provided in Chapter 3.

The extension of the [100] screw dislocation cores obtained in our study is in reasonable agreement with previous results based on the PN model (Carrez *et al.* 2007a), which rely on γ -lines from the first-principles calculations performed with the same GGA approximation and pseudopotentials as employed in this study. The classical PN model showed that the compact [100] screw dislocation should have a half-width of 1 Å in {011}. Discrepancies in core size between the present results and those of the PN model can be largely attributed to the GSF calculations (Fig. 3.4c). GSF computed by Carrez *et al.* (2007a) involves atomic layers above the actual spreading layer of the core, delimited by neighbouring Mg rows. Consequently, the GSF energies used in the PN model were overestimated, leading to a narrower core. Despite a core spreading in {011}, the easiest glide plane of [100] screw dislocations is (010). This is the result of a glide alternating between (011) and (0 $\bar{1}$ 1), defining a global macroscopic glide plane (010). This non-standard behaviour could be evidenced only by full atomistic calculations and could not be deduced from the PN model. The observed path of [100] screw dislocations glide represents an interesting case which challenges the hypothesis and relevance of the PN model in this case.

In this work, [100] edge dislocations lying on (010), (011) and (001) planes are only computed with the pairwise potential because of the large simulation cells needed. All those dislocations are characterized by compact symmetric cores (Fig. 4.5) with a half width ζ close to $2b \sim 5$ Å. For these dislocation cores, the PN model (Carrez *et al.* 2007a) leads to ζ values below 2 Å, which mainly results from the higher γ -energies (Fig. 3.4a-c).

[001] dislocations

Atomistic modeling of [001] screw and edge dislocations (performed with the pairwise potential) indicates their dissociation in (010) into two symmetric partials separated by a stacking fault (Fig. 5.1, 5.4). Both dislocations exhibit mixed characters and are characterized by the presence of $\langle 100 \rangle$ components (Fig. 5.9). In case of edge dislocations, $[001] \rightarrow \frac{1}{2}[101] + \frac{1}{2}[\bar{1}01]$ dissociation is observed, while for the screw dislocations, this dissociation scheme involves high energy configurations and the $\langle 100 \rangle$ component reaches only 15% in stable dislocation cores.

Dissociation of [001] screw and edge dislocations in the (010) plane was previously investigated from the first principles based on the Peierls-Nabarro (PN) model (Carrez *et*

al. 2007a,b). However, these early studies were focused on pure screw and pure edge dislocation cores without taking into account the presence of $\langle 100 \rangle$ component, *i.e.* mixed [001] dislocation cores have been never modeled before. As it can be expected, the predicted dissociation width of 16.2 Å for pure [001](010) edge dislocations (Carrez *et al.* 2007a,b) is significantly lower, than the value of 41.6 Å found in this work for the mixed dislocation core. Nevertheless, for the screw dislocations characterized by only 15% $\langle 100 \rangle$, both the separation distance $R = 10.8$ Å and the half-width of each partial $\zeta = 1.0$ Å compare well with the values $R = 9.9$ Å and $\zeta = 1.1$ Å predicted by the PN model for the pure [001] screw dislocation core (Carrez *et al.* 2007a,b).

$\frac{1}{2}\langle 110 \rangle$ dislocations

Full atomistic modeling of $\frac{1}{2}[110]$ screw and edge dislocations performed with the pairwise potential reveals their spontaneous dissociation in $(1\bar{1}0)$ plane into $\frac{1}{3}[110]$ and $\frac{1}{6}[110]$ partials separated by a widespread stacking fault where Si-octahedra are interconnected with neighboring Si-polyhedra by corners creating a thin perovskite lamella (Fig. 6.2 and 6.4 in Chapter 6). Such configuration of the stacking fault related to the $\frac{1}{2}\langle 110 \rangle \{110\}$ system is favored due to the structural relation between perovskite and post-perovskite phases where [001] direction is kept in common for both phases, and where $[110]^{\text{PPV}}$ and $[1\bar{1}0]^{\text{PPV}}$ directions correspond to the $[010]^{\text{PV}}$ and $[100]^{\text{PV}}$ vectors, respectively (see section 1.2 in Chapter 1). The pairwise potential employed in this study was originally adjusted for MgSiO_3 perovskite (bridgmanite) phase and it is shown to significantly underestimate (7 times) the energy of such a stacking fault configuration. This results in notably overestimated spreading of the dislocation cores. However, DFT calculations confirm that perovskite lamella represents the stable stacking fault configuration for the $\frac{1}{2}\langle 110 \rangle \{110\}$ slip system (for more details see section 6.3 in Chapter 6). By analogy, full atomistic modeling performed for the [100](010) and [010](100) dislocations in MgSiO_3 bridgmanite (orthorhombic perovskite phase) indicate the presence of PPV-type interconnections of Si-polyhedra (*i.e.* nucleus of 2D layers) in the edge dislocation cores. For cubic and rhombohedral perovskites, *e.g.* in SrTiO_3 (Hirel *et al.* 2012; 2016) and KNbO_3 phases (Hirel *et al.* 2015), similar PPV-like stacking fault configurations were reported for $\langle 110 \rangle \{110\}$ dislocation cores, corresponding to the

[100](010) and [010](100) systems in the lower symmetry orthorhombic reference. Thus, the atomic scale modeling performed in this work emphasizes the role of $\frac{1}{2}\langle 110 \rangle \{110\}$ dislocations in MgSiO_3 PPV for the $\text{PPV} \rightarrow \text{PV}$ phase transition. The role of defects for the transformation between the two phases was previously considered only in the simple context of successive accumulation of $\langle 110 \rangle \{110\}$ stacking faults in post-perovskite (Oganov *et al.* 2005) and [101](010) stacking faults in orthorhombic perovskite (Zahn 2011).

Similar behavior is also known for the Al_2SiO_5 polymorphs. TEM studies of these phases report that the stacking fault between the two $\frac{1}{2}[100](010)$ partials in sillimanite represents a thin lamella of kyanite phase (Doukhan and Christie, 1982; Doukhan *et al.* 1985). Another example of dislocation induced structural transformations can be found in numerous SiC phases where activation of partial dislocations in basal plane prompts polymorphic transformations, such as $3\text{C} \rightarrow 6\text{H}$ and $4\text{H} \rightarrow 3\text{H}$ (Pirouz and Yang 1993; Duval-Riviere and Vicen 1994).

In this work, we also highlight the importance of $\frac{1}{2}\langle 110 \rangle$ defects in post-perovskite for plastic deformation along the [010] direction. In this phase, dislocations with the [010] Burgers vector, corresponding to the largest unit cell parameter (8.12 Å), will dissociate into two $\frac{1}{2}\langle 110 \rangle$ dislocations, in agreement with Franck's criterion ($b^2 > b_1^2 + b_2^2$) and with the symmetry of the base-centered *C*-lattice. Due to the very short [100] lattice repeat, full $\frac{1}{2}\langle 110 \rangle$ burgers vector length (4.253 Å) is only 4.5% larger than $\frac{1}{2}[010]$ lattice repeat (4.062 Å).

7.2 Anisotropic lattice friction

Lattice friction of a material describes its mechanical resistance opposed to dislocation motion. This intrinsic characteristic is commonly assessed in absence of thermal activation through the Peierls potential V_P (the energy barrier opposed to the glide of a straight infinite dislocation line at 0 K) or through the Peierls stress σ_p (the critical stress required to move a straight dislocation at 0 K). Computing these values for different slip systems provides anisotropic lattice friction of a material, a key parameter for understanding its anisotropic plasticity. In this work, the Peierls potential was directly computed only for the [100] screw dislocations, and Peierls stress – for all the screw and edge dislocations,

Table 7.1

Peierls stress values computed for the [100], [001] and $\frac{1}{2}\langle 110 \rangle$ screw and edge dislocations in MgSiO_3 post-perovskite

Slip system	Peierls stress σ_p , GPa	
	Screw	Edge
[100](010)	1.0 // 2.3*	<0.1
[100](011)	>10.4	~0.12
[100](001)	17.5	~0.1
[001](010)	3.0	2.0
$\frac{1}{2}\langle 110 \rangle \{110\}$	0.7	2.8

* DFT calculations

therefore, we describe anisotropic lattice friction with the latter one. All the Peierls stress values calculated with the pairwise potential (and DFT for [100] screw dislocations only) are summarized in Table 7.1.

Lattice friction opposed to the glide of [100] dislocations, *i.e.* dislocations with the shortest Burgers vector, is found to be highly anisotropic. Mobility of [100] edge dislocations is generally much higher than that of screw dislocations (more than an order of magnitude of difference in the Peierls stress), regardless of the glide plane. Therefore, screw dislocations will account for most of the plastic strain produced during deformation. At the same time, glide of [100] screw dislocations through MgSiO_3 post-perovskite structure is characterized by significantly different Peierls stress while moving in (010) within MgO layer or across the rigid SiO_2 layers. According to the results of the performed atomic scale modeling, lattice friction opposed to the glide of [100] screw dislocations in (010) is one order of magnitude lower than that in (001). This behavior clearly results from the anisotropic crystal chemistry due to the difference in the Mg-O and Si-O bond strength.

Full atomistic modeling of [001] dislocations indicates their spontaneous dissociation in (010), therefore we consider them gliding in (010) only. In contrast to the [100] dislocations, the contrast in Peierls stress between screw and edge [001] dislocations is not so high. Lattice friction opposed to the glide of [001] screw dislocations is 3 GPa, while

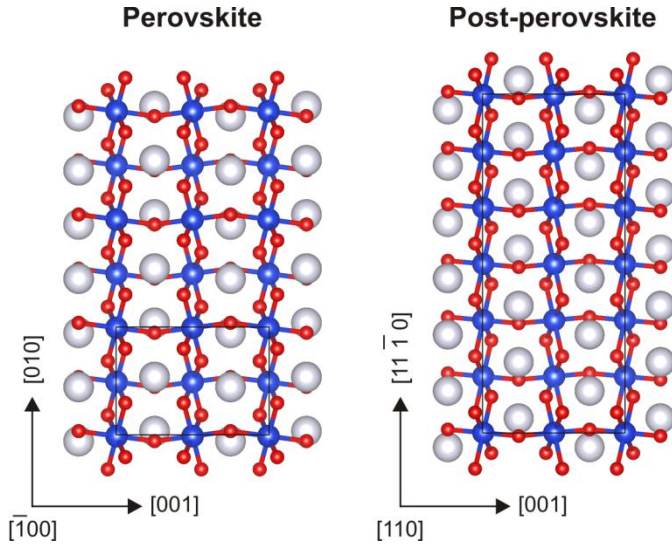


Fig.7.1. Structural relation between $MgSiO_3$ perovskite (bridgmanite) and post-perovskite at 120 GPa. Si atoms are shown with blue balls, Mg –with gray, and O – with red.

that of edge dislocations is 33% lower (Table 7.1). Therefore, plastic deformation within $[001](010)$ slip system will be governed by the screw dislocations.

Structural relaxation of screw and edge $\frac{1}{2}[110]$ dislocations reveals their spontaneous dissociation in $(1\bar{1}0)$ into $\frac{1}{6}[110]$ and $\frac{1}{3}[110]$ partials where the first one is found to be mobile and the second one – immobile. The Peierls stress values provided in Table 7.1 correspond to the critical stress needed to initiate the motion of the mobile $\frac{1}{6}[110]$ partial. In contrast to the $[100]$ and $[001]$ dislocations, for $\frac{1}{2}\langle 110 \rangle\{110\}$ system, lattice friction opposed to the glide of screw dislocations is lower than that for edge dislocations. The reason of such unusual behavior can be explained while analyzing the stacking fault structure between the partials, where Si-octahedra create a thin perovskite lamella. Thus, motion of the leading partial through the post-perovskite crystal structure involves propagation of the perovskite lamella along $[001]$ direction in case of screw dislocations and along $\langle 110 \rangle$ direction in case of edge dislocations. The PPV structure inherits the $[001]$ crystallographic direction of the PV phase (Fig.1.5 in Chapter 1). Consequently, the structural difference between PV and PPV is minimal in this direction (Fig.7.1). Therefore, propagation of the PV-lamella in the PPV matrix appears to be easier along $[001]$, *i.e.* due to the motion of $\frac{1}{6}[110]$ $(1\bar{1}0)$ screw dislocation partial in our case.

For the $\frac{1}{2}\langle 110 \rangle\{110\}$ slip system we also performed atomic-scale modeling of twinning. The critical twin nucleation stress is found to be ~ 900 MPa based on DFT calculations and ~ 200 MPa based on the pairwise potential modeling. These relatively low

stress values indicate that deformation twinning related to the $\frac{1}{2}\langle 110 \rangle \{110\}$ system represents an important deformation mechanism in MgSiO_3 post-perovskite. Taking into account the high strain rates involved in deformation experiments, one can expect appearance of $\langle 110 \rangle \{110\}$ twin domains affecting the deformation textures of aggregates. Indeed such domains were observed with TEM after DAC deformation experiments on CaIrO_3 (see Table 1.1 in Chapter 1, experiments by Miyajima *et al.* (2010) and Niwa *et al.* (2012)).

Easy glide of [100] and [001] dislocations in (010) is also in agreement with the TEM observations of dislocations in deformed CaIrO_3 and CaPtO_3 post-perovskite structural analogues (see Table 1.1 in Chapter 1). In other words, theoretical and experimental evidence of dislocations in post-perovskites consistently indicates, that plastic deformation along (010) layers appears to be much easier than in other directions. Thus, the structural layering can be inferred to be responsible for the anisotropic plasticity of the post-perovskite. This behavior is significantly different from that in rather isotropic bridgmanite where all Si-octahedra are interconnected along the three directions creating a rigid 3D network. In this context, one can expect that general character of plasticity of the post-PPV phases (see section 1.3 in Chapter 1), where Si-polyhedra also form a rigid network, to be similar to that in bridgmanite, *i.e.* close to isotropic.

Lattice friction of high-pressure silicates in the lower mantle

To highlight the importance of the low lattice friction opposed to the dislocation glide in (010) layers in MgSiO_3 post-perovskite, it's worth comparing our results with the lattice friction in MgSiO_3 bridgmanite, the main component of the overlying mantle. Previous atomic-scale study of bridgmanite by Hirel *et al.* (2014), performed with the same pairwise potential parameterization, indicates that pressure has a strong effect on the lattice friction and the latter has been shown to increase significantly over the pressure range of the lower mantle. Figure 7.2 compares the Peierls stress of the easiest screw dislocations in MgSiO_3 bridgmanite with that in post-perovskite of the same composition. The change in crystal structure results in a drop of lattice friction. From completely different perspective, our calculations support the suggestion by Ammann *et al.* (2010), based on the study of anisotropic diffusion in MgSiO_3 , that the transition of bridgmanite to post-perovskite will be responsible for the weak D'' layer in regions dominated by the post-perovskite phase.

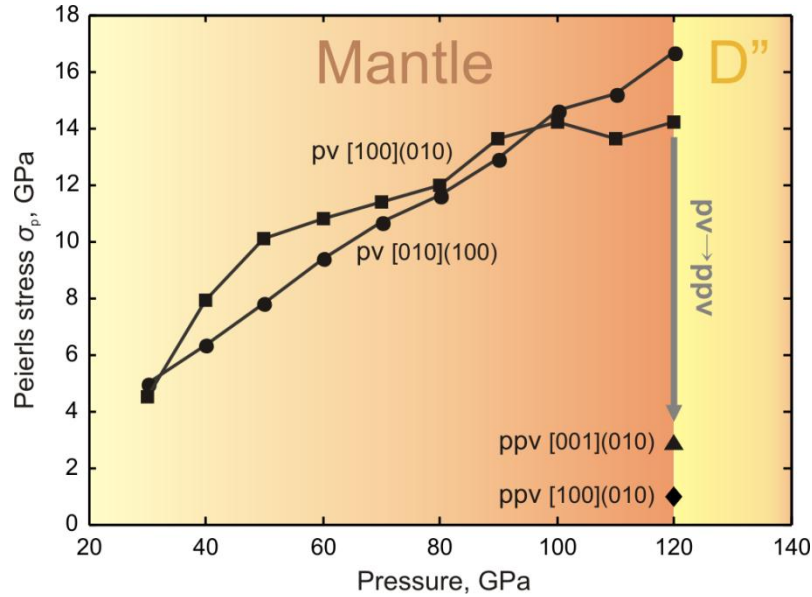


Fig. 7.2. Lattice friction opposed to the easiest dislocation glide in $MgSiO_3$ perovskite (PV), also called bridgmanite, and in post-perovskite (PPV) in the lower mantle pressure range. The Peierls stress values for PV phase are taken from Hirel et al. (2014).

7.3 Thermally activated dislocation glide

The anisotropic lattice friction described in the previous section corresponds to the intrinsic resistance of the crystal lattice at 0 K only. The Peierls stress σ_p , characterizing lattice friction, is commonly viewed as the critical resolved shear stress (CRSS) in absence of thermal activation. To determine how CRSS evolve in the conditions of the D'' layer, it is necessary to model thermal activation of dislocation glide. At finite temperature, the actual motion of dislocations occurs through nucleation and propagation of kink-pairs. The nucleation process corresponds to a small segment of dislocation line which bulges over the Peierls potential, then the further migration of the kinks is responsible for the glide of the whole dislocation line to the next stable position. The key parameter describing the efficiency of the dislocation glide at finite temperature is the critical kink-pair formation enthalpy ΔH_{2k} . In this study, evolution of the latter with applied stress was computed based on the LT model for the [100](010) screw dislocations (see section 4.5 in Chapter 4), relying both on the pairwise potential modeling and on DFT calculations. For the

[001](010) screw dislocations, the $\Delta H_{2k}(\sigma=0)$ value is estimated (see section 5.6 in Chapter 5) based on the observed dislocation core characteristics inferred from the pairwise potential modeling.

For the kink-pair mechanism, the shear strain rate $\dot{\epsilon}$ can be defined as the function of dislocation glide velocity \bar{v} and density of mobile dislocations ρ through Orowan's equation $\dot{\epsilon} = \rho b \bar{v}$. Combining this equation with the assumption of a dislocation velocity controlled by kink-pair nucleation, the strain rate $\dot{\epsilon}$ can be described with the following expression:

$$\dot{\epsilon} = \frac{\rho L a' b^2 \nu_D}{2w^2} \exp\left(\frac{-\Delta H_{2k}(\sigma)}{kT}\right), \quad (7.1)$$

where ρ is the mobile dislocation density; b is the Burgers vector length; a' stands for periodicity of the Peierls potential; w corresponds to the kink-pair width; $L = 1/\sqrt{\rho}$ describes the average length of dislocation lines; ν_D is the Debye frequency; and k is the Boltzmann constant. Thus, according to the Orowan's equation, a dislocation segment of length L glides with a velocity \bar{v} at a certain strain rate $\dot{\epsilon}$. Efficiency of this motion at finite temperature depends on the kink-pair formation enthalpy $\Delta H_{2k}(\sigma)$. Evolution of the ΔH_{2k} with applied stress can be further parameterized over the whole range of stress (from 0 to σ_p) using the continuous formulation by Kocks *et al.* (1975):

$$\Delta H_{2k}(\sigma) = 2H_k \left(1 - \left(\frac{\sigma}{\sigma_p}\right)^p\right)^q, \quad (7.2)$$

where σ_p is the Peierls stress; p and q are adjustable parameters; and $2H_k(\sigma=0)$ is the total activation enthalpy, corresponding to twice the energy of an isolated kink at no applied stress. Relying on the equations (7.1) and (7.2), one can express the CRSS as the function of temperature:

$$\sigma = \sigma_p \left(1 - \left(C \frac{T}{2H_k}\right)^{1/q}\right)^{1/p} = \sigma_p \left(1 - \left(\frac{T}{T_a}\right)^{1/q}\right)^{1/p}, \quad (7.3)$$

where $C = \ln \frac{2\dot{\epsilon}w^2}{\rho a' b^2 \nu_D}$ is a function of a strain rate $\dot{\epsilon}$, dislocation density ρ , and the kink geometry: width w and height a' ; T_a is the so-called athermal temperature at which lattice friction of a material vanishes.

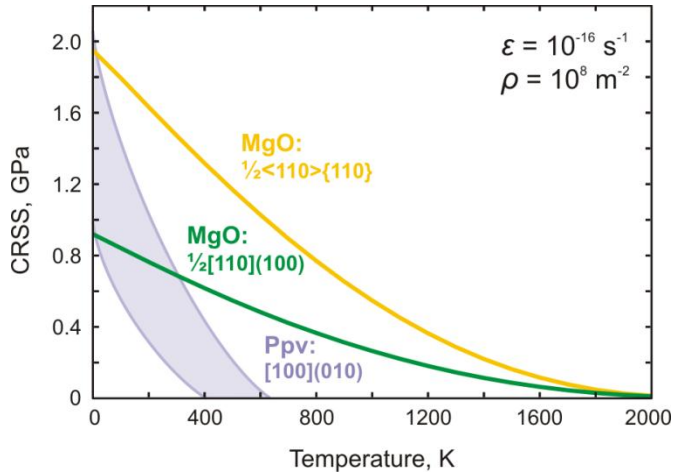


Fig. 7.3. Evolution of CRSS with temperature for $[100](010)$ in PPV at 120 GPa, compared with that for $\frac{1}{2}[110](100)$ and $\frac{1}{2}\langle 110 \rangle \{110\}$ in MgO at 100 GPa (Cordier *et al.* 2012). Strain rate $\dot{\epsilon}$ and dislocation density ρ correspond to the lower mantle conditions.

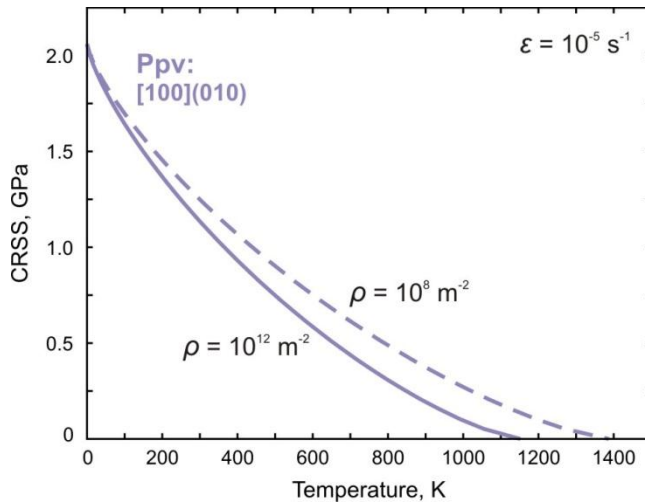


Fig. 7.4. Evolution of CRSS with temperature for $[100](010)$ in PPV at 120 GPa at strain rate $\dot{\epsilon}$ and dislocation density ρ corresponding to experimental conditions.

For $[100](010)$ dislocation cores, relying on the computed $2H_k = 2.69$ eV, $p = 0.73$ and $q = 1.31$ from LT model based on DFT calculations, one can find that, at the lower mantle conditions characterized by strain rates $\dot{\epsilon}$ in the order of 10^{-16} s^{-1} and dislocation density $\rho = 10^8 \text{ m}^{-2}$, lattice friction vanishes at the critical temperature $T_a = 600$ K (Fig. 7.3). With the lower $2H_k = 1.71$ eV, $p = 0.82$ and $q = 1.50$ values from the pairwise potential modelling, T_a is close to 400 K (Fig. 7.3). These temperatures are far below the temperature of 3700 – 4400 K (Boehler 2000; Alfè *et al.* 2002) expected in the lowermost mantle, therefore $[100]$ dislocation glide at D'' conditions can be expected to occur in the athermal regime. Considering experimental conditions, *i.e.* strain rates $\dot{\epsilon} = \sim 10^{-5} \text{ s}^{-1}$ and dislocation density $\rho = 10^{12} \text{ m}^{-2}$ (Fig. 7.4), we find that for the $[100](010)$ system in MgSiO_3 post-perovskite

lattice friction vanishes when the temperature is raised above 1100 K (as an upper bound defined based on data from DFT calculations).

In case of dissociated [001](010) screw dislocation cores with much more complex geometry (Fig. 5.1, Chapter 5), we did not determine the full curve describing the evolution of the kink-pair formation enthalpy with applied stress, but only estimated the maximum $2H_{2k}=8.3$ eV values describing the energy of the two isolated kink-pairs nucleated simultaneously on the two partials without changing the stacking fault width (as it is shown on Fig. 2.15a, Chapter 2), relying on the elastic interaction model by Koizumi *et al.* (1993). In conjunction with the equation (7.3), we assume that the kink-pair enthalpy $2H_{2k}$ scales linearly with kT (Kubin 2013). Then, once $2H_{2k}(\sigma=0)$ is defined, the athermal temperature T_a relevant for glide of dissociated [001](010) dislocations can be estimated as $T_a = \frac{2H_{2k}}{\kappa C}$. Employing the dislocation density $\rho = 10^8$ m⁻² and the strain rate $\dot{\epsilon} = 10^{-16}$, typical for lower mantle conditions, provides the athermal temperature $T_a = 1950$ K. These results suggest that [001](010) dislocation glide at the D'' conditions in MgSiO₃ post-perovskite would rather occur in the athermal regime.

7.4 Implications

Textures and CPO development. The most testable implication of our results is, of course, that strong crystal preferred orientation should result from preferential dislocation glide in (010) upon flow in the D'' layer. This is an important parameter because this layer has long been recognized as highly anisotropic. Although no consensus has yet been reached (see, for instance, Cottaar *et al.* (2014)), our finding that PPV exhibits dominant easy glide in (010) is consistent with the recent seismological studies by Nowacki *et al.* (2013) and Ford and Long (2015). However, our results cannot account for the (001) textures systematically observed after DAC experiments on silicate and germanate post-perovskites (see Table 1.1 in Chapter 1 for the overview). This CPO could rather originate from inherited transformation textures, which could be further enhanced by dislocation glide in (001) on pre-textured samples under very high stresses produced in DAC. Other processes, like grain boundary sliding, also may affect the resulting CPO. This discrepancy still remains to be clarified.

Low viscosity. Our results demonstrate that the presence of weak {010} Mg-layers in MgSiO_3 post-perovskite leads to dislocation structures that can easily glide, almost without affecting rigid Si-layers, especially in case of the shortest Burgers vector of 2.5 Å. The relative ease of slip between silicate PPV and periclase (Fig.7.3) demonstrates that, due to the structural layering, the high pressure MgSiO_3 phase can be as ductile as MgO. Under lower mantle conditions, these two phases are expected to deform in the athermal regime, *i.e.* lattice friction is overcome at a critical temperature T_a below the temperature range of 3700-4400 K (Boehler 2000; Alfè *et al.* 2002), expected in the D'' layer. In absence of intrinsic resistance of the lattice, dislocation creep is controlled by interaction of dislocations and by its rate of recovery which is ultimately controlled by diffusion. Diffusion in MgSiO_3 post-perovskite is known to be highly anisotropic (Amman *et al.* 2010). The fastest diffusion in this phase occurs along the shortest [100] direction (Fig.7.5) and the corresponding diffusion coefficient is very close to that in MgO. Again here, one can see the proximity between MgO periclase and the MgO sublattice in MgSiO_3 post-perovskite. Taking into account that both MgO and PPV deform in the athermal regime and have similar characteristics of the (fast) diffusion, one can expect that these phases exhibit comparable creep properties and hence viscosities. Contribution of more difficult deformation mechanisms normal to structural layering (either involving dislocations or slowest diffusion) may however affect (which is difficult to evaluate quantitatively at this point) the strength of polycrystalline PPV aggregates. The latter may be slightly stronger than coexisting periclase. The respective point defect chemistry of both phases may also

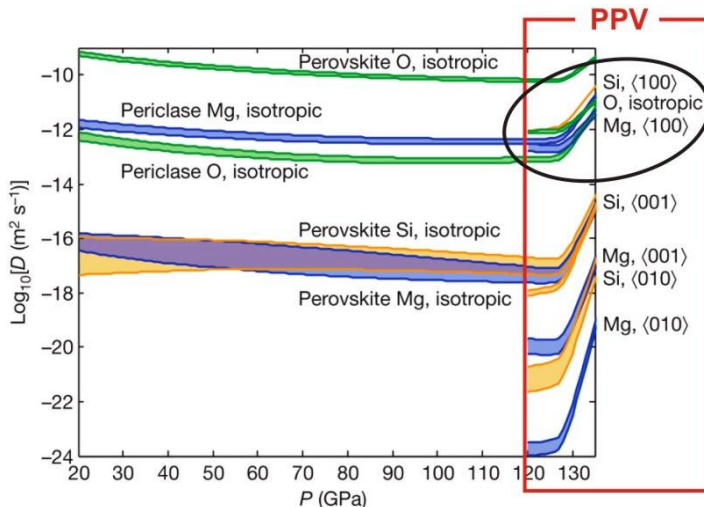


Fig. 7.5. Vacancy diffusion coefficients along a geotherm in the lower mantle inferred from the first-principles calculations by Ammann *et al.* (2010).

affect diffusion in one or the other direction. At this stage we can only highlight the fact of surprising resemblance between the two phases.

The implications of a low viscosity layer have already been considered and discussed. The strongest implication is the enhancement of heat transfer from the core across the CMB, as earlier predicted by Buffett (2007) and more recently investigated numerically (Nakagawa and Tackley (2011), Deschamps and Tackley (2014)).

Attenuation of seismic waves. Besides, viscosity, low lattice friction in silicate post-perovskite may also have important implications regarding seismic wave attenuation. A seismic (body) wave corresponds to strains in the range of 10^{-8} - 10^{-6} , with periods in the range of 1-10 s. These values correspond to stresses of a fraction of a MPa at most, applied at a strain rate of 10^{-6} s^{-1} or lower. Under these conditions, the athermal temperature T_a will be lower than 1400 K (the value corresponding to a strain-rate of 10^{-5} s^{-1} (to assess the response of a seismic wave), constraining the dislocation density at 10^8 m^{-2} on Fig.7.4). This result shows that PPV will be in the athermal regime under seismic loading conditions at temperatures of the D'' layer, with dislocations moving freely without lattice friction.

This situation has not been considered up to now for seismic attenuation because most discussions have been driven by the example of olivine (Karato and Spetzler 1990; Karato 1998). Olivine exhibits high lattice friction; thus, dislocations are prescribed to stay in their Peierls valleys, and dislocation damping can only result in a limited contribution from kink migration (Karato and Spetzler 1990; Karato 1998). For this reason, the most important source of attenuation in olivine has been linked to diffusionally assisted grain boundary sliding (Jackson *et al.* 2010).

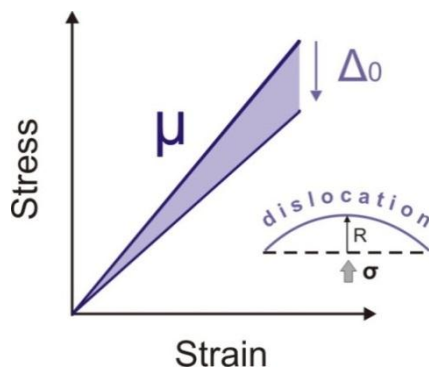


Fig. 7.6. Schematic illustration of the relaxation strength due to bowing of dislocations in absence of lattice friction.

Under an applied stress σ_a and without lattice friction, a dislocation segment of length l will bow out with a curvature $R = \frac{1}{2} \frac{\mu b}{\sigma_a}$. This bowing gives rise to a reduction of the effective shear modulus (Fig. 7.6), called the *modulus defect* or *relaxation strength*: $\frac{\Delta\mu}{\mu} = \Delta_0 = \frac{1}{6} \rho l^2$, where ρ is the dislocation density (Nowick and Berry 1972). Assuming that l scales with $\frac{1}{\sqrt{\rho}}$, one can conclude that Δ_0 could be as high as 15% (as an upper bound). Consequently, a shear wave travelling through the post-perovskite containing dislocations could encounter a maximum velocity reduction $\frac{\Delta V_S}{V_S}$ of approximately 7% compared to the ideal structure. In this regime, dislocation damping can be described using the vibrating string model (Nowick and Berry 1972) which assumes that under an applied alternating stress, a dislocation characterized by a line tension can execute forced vibrations like a vibrating string. An alternating stress, such as the one associated with a seismic wave, will result in damping and energy dissipation. This model has two important consequences. At sufficiently high frequency, there exists a peak in $\tan\phi$ versus ω with a resonance at ω_0 such that $\omega_0^2 = \frac{12\Gamma}{m_l l^2}$. The frequency ω_0 is a function of Γ , *i.e.*, the line tension of the dislocation, as previously computed, and of m_l , the effective mass per unit length of the dislocation line. This effective mass m_l can be computed by summing the squared displacements dq_i of all atoms i in a simulation cell in which a dislocation has moved from one Peierls valley to the next one, *i.e.*, by $dQ=a'$, using the following expression (Vegge *et al.* 2001):

$$m_l = \sum_i M_i \left(\frac{dq_i}{dQ} \right)^2. \quad (7.4)$$

In the previous expression, M_i corresponds to the mass of atom i ; the effective mass of the dislocation thus accounts for the kinetic energy of surrounding atoms as if they were to respond adiabatically to dislocation motion. Computed from different cell sizes to account for finite size effects, we find (in units of atomic mass per unit length) $m_l \sim 9.7 \text{ u}/\text{\AA}$, which results in $\omega_0 \sim 3.3 \cdot 10^4 \text{ s}^{-1}$. This frequency is higher than that of seismic waves, but it could allow experimental verification in the laboratory. At lower frequencies corresponding to seismic waves, the internal friction is proportional to ρl^4 and to the frequency ω .

Our proposition of post-perovskite being highly attenuating is consistent with the earlier report of seismic attenuation in the D'' by Anderson and Hart (1978) and more recently by Lawrence and Wysession (2006). However, attenuation in the heterogeneous D'' layer is still not well constrained and the resulting shear attenuation profiles, expressed in terms of quality factor Q_μ , differ by more than 30% (see reviews by Romanowicz and Durek 2000; Romanowicz and Mitchell 2007). Moreover, some seismological studies report a continuous decrease in attenuation from the top of the lower mantle to its bottom (Hwang and Ritsema 2011). This discrepancy may come from the difference in methods between these studies (Durand *et al.* 2013) and/or from the fact that their measurements sample different regions of the deep mantle. In this context, possible attenuation of seismic waves in the lowermost mantle deserves more attention in the future as it may serve a feasible marker of the post-perovskite phase in this region.

CONCLUSIONS

The key objective of this work was to investigate the structure of dislocations, their mobility and their contribution to anisotropic plasticity of the high pressure MgSiO_3 post-perovskite, relying on the full atomistic modeling approach. We focused our efforts on [100], [001] and $\frac{1}{2}\langle 110 \rangle$ defects. For this mineral phase, only [100] screw dislocations and $\frac{1}{2}\langle 110 \rangle\{110\}$ deformation twinning could be explored relying on the first-principles simulation techniques. Structure and mobility of [001] and $\frac{1}{2}\langle 110 \rangle$ screw dislocations and all edge dislocations can be only investigated using an appropriate semi-empirical potential, allowing to employ large atomic arrays. The main results of this study can be summarized as follows.

➤ Transferability of the pairwise potential parameterization derived by Oganov *et al.* (2000) for MgSiO_3 perovskite (bridgmanite) was examined to reproduce the structure, elastic properties and GSF excess energies of the post-perovskite phase. The ground state properties computed with the empirical potential were shown to compare well with available theoretical and experimental data. For the γ -surface calculations, which involve atomic configurations far from the equilibrium, the chosen pairwise potential parameterization was shown to reproduce well previous *ab initio* calculations by Carrez *et al.* (2007) and Metsue and Tsuchiya (2013), apart from the very unfavorable, *i.e.* high energy, (100) shear plane, where the potential model leads to γ -lines with systematically higher energies (up to $\sim 30\%$) and dissimilar shape compared to that from DFT calculations. Based on the good qualitative description of the most important (010), (001), (011) and (110) planes, where the potential accurately reproduces the shape of DFT γ -lines and provides 20-30% lower energy barriers, the empirical parameterization proposed by Oganov *et al.* (2000) was considered as valid for full atomistic modeling of defects MgSiO_3 post-perovskite.

➤ Full atomistic modeling directly provides essential structural information about screw and edge dislocation cores in MgSiO_3 post-perovskite at 120 GPa confining pressure. Among the considered [100], [001] and $\frac{1}{2}\langle 110 \rangle$ dislocations, only that with the

shortest Burgers vector [100] are characterized by compact dislocation cores, while [001] and $\frac{1}{2}\langle 110 \rangle$ dislocations exhibit complex dissociated core geometries.

Our calculations emphasize the importance of [100] screw dislocations for plastic deformation of MgSiO_3 post-perovskite. Stable [100] screw dislocations exhibit compact planar cores centered between two neighboring Mg atoms and spread in {011}. The spreading is characterized by a half-width close to ζ of ~ 1.9 Å and limited by Si-layers. The geometrical characteristics of the core deduced from the pairwise potential and DFT calculations are in good agreement (less than 5% of difference in the dislocation core spreading). The performed atomic scale modeling of dislocation mobility in absence of thermal activation indicates that lattice friction opposed to the glide of straight [100] screw dislocations in MgSiO_3 post-perovskite is highly anisotropic. Despite the narrow core spreading in {011}, remarkably low values of Peierls stress (1 GPa from the pairwise potential and 2.1 GPa from DFT calculations) are found for the glide in (010), which is not the plane of core spreading. At the same time, [100](001) glide requires stress threshold which is almost 18 times larger (based on the pairwise potential modeling) than that in (010). Dislocation glide in {011} appears to be unfavorable and could not be activated while applying a simple shear.

Both [001] screw and edge dislocations exhibit spontaneous dissociation in (010) plane into two symmetric partials characterized by the presence of $\langle 100 \rangle$ component. In case of edge dislocations, dissociation occurs into $\frac{1}{2}\langle 101 \rangle$ partials, while for the screw dislocations the $\langle 100 \rangle$ component reaches only 15%. Under applied stress, both [001](010) screw and edge dislocations behave similarly. Above the Peierls stress, the two partials glide together while keeping their stacking fault widths (~ 11 Å and ~ 42 Å for the screw and edge dislocations respectively) constant. The Peierls stress opposed to the glide of [001](010) screw dislocations is 3 GPa, while that of edge dislocations is 33% lower. Consequently, plastic deformation within this slip system is expected to be governed by the screw dislocations.

Atomistic modeling of $\frac{1}{2}[110]$ screw and edge dislocations reveals their spontaneous dissociation within (1 $\bar{1}$ 0) into $\frac{1}{3}[110]$ and $\frac{1}{6}[110]$ partials separated by a widespread stacking fault where Si-octahedra are interconnected with neighboring Si-polyhedra by corners creating a thin perovskite lamella. The pairwise potential employed in this study

was originally adjusted for MgSiO_3 perovskite (bridgmanite) phase and it is shown to significantly underestimate (7 times) the energy of such a stacking fault configuration. This results in notably overestimated (5 times) spreading of the dislocation cores. However, DFT calculations confirm that perovskite lamella represents the stable stacking fault configuration for the $\frac{1}{2}\langle 110 \rangle\{110\}$ slip system. For this slip system, the shorter partial is found to be mobile, while the larger one is not, due to a much higher lattice friction. In contrast to the $[100]$ and $[001]$ dislocations, for the $\frac{1}{2}\langle 110 \rangle\{110\}$ system, lattice friction opposed to the glide of screw dislocations is lower than that for edge dislocations. The reason of such unusual behavior can be explained by the relative ease of propagating PV-lamella through the PPV structure along $[001]$ direction (as happens for the screw dislocations), resulting from the structural relation between perovskite and post-perovskite phases.

We also investigated the possible contribution of the $\frac{1}{2}\langle 110 \rangle\{110\}$ slip system to deformation twinning. Relying on the observed $\frac{1}{2}[110](1\bar{1}0)$ dissociated dislocation core geometries, the mobile $\frac{1}{6}[110]$ dislocation partial was considered as a twinning dislocation with Burgers vector b_p . For the investigated twinning system in MgSiO_3 post-perovskite, we found that a twin nucleus can be created after formation of the third twinning partial ($N=3$), resulting in a total shear displacement of a full $\frac{1}{2}[110]$ lattice repeat. The geometry of $\frac{1}{2}\langle 110 \rangle\{110\}$ twinning in MgSiO_3 post-perovskite can be described by rotation of the parent lattice by 34.5° around the $[001]$ axis. The critical twin nucleation stress is found to be ~ 900 MPa based on DFT calculations and ~ 200 MPa based on the pairwise potential modeling. These relatively low stress values indicate that deformation twinning related to the $\frac{1}{2}\langle 110 \rangle\{110\}$ system may represent an important deformation mechanism in MgSiO_3 post-perovskite. Taking into account the high strain rates involved in deformation experiments, one can expect appearance of $\langle 110 \rangle\{110\}$ twin domains, as it was observed after DAC deformation experiments on CaIrO_3 .

➤ To address the efficiency of dislocation glide in MgSiO_3 post-perovskite under temperature conditions of D'' , the kink-pair formation mechanism, controlling thermally activated dislocation glide, was modeled. Computing critical kink-pair formation enthalpy

$\Delta H_{2k}(\sigma)$, the key parameter defining the efficiency of dislocation glide at finite temperature, allows describing evolution of the CRSS with temperature.

For compact [100](010) screw dislocations, the evolution of ΔH_{2k} with the applied stress was calculated based on the LT model in conjunction with the pairwise potential and on DFT calculations. Modeling thermally activated mobility of [100](010) slip in PPV indicates that under pressure, temperature and strain-rate conditions of the lowermost lower mantle, there is no lattice friction opposed to the glide of these dislocations (lattice friction vanishes when temperature rises above 600 K).

For dissociated [001](010) screw dislocations with complex geometry, the maximum $\Delta H_{4k}(\sigma=0)$ value was computed using the elastic interaction model by Koizumi *et al.* (1993), relying on the dislocation core characteristics inferred from the pairwise potential modeling. For this system, we did not determine the full curve describing the evolution of CRSS with temperature, but only estimated the so-called athermal temperature T_a , above which the lattice friction vanishes. For the lower mantle conditions, the critical temperature T_a is found to be in the range of 1800 – 2050 K. These results suggest that [001](010) dislocation glide at the D'' would rather occur in the athermal regime.

The easy dislocation glide along (010), parallel to the structural layering, in the absence of lattice friction has several geophysical implications:

- ◆ Although the exact viscosity of the post-perovskite cannot be calculated from dislocation mobility in the single (010) plane alone, we can predict a weak behaviour comparable with that of MgO periclase.
- ◆ This conclusion supports the scenarios that involve a weak layer in the D'' layer with, in particular, enhancement of heat transfer from the core.
- ◆ Easy dislocation glide in (010) suggests development of marked crystal preferred orientations characterized by alignment of the (010) planes.
- ◆ The high mobility of [100] screw dislocations allows for energy dissipation when a seismic wave travels through dislocation-bearing post-perovskite. We predict that deforming silicate PPV should be characterized by strong seismic attenuation.

PERSPECTIVES

- Full atomic modeling of dislocation glide in MgSiO_3 post-perovskite under lower mantle conditions indicates easy slip in (010) plane parallel to the structural layering. This results allow predicting development of (010) deformation textures (Fig. P1). However, results of this study are still not sufficient for quantifying viscosity of post-perovskite and for deriving constitutive equation describing plastic flow in this phase. To address these essential characteristics, further modeling of dislocation creep involving the interplay between dislocation glide and diffusion of point defects is needed.
- Using anisotropic lattice friction and critical twinning stress computed in this work (see Table 7.1 in Chapter 7), one can further perform VPSC modeling of deformation textures (Fig. P1) and seismic properties of PPV aggregates and more complex (*e.g.* two-phase PPV + MgO) aggregates at D'' conditions.

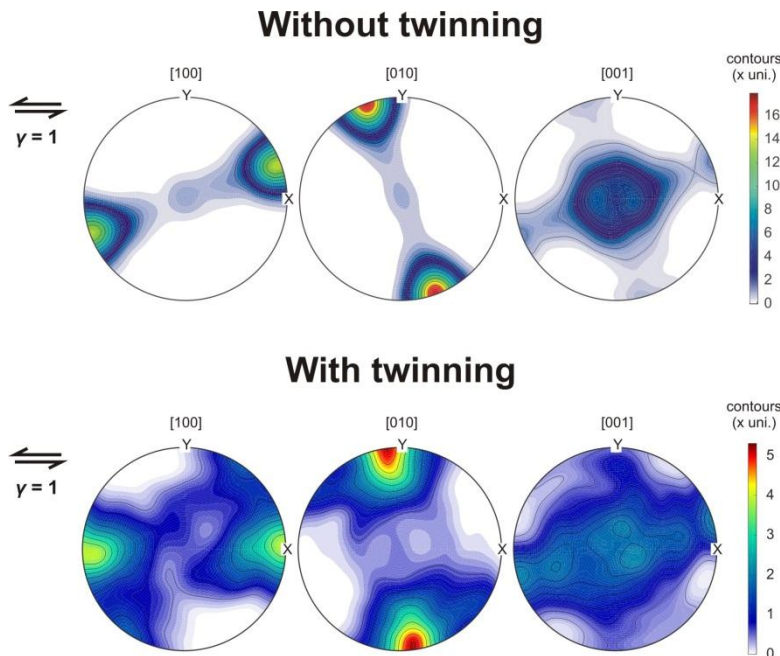


Fig. P1. Pole figures of deformation textures (at shear strain $\gamma = 1$) in MgSiO_3 PPV computed with VPSC model using the Peierls stresses and critical twin nucleation stress reported in this work (Table 7.1). Horizontal X axis is parallel to the shear direction, vertical Y axis is normal to the shear plane. VPSC modeling is done by A. Tommasi

- In order to address ability of low pressure PPV analogues (*e.g.* CaIrO_3 , CaPtO_3 , MgGeO_3) to qualitatively reproduce anisotropic plasticity of high pressure MgSiO_3 PPV, atomic-scale modeling of dislocations and twinning could be performed for these phases, by analogy with the simulations reported in this work.

ACKNOWLEDGMENTS

After living and working in Lille for three years, I would like to sincerely thank some people for their contribution to my scientific achievements and everyday life.

First of all, I would like to thank my supervisors Prof. Patrick Cordier and Prof. Philippe Carrez. It was a great pleasure for me to work together and to be a part of the RheoMan group. From the very beginning of my PhD project, I felt to be at the right place at the right time. Finishing my studies in Lille, I have a strong believe that it was not simply about place and time but mainly about the two competent professors guiding me. I do appreciate the exceptional freedom and family-like atmosphere we had in the group. I also would like to thank Patrick and Philippe for the broad scientific knowledge I've learned from them (starting from technical computational problems and finishing with global philosophical issues of planetary scale). Certainly, I will do my best to profit from this knowledge in the coming future. In this context, it's also worth acknowledging all the members of the RheoMan group for their practical advices and willingness to share their knowledge and experience. Francesca Boioli, Pierre Hirel, Karine Gouriet, Antoine Kraych, Srinivasan Mahendran, Riccardo Reali, Sebastian Ritterbex and Xiao-Yu Sun, thank you all guys! This PhD would have been much more challenging without your technical assistance and useful advices.

Besides the RheoMan group, I would like to thank Dr. Andrea Tommasi, Prof. John Brodholt, Dr. Laurent Pizzagalli, Prof. Paul Tackley and Prof. Maureen Long for being a part of the committee for my PhD defense. It was a remarkable experience and real pleasure to have such a jury. I very much appreciate their contribution to the scientific discussion and all the fair comments which helped improving clarity of the manuscript.

Thanks to the advanced ERC funding, I've had a chance to travel all over the globe and participate in numerous scientific meetings, conferences and workshops. Such extensive traveling could not be so smooth without administrative assistance of Daniele Duveau, managing financial issues of the RheoMan project.

Moving from Moscow to Lille would not be easy without the financial support from Dr. Oleg Kuskov, head of Dept. of Thermodynamics and Mathematical Modeling at Vernadsky Institute of Geochemistry RAS. His strong belief in my professional perspectives has particularly facilitated the beginning of my life in France. As we know well, sometimes, the most difficult thing is to get started and I'm very much grateful to those who supported me at that critical moment. Besides, Dr. Kuskov, I would like to thank my friends Olya Fadeeva, Evgeny Lashchenkov and Nina Sidorova for their great assistance during the tough transition period in August 2013. Спасибо, ребята! С такими друзьями хоть на край света.

Lastly, I would like to use this opportunity and acknowledge my former advisors from Moscow State University, namely Prof. Nikolay Eremin and Prof. Vadim Urusov from Dept. of Geology; and Prof. Valery Vavilov from Dept. of Mechanics and Mathematics. I don't want to say banal or pathetic things about these people. One can't underestimate their contribution to my major education and to my enthusiastic attitude to science. Unfortunately, even very good and talented people can't stay with us forever and I endlessly reproach myself for missing a chance to acknowledge Prof. Vavilov and Prof. Urusov in person. Due to them, I fell in love with the magic beauty of geometry and symmetry. I wish each and every student could have such outstanding teachers.

Bibliography

- Akber-Knutson S, Steinle-Neumann G and Asimow PD (2005) Effect of Al on the sharpness of the MgSiO₃ perovskite to post-perovskite phase transition. *Geophysical Research Letters* 32: L14303
- Alfè D, Gillan MJ, Price GD (2002) Composition and temperature of the earth's core constrained by combining *ab initio* calculations and seismic data. *Earth and Planetary Science Letters* 195:91–98
- Ammann MW, Brodholt JP, Wookey J, Dobson DP (2010) First-principles constraints on diffusion in lower-mantle minerals and a weak D'' layer. *Nature* 465:462–465
- Amodeo J, Carrez Ph, Devincere B, and Cordier P (2011) Multiscale modelling of MgO plasticity. *Acta Materialia* 59:2291–2301
- Anderson DL, and Hart RS. (1978) Q of the Earth. *Journal of Geophysical Research: Solid Earth* 83:5869–5882
- Andraut D, Munoz M, Bolfan-Casanova N, Guignot N, Perrillat J, Aquilanti G, Pascarelli S (2010) Experimental evidence for perovskite and post-perovskite coexistence throughout the whole D'' region. *Earth and Planetary Science Letters* 293:90–96
- Baraffe I, Chabrier G, Fortney J, and Sotin C. (2014) Planetary internal structures. *Protostars and Planets VI*, University of Arizona Press, 24.
- Batalha NM, Borucki WJ, Bryson ST, Buchhave LA, Caldwell DA, et al. (2011) Kepler's First Rocky Planet: Kepler-10b. *The Astrophysics Journal* 729:27
- Bitzek E, Koskinen P, Gahler F, Moseler M, Gumbsch P (2006) Structural Relaxation Made Simple. *Physical Review Letters* 97: 170201 (2006)
- Blöchl PE (1994) Projector augmented-wave method. *Physical Review B* 50: 17953
- Boehler R (2000) High-pressure experiments and the phase diagram of lower mantle and core materials. *Reviews of Geophysics* 38:221–245
- Born M, and Mayer JE (1932) Zur Gittertheorie der Ionenkristalle. *Zeitschrift für Physik* 75: 1-18
- Buckingham RA. (1938) The classical equation of state of gaseous helium, neon and argon. *Proceedings of the Royal Society of London A* 168:264-283
- Buffett BA (2007) A bound on heat flow below a double crossing of the perovskite-postperovskite phase transition. *Geophysical Research Letters* 34:L17302
- Bulatov VV, and Cai W (2006) Computer simulations of dislocations. 300 p. Oxford University press
- Bulatov VV, Justo JF, Cai W, Yip S, Argon AS, Lenosky T, M de Koning M, and T. Diaz de la Rubia (2001) Parameter-free modelling of dislocation motion: The case of silicon. *Philosophical Magazine A*, 81:5, 1257-1281
- Bulatov VV, Richmond O, Glazov MV (1999) An atomistic dislocation mechanism of pressure-dependent plastic flow in aluminum. *Acta Materialia* 47:3507–3514

- Cai W, Bulatov VV, Chang J, Li J, Yip S (2004) Dislocation core effects on mobility. In *Dislocations in Solids*, eds. Nabarro FRN and Hirth JP. Vol. 12, p. 1-80, Elsevier, Amsterdam
- Caillard D and Martin J (2003) *Thermally activated mechanisms in crystal plasticity*. 452 p. Pergamon press, Amsterdam
- Caracas R and Cohen RE (2005) Effect of chemistry on the stability and elasticity of the perovskite and post-perovskite phases in the $\text{MgSiO}_3\text{--FeSiO}_3\text{--Al}_2\text{O}_3$ system and implications for the lowermost mantle. *Geophysical Research Letters* 32:L16310
- Carrez Ph, Ferré D, Cordier P (2007a) Peierls–Nabarro model for dislocations in MgSiO_3 post-perovskite calculated at 120 GPa from first principles. *Philosophical Magazine* 87:3229–3247
- Carrez Ph, Ferré D, Cordier P (2007b) Implications for plastic flow in the deep mantle from modelling dislocations in MgSiO_3 minerals. *Nature Letters* 446:68–70
- Carrez Ph, Walker AM, Metsue A, Cordier P (2008) Evidence from numerical modeling for 3D spreading of [001] screw dislocations in Mg_2SiO_4 forsterite. *Philosophical Magazine* 88:2477-2485
- Carrier P, Justo JF and Wentzcovitch RM (2008) Quasiharmonic elastic constants corrected deviatoric thermal stresses. *Physical Review B* 78:144302.
- Catalli K, Shim S, Prakapenka V (2009) Thickness and Clapeyron slope of the post-perovskite boundary. *Nature* 462:782–785
- Catlow CRA, and Price GD (1990) Computer modelling of solid-state inorganic materials. *Nature* 347: 243-347
- Chang J, Cai W, Bulatov VV, Yip S (1999) Molecular dynamics study of edge dislocation motion in a bcc metal. *Journal of Computer-Aided Molecular Design* 6:165–173
- Chang J, Cai W, Bulatov VV, Yip S (2002) Molecular dynamics simulations of motion of edge and screw dislocations in a metal. *Computational Materials Science* 23:111–115
- Cobden L, and Thomas C (2013) The origin of D'' reflections: a systematic study of seismic array data sets. *Geophysical Journal International* 194:1091-1118
- Cobden L, Thomas C, Trampert J (2015) Seismic detection of post-perovskite inside the Earth, in “The Earth heterogeneous mantle”, eds. Khan A, Deschamps F, p. 391-440, Springer International Publishing, Switzerland
- Cooper RE (1965) The equilibrium shape of deformation twins. *Acta Metallurgica* 13:46-48
- Cooper RE (1966) The equilibrium shape of deformation twins - II. *Acta Metallurgica* 14:78-80
- Cordier P, Amodeo J, and Carrez Ph (2012) Modelling the rheology of MgO under Earth 's mantle pressure, temperature and strain rates. *Nature* 481:177–180
- Cottaar S, and Romanowicz B (2013) Observations of changing anisotropy across the southern margin of the African LLSVP. *Geophysical Journal International* 195:1184–1195

- Cottaar S, Li M, McNamara A, Romanowicz B, and Wenk H-R. (2014) Synthetic seismic anisotropy models within a slab impinging on the core-mantle boundary. *Geophysical Journal International* 199, 164–177
- Davies DR, Goes S, Lau HCP (2015) Thermally dominated deep mantle: a review, in “The Earth heterogeneous mantle”, eds. Khan A, Deschamps F, p. 441-477, Springer International Publishing, Switzerland
- Deschamps F, Li Y, and Tackley PJ (2015) Large-scale thermo-chemical structure of the deep mantle: observations and models, in “The Earth heterogeneous mantle”, eds. Khan A, Deschamps F, p. 479-515, Springer International Publishing, Switzerland
- Dezerald L, Proville L, Ventelon L, Willaime F, and Rodney D (2015) First-principles prediction of kink-pair activation enthalpy on screw dislocations in bcc transition metals: V, Nb, Ta, Mo, W, and Fe. *Physical Review B* 91:094105
- Dezerald L, Ventelon L, Clouet E, Denoual C, Rodney D, and Willaime F (2014) Ab initio modeling of the two-dimensional energy landscape of screw dislocations in bcc transition metals. *Physical Review B* 89: 024104
- Douin J, Veyssi re P, and Beauchamp P (1986) Dislocation line stability in Ni₃Al. *Philosophical Magazine* 54: 375-393
- Doukhan J, and Christie J (1982) Plastic deformation of silimanite Al₂SiO₅ single crystals under confining pressure and TEM investigation of the induced defect structure. *Bulletin de Mineralogie* 105: 583-589
- Doukhan J, Doukhan N, Koch P, and Christie J (1985) Transmission electron microscopy investigation of lattice defects in Al₂SiO₅ polymorphs and plasticity induced polymorphic transformations. *Bulletin de Mineralogie* 108: 81-96
- Durand S, Matas J, Ford S, Ricard Y, Romanowicz B, Montagner J-P (2013) Insights from ScS–S measurements on deep mantle attenuation. *Earth and Planetary Science Letters* 374:101–110
- Duval-Riviere ML, and Vicens J (1994) Polytypic transformation and gliding behavior in polycrystalline α -SiC deformed by compression at high temperatures. *Philosophical Magazine* 69:451-470
- Dziewonski AM, and Anderson DL (1981) Preliminary reference Earth model. *Physics of the Earth and Planetary Interiors* 25:297-356
- Ewald PP (1921) Die Berechnung optischer und elektrostatischer Gitterpotentiale. *Annals of Physics* 64: 253.
- Farla R, Amulele G, Girard J, Miyajima N, and Karato S (2015) High-pressure and high-temperature deformation experiments on polycrystalline wadsleyite using the rotational Drickamer apparatus. *Physics and Chemistry of Minerals* 42:541–558
- Ford HA, and Long MD (2015) A regional test of global models for flow, rheology, and seismic anisotropy at the base of the mantle. *Physics of the Earth and Planetary Interiors* 245: 71–75

- Frenkel J, and Kontorova TA (1938) On the theory of plastic deformation and twinning. *Phys. Z. Sowjetunion* 13:1–10
- Gale JD, and Rohl AL (2003) The General Utility Lattice Program (GULP). *Molecular Simulation* 29: 291 – 341
- Garnero EJ and Helmberger DV (1995) A very slow basal layer underlying large-scale low-velocity anomalies in the lower mantle beneath the Pacific: evidence from core phases. *Earth and Planetary Science Letters* 91:161-176
- Girard J, Amulele G, Farla R, Mohiuddin A, and Karato S (2016) Shear deformation of bridgmanite and magnesiowüstite aggregates at lower mantle conditions. *Science* 351:144–147
- Godet J, Pizzagalli L, Brochard S, Beauchamp P (2003) Comparison between classical potentials and ab initio methods for silicon under large shear. *Journal of Physics Condensed Matter* 15:6943-6953
- Grocholski B, Catalli K, Shim S, Prakapenka V (2012) Mineralogical effects on the detectability of the postperovskite boundary. *Proceedings of the National Academy of Sciences* 109:2275–2279
- Guyot P, Dorn JE (1967) A critical review of the peierls mechanism. *Canadian Journal of Physics* 45:983-1016
- Hayward E, Deo C , Uberuaga BP, and Tomé CN (2012) The interaction of a screw dislocation with point defects in bcc iron. *Philosophical Magazine* 92:1-20
- Heinz DL and Jeanloz R (1984) The equation of state of the gold calibration standard. *Journal of Applied Physics* 55:885–93
- Henkelman G, Uberuaga BP, Harris DJ, Harding JH, and Allan NL (2005) MgO addimer diffusion on MgO(100): A comparison of ab initio and empirical models. *Physical Review B*, 72: 115437
- Hernlund JW, Thomas C, Tackley PJ (2005) A doubling of the post-perovskite phase boundary and structure of the Earth's lowermost mantle. *Nature* 434:882–886
- Hirel P (2015) Atomsk: A tool for manipulating and converting atomic data files. *Computer Physics Communications* 197:212-219
- Hirel P, Carrez Ph, and Cordier P (2016) From glissile to sessile: effect of temperature on <110> dislocations in perovskite materials. *Scripta Materialia*, 120, 67-70
- Hirel P, Mark AF, Castillo-Rodriguez M, SigleW, Mrovec M, and Elsässer C (2015) Theoretical and experimental study of the core structure and mobility of dislocations and their influence on the ferroelectric polarization in perovskite KNbO₃. *Physical Review B* 92:214101
- Hirel P, Mrovec M, Elsässer C (2012) Atomistic simulation study of <110> dislocations in strontium titanate. *Acta Materialia* 60: 329–338
- Hirose K, Karato S, Cormier VF, Brodholt JP, Yuen DA (2006) Unsolved problems in the lowermost mantle. *Geophysical Research Letters* 33:L12S01

- Hirose K, Nagaya Y, Merkel S, Ohishi Y (2010) Deformation of MnGeO_3 post-perovskite at lower mantle pressure and temperature. *Geophysical Research Letters* 37:L20302
- Hirth JP, and Lothe J (1982) *Theory of Dislocations*. 2nd Edition. 857 p. Krieger Publishing Company, Malabar
- Hohenberg P, and Kohn W (1964) Inhomogeneous electron gas. *Physical Review* 136: 864 -871
- Holmes NC, Moriarty JA, Gathers GR, Nellis WJ (1989) The equation of state of platinum to 660 GPa (6.6 Mbar). *Journal of Applied Physics* 66:2962–67
- Hustoft J, Amulele G, Ando J, Otsuka K, Du Zh, Zhicheng Jing Zh, Karato S (2013) Plastic deformation experiments to high strain on mantle transition zone minerals wadsleyite and ringwoodite in the rotational Drickamer apparatus. *Earth and Planetary Science Letters* 361:7–15
- Hutko AR, Lay T, Revenaugh J (2009) Localized double-array stacking analysis of PcP: D'' and ULVZ structure beneath the Cocos plate, Mexico, central Pacific, and north Pacific. *Phys Earth Planet Inter* 173:60–74
- Hutko AR, Lay T, Revenaugh J, Garnero EJ (2008) Anticorrelated seismic velocity anomalies from post-perovskite in the lowermost mantle. *Science* 320:1070–1074
- Hwang YK, Ritsema J (2011) Radial Q_μ structure of the lower mantle from teleseismic body-wave spectra. *Earth and Planetary Science Letters* 303:369–375
- Iitaka T, Hirose K, Kawamura K, Murakami M (2004) The elasticity of the MgSiO_3 post-perovskite phase in the Earth's lowermost mantle. *Nature* 430:442–445
- Ismail-Beigi S, Arias TA (2000) Ab initio study of screw dislocations in Mo and Ta: a new picture of plasticity in bcc transition metals. *Physical Review Letters* 87:1499–1502
- Jackson I, and Faul UH (2010) Grainsize-sensitive viscoelastic relaxation in olivine: Towards a robust laboratory-based model for seismological application. *Physics of the Earth and Planetary Interiors* 183, 151–163
- Jamieson JC, Fritz JN, Manghnani MH (1982) Pressure measurement at high temperature in X-ray diffraction studies: gold as a primary standard. In *High-Pressure Research in Geophysics*, eds. S Akimoto, MH Manghnani, p. 27–48, Tokyo: Cent.Acad. Publ. Jpn.
- Joós B, and Duesbery MS (1997) Dislocation kink migration energies and the Frenkel-Kontorowa model. *Physical Review B* 55:11161
- Joós B, Ren Q, Duesbery MS (1994) Peierls-Nabarro model of dislocations in silicon with generalized stacking-fault restoring forces. *Physical Review B* 50:5890
- Joós B, Zhou J (2001) The Peierls–Nabarro model and the mobility of the dislocation line. *Philosophical Magazine A* 81:1329–1340
- Karato S (1998) Dislocation model of seismic wave attenuation and micro-creep in the Earth: Harold Jeffreys and the rheology of the solid Earth. *Pure and Applied Geophysics* 153:239–256

- Karato S (2010) The influence of anisotropic diffusion on the high-temperature creep of a polycrystalline aggregate. *Physics of the Earth and Planetary Interiors* 183:468–472
- Karato S, and Spetzler HA (1990) Defect microdynamics in minerals and solid state mechanisms of seismic wave attenuation and velocity dispersion in the mantle. *Reviews of Geophysics* 28:399–421
- Kawazoe T, Nishiyama N, Nishihara Y, and Irifune T (2010) Deformation experiment at P–T conditions of the mantle transition zone using D-DIA apparatus. *Physics of the Earth and Planetary Interiors* 183:190–195
- Kesson S, Fitz Gerald J, and Shelley J (1998) Mineralogy and dynamics of a pyrolite lower mantle. *Nature* 393:252–255
- Kibey S, Liu JB, Johnson DD, and Sehitoglu H (2007) Predicting twinning stress in fcc metals: Linking twin energy pathways to twin nucleation. *Acta Materialia* 55:6843–6851
- Knittle E, and Jeanloz R (1987) Synthesis and equation of state of (Mg,Fe)SiO₃ perovskite to over 100 GPa. *Science* 235:668–670
- Kocks UF, Argon AS, and Ashby MF (1975) *Thermodynamics and kinetics of slip*. Pergamon Press
- Kohn W, and Sham LJ (1965) Self-consistent equations including exchange and correlation effects. *Physical Review* 140: 1133 – 1138
- Koizumi H, Kirchner HOK (1994) Nucleation of trapezoidal kink pairs on a Peierls potential. *Philosophical Magazine* 69:805-820
- Koizumi H, Kirchner HOK, Suzuki T (1993) Kink pair nucleation and critical shear stress. *Acta Metallurgica et Materialia* 41:3483-3493
- Krasheninnikov AV, Lehtinen PO, Foster AS, Pyykkö P, and Nieminen RM (2009) Embedding Transition-Metal Atoms in Graphene: Structure, Bonding, and Magnetism. *Physical Review Letters* 102: 126807
- Kraych A (2016) Modélisation à l'échelle atomique du rôle des dislocations dans la déformation de la bridgmanite. PhD thesis
- Kraych A, Carrez Ph, Cordier P (2016b) On dislocation glide in MgSiO₃ bridgmanite at high-pressure and high-temperature. *Earth and Planetary Science Letters* 452:60-68
- Kraych A, Carrez Ph, Hirel P, Clouet E, Cordier P (2016a) Peierls potential and kink-pair mechanism in high-pressure MgSiO₃ perovskite: an atomic scale study. *Physical Review B* 93:014103
- Kresse G, and Furthmüller J (1996) Efficient iterative schemes for *ab initio* total-energy calculations using a plane-wave basis set. *Physical Review B* 54: 11169
- Lawrence JF, and Wyession ME (2006) QLM9: A new radial quality factor (Q_μ) model for the lower mantle. *Earth and Planetary Science Letters* 241:962–971
- Lay T (2008) Sharpness of D'' discontinuity beneath the Cocos plate: implications for the perovskite to post-perovskite phase transition. *Geophysical Research Letters* 35:L03304

- Lay T, and Helmberger DV (1983) A lower mantle S-wave triplication and the shear velocity structure of D". *Geophysical Journal of the Royal Astronomical Society* 75:799-838
- Lay T, and Helmberger DV (1983) The shear-wave velocity gradient at the base of the mantle. *Journal of Geophysical Research* 88:8160
- Lay T, Hernlund J, Garnero EJ, Thorne MS (2006) A post-perovskite lens and D'' heat flux beneath the central Pacific. *Science* 314:1272–1276
- Lewis GV, and Catlow CRA (1985) Potential models for ionic oxides. *Journal of Physics C: Solid State Physics* 18: 1149
- Lewis JG, and van de Geijn RA (1993) Distributed memory matrix-vector multiplication and conjugate gradient algorithms. In *Proceedings on Supercomputing'93*:484–492. ACM Press, New York
- Li Y, Deschamps F, and Tackley PJ (2014) Effects of low-viscosity post-perovskite on the stability and structure of primordial reservoirs in the lower mantle. *Geophysical Research Letters* 41:7089–7097
- Liu ZJ, Sun XW, Zhang CR, Hu JB, Cai LC, Chen QF (2012) High pressure physical properties of magnesium silicate post-perovskite from *ab-initio* calculations. *Bulletin of Materials Science* 35:665-672
- Long MD (2009) Complex anisotropy in D'' beneath the eastern Pacific from SKS-SKKS splitting discrepancies. *Earth and Planetary Science Letters* 283:181-189
- Mainprice D, Barruol G, and Ismaïl WB (2000) The seismic anisotropy of the Earth's mantle: From single crystal to polycrystal, in "Earth's deep interior: mineral physics and tomography from the atomic to the global scale", eds. Karato S-I, Forte A, Liebermann R, Masters G and Stixrude L, p. 237-264, AGU, Washington DC
- Mao WL, Meng Y, Shen G, Prakapenka VB, Campbell AJ, Heinz DL et al. (2005) Iron-rich silicates in the Earth's D'' layer. *Proceedings of the National Academy of Sciences* 102:9751-9753
- Mao WL, Shen G, Prakapenka V, Meng Y, Campbell A, Heinz D, Shu J, Hemley R, Mao H (2004) Ferromagnesian postperovskite silicates in the D'' layer of the Earth. *Proceedings of the National Academy of Sciences* 101:15867–15869
- Marquardt H, and Miyagi L. Slab stagnation in the shallow lower mantle linked to an increase in mantle viscosity. *Nature Geosciences* 8:311–314
- Martens J (2010) Deep learning via Hessian-free optimization. Appearing in *Proceedings of the 27th International Conference on Machine Learning*. Haifa, Israel
- McCormack R, Dobson DP, Walte NP, Miyajima N, Taniguchi T, and Wood IG (2011) The development of shape- and crystallographic-preferred orientation in CaPtO₃ post-perovskite deformed in pure shear. *American Mineralogist* 96: 630–1635
- Merkel S, Kubo A, Miyagi L, Speziale S, Duffy TS, Mao H-K, and H.-R. Wenk (2006) Plastic deformation of MgGeO₃ post-perovskite at lower mantle pressures, *Science* 311:644-646

- Merkel S, McNamara AK, Kubo A, Speziale S, Miyagi L, Meng Y, Duffy TS, and Wenk H-K (2007) Deformation of (Mg,Fe)SiO₃ post-perovskite and D'' anisotropy. *Science* 316:1729–1732
- Metsue A, and Tsuchiya T (2012) Thermodynamic properties of (Mg, Fe²⁺)SiO₃ perovskite at the lower-mantle pressures and temperatures: an internally consistent LSDA+U study. *Geophysical Journal International* 190:310–322
- Metsue A, and Tsuchiya T (2013) Shear response of Fe-bearing MgSiO₃ post-perovskite at lower mantle pressures. *Proceedings of the Japan Academy B* 89:51–58
- Metsue A, Carrez Ph, Mainprice D, and Cordier P (2009) Numerical modeling of dislocations and deformation mechanisms in CaIrO₃ and MgGeO₃ post-perovskites – comparison with MgSiO₃ post-perovskite. *Physics of Earth and Planetary Interiors* 174:165-173
- Miyagi L, Amulele G, Otsuka K, Du Zh, Farla R, Karato S (2014) Plastic anisotropy and slip systems in ringwoodite deformed to high shear strain in the Rotational Drickamer Apparatus. *Physics of the Earth and Planetary Interiors* 228:244–253
- Miyagi L, Kanitpanyacharoen W, Kaercher P, Lee KKM, and Wenk H-R (2010) Slip systems in MgSiO₃ post-perovskite: Implications for D'' anisotropy. *Science* 329: 1639-1642
- Miyagi L, Kanitpanyacharoen W, Kaercher P, Stackhouse S, Militzer B, and Wenk H-R (2011) The enigma of post-perovskite anisotropy: deformation versus transformation textures. *Physics and Chemistry of Minerals* 38:665-678
- Miyagi L, Nishiyama N, Wang Y, Kubo A, West DV, Cava RJ, Duffy TS, Wenk HR (2008) Deformation and texture development in CaIrO₃ post-perovskite phase up to 6 GPa and 1300 K. *Earth and Planetary Science Letters* 268:515–525
- Miyajima N, Niwa K, Heidelbach F, Yagi T and Ohgushi K (2010) Deformation microtextures in CaIrO₃ post-perovskite under high stress conditions using a laser-heated diamond anvil cell. *Journal of Physics: Conference Series* 215:012097
- Miyajima N, Ohgushi K, Ichihara M, Yagi T (2006) Crystal morphology and dislocation microstructures of CaIrO₃: a TEM study of an analogue of the MgSiO₃ post-perovskite phase. *Geophysical Research Letters* 33:L12302
- Miyajima N, Walte N (2009) Burgers vector determination in deformed perovskite and post-perovskite of CaIrO₃ using thickness fringes in weak-beam dark-field images. *Ultramicroscopy* 109:683–692
- Möller HJ (1978) The movement of dissociated dislocations in the diamond-cubic structure. *Acta Metallurgica* 26:963-973
- Monkhorst HJ, and Pack JD (1976) Special points for Brillouin-zone integrations. *Physical Review B* 13: 5188–5192
- Montagner J.-P, and Kennett BLN (1996) How to reconcile body-wave and normal-mode reference Earth models. *Geophysical Journal International* 125: 229-248
- Murakami M, Hirose K, Kawamura K, Sata N, Ohishi Y (2004) Post-perovskite phase transition in MgSiO₃. *Science* 304:855–858

- Murakami M, Hirose K, Sata N, Ohishi Y (2005) Post-perovskite phase transition and mineral chemistry in the pyrolitic lowermost mantle. *Geophysical Research Letters* 32:L03304
- Nabarro FRN (1947) Dislocation in a simple cubic lattice. *Proceedings of the Physical Society* 59: 256-272
- Nakagawa T, Tackley PJ (2011) Effects of low-viscosity post-perovskite on thermo-chemical mantle convection in a 3-D spherical shell. *Geophysical Research Letters* 38:1–6
- Nishihara Y. et al. (2008) Plastic deformation of wadsleyite and olivine at high-pressure and high-temperature using a rotational Drickamer apparatus (RDA). *Physics of the Earth and Planetary Interiors* 170:156–169
- Nishio-Hamane D, Fujino K, Seto Y, Nagai T (2007) Effect of the incorporation of FeAlO₃ into MgSiO₃ perovskite on the post-perovskite transition. *Geophysical Research Letters* 34:L12307
- Nisr C, Ribárik G, Ungár T, Vaughan GBM, Cordier P, and Merkel S (2012) High resolution three-dimensional X-ray diffraction study of dislocations in grains of MgGeO₃ post-perovskite at 90 GPa. *Journal of Geophysical Research* 117: B03201
- Niwa K, Miyajima N, Seto Y, Ohgushi K, Gotou H, Yagi T (2012) In situ observation of shear stress-induced perovskite to post-perovskite phase transition in CaIrO₃ and the development of its deformation texture in a diamond-anvil cell up to 30 GPa. *Physics of the Earth and Planetary Interiors* 194-195:10–17
- Niwa K, Yagi T, Ohgushi K, Merkel S, Miyajima N, Kikegawa T (2007) Lattice preferred orientation in CaIrO₃ perovskite and post-perovskite formed by plastic deformation under pressure. *Physics and Chemistry of Minerals* 34:679–686
- Nowacki A, Walker AM, Wookey J, and Kendall JM (2013) Evaluating post-perovskite as a cause of D'' anisotropy in regions of paleosubduction. *Geophysical Journal International* 192:1085–1090
- Oganov AR, Brodholt JP, Price GD (2000) Comparative study of quasiharmonic lattice dynamics, molecular dynamics and Debye model applied to MgSiO₃ perovskite. *Physics of Earth Planetary Interiors* 122: 277–288
- Oganov AR, Martonak R, Laio A, Raiteri P, and Parrinello M (2005) Anisotropy of Earth's D'' layer and stacking faults in the MgSiO₃ post-perovskite phase. *Nature* 438:1142-1144
- Oganov AR, Ono S (2004) Theoretical and experimental evidence for a post-perovskite phase in MgSiO₃ in the Earth's D'' layer. *Nature* 430:445–448
- Ogata S, Li J, and Yip S (2005) Energy landscape of deformation twinning in bcc and fcc metals. *Physical Review B* 71:224102
- Ohta K, Hirose K, Lay T, Sata N, Ohishi Y (2008) Phase transitions in pyrolite and MORB at lowermost mantle conditions: implications for a MORB-rich pile above the core-mantle boundary. *Earth and Planetary Science Letters* 267:107–117

- Ojha A, Sehitoglu H, L Patriarca L, and Maier HJ (2014) Twin nucleation in Fe-based bcc alloys - modeling and experiments. *Modelling and Simulation in Materials Science and Engineering* 22: 075010
- Okada T, Yagi T, and Nishio-Hamane D (2011) High-pressure phase behavior of MnTiO_3 : Decomposition of perovskite into MnO and MnTi_2O_5 . *Physics and Chemistry of Minerals* 38:251–258
- Ono S, and Oganov AR (2005) *In situ* observations of phase transition between perovskite and CaIrO_3 -type phase in MgSiO_3 and pyrolitic mantle composition. *Earth and Planetary Science Letters* 236:914–932
- Osetsky YN, and Bacon DJ (2003) An atomic-level model for studying the dynamics of edge dislocations in metals. *Modeling and Simulation Materials Science and Engineering* 11: 427–446
- Peierls R (1940) The size of a dislocation. *Proceedings of the Physical Society* 52:34–37
- Perdew JP, and Wang Y (1992) Accurate and simple analytic representation of the electron gas correlation energy. *Physical Review B* 45: 13244 – 13249
- Perdew JP, and Zunger A (1981) Self-interaction correction to density-functional approximations for many-electron systems. *Physical Review B* 23: 5048 – 5079
- Perdew JP, Burke K and Ernzerhof M (1996) Generalized gradient approximation made simple. *Physical Review Letters* 77:3865-3868
- Pirouz P, and Yang J (1993) Polytypic transformations in SiC: the role of TEM. *Ultramicroscopy* 51:189-214
- Pizzagalli L, Beauchamp P, and Jónsson H (2008a) Calculations of dislocation mobility using Nudged Elastic Band method and first principles DFT calculations. *Philosophical Magazine* 88:91–100
- Pizzagalli L, Pedersen A, Arnaldsson A, Jónsson H, and Beauchamp P (2008b) Theoretical study of kinks on screw dislocation in silicon. *Physical Review B* 77: 064106
- Plimpton S (1995) Fast parallel algorithms for short-range molecular dynamics. *Journal of Computational Physics* 117: 1–19
- Price GD, and Voadlo L (1996) Computational Mineralogy. *Comptes rendus de l'academie des sciences - sciences de la Terre et des planetes* 323: 357 -371
- Price GD, Parker SC, Leslie M (1987) The lattice dynamics of forsterite. *Mineralogical Magazine* 5:157-170
- Proville L, Ventelon L, and Rodney D (2013) Prediction of the kink-pair formation enthalpy on screw dislocations in α -iron by a line tension model parameterized on empirical potentials and first-principles calculations. *Physical Review B* 87:144106
- Queloz D, Bouchy F, Moutou C, Hatzes A, Hébrard G, Alonso R, Auvergne M, Baglin A, et al. (2009) The CoRoT-7 planetary system: two orbiting super-Earths. *Astronomy and Astrophysics* 506:303–319

- Rabone JAL, and De Leeuw NH (2006) Interatomic potential models for natural apatite crystals: Incorporating strontium and the lanthanides. *Journal of Computational Chemistry* 27: 253–266
- Ritterbex S, Carrez Ph, and Cordier P (2016) Modeling dislocation glide and lattice friction in Mg_2SiO_4 wadsleyite in conditions of the Earth's transition zone. *American Mineralogist* 101:2085-2094
- Ritterbex S, Carrez Ph, Gouriet K, and Cordier P (2015) Modeling dislocation glide in Mg_2SiO_4 ringwoodite: Towards rheology under transition zone conditions. *Physics of the Earth and Planetary Interiors* 248:20–29
- Rivera EJ, Lissauer JJ, Butler RP, Marcy GW, Vogt SS, Fischer DA, Brown TM, et al. (2005) A $\sim 7.5M_{\oplus}$ Planet Orbiting the Nearby Star, GJ 876. *The Astrophysical Journal* 634:625–640
- Rodney D, and Proville L (2009) Stress-dependent peierls potential : Influence on kink-pair activation. *Physical Review B* 79:094108
- Romanowicz B, and Durek J (2000) Seismological constraints on attenuation in the Earth: a review. In: Karato S, et al. (eds.) *Earth's Deep Interior: Mineral Physics and Tomography from the Atomic to the Global Scale*, AGU Monograph 117:161–180
- Romanowicz B, and Mitchell B (2007). Q of the Earth from crust to core. In: *Treatise of Geophysics* 1:731–774
- Rost S, Garnero EJ, Williams Q, and Manga M (2005) Seismological constraints on a possible plume root at the core–mantle boundary. *Nature* 435:666-669
- Rost S, Garnero EJ, Williams Q, and Manga M (2005) Seismological constraints on a possible plume root at the core–mantle boundary. *Nature* 435:666-669
- Seeger A, Schiller P (1962) The formation and diffusion of kinks as the fundamental process of dislocation movement in internal friction measurements. *Acta Metallurgica* 10:348-357
- Shieh SR, Dorfman SM, Kubo A, Prakapenka VB, Duffy TS (2011) Synthesis and equation of state of post-perovskites in the $(\text{Mg}, \text{Fe})(3)\text{Al}_2\text{Si}_3\text{O}_{12}$ system. *Earth and Planetary Science Letters* 312:422–428
- Shieh SR, Duffy T, Kubo A, Shen G, Prakapenka V, Sata N, Hirose K, Ohishi Y (2006) Equation of state of the postperovskite phase synthesized from a natural $(\text{Mg},\text{Fe})\text{SiO}_3$ orthopyroxene. *Proceedings of the National Academy of Sciences*: 103:3039–3043
- Shim SH, Duffy TS, Jeanloz R, Shen G (2004) Stability and crystal structure of MgSiO_3 perovskite to the core-mantle boundary. *Geophysical Research Letters* 31:L10603
- Shim SH, Duffy TS, Kenichi T (2002) Equation of state of gold and its application to the phase boundaries near the 660-km depth in the mantle. *Earth and Planetary Science Letters* 203:729–39
- Sidorin I, Gurnis M, Helmberger DV (1999) Evidence for a ubiquitous seismic discontinuity at the base of the mantle. *Science* 286:1326–1331

- Sinmyo R, Hirose K, Muto S, Ohishi Y, Yasuhara A (2011) The valence state and partitioning of iron in the Earth's lowermost mantle. *Journal of Geophysical Research: Solid Earth* 116:B07205
- Sotin C, Grasset O, and Mocquet A (2007) Mass-radius curve for extrasolar Earth-like planets and ocean planets. *Icarus* 191:337–351
- Speziale S, Zha C-S, Duffy TS, Hemley RJ, Mao H-K (2001) Quasi-hydrostatic compression of magnesium oxide to 52 GPa: implications for the pressure-volume-temperature equations of state. *Journal of Geophysical Research* 106:515–28
- Stackhouse S and Brodholt JP (2007) The high-temperature elasticity of MgSiO₃ post-perovskite. In: *Post-Perovskite: The Last Mantle Phase Transition*. *Geophysical Monograph* 174:99–113
- Stamenković V, Breuer D, and Spohn T (2011) Thermal and transport properties of mantle rock at high pressure: Applications to super-Earths. *Icarus* 216:572–596
- Stroh AN (1958) Dislocations and cracks in anisotropic elasticity. *Philosophical Magazine* 3:625–646
- Sutou Y, Kamiya N, Omori T, Kainuma R, Ishida K, and Oikawa K (2004) Stress-strain characteristics in Ni–Ga–Fe ferromagnetic shape memory alloys. *Applied Physics Letters* 84:1275
- Tackley PJ (2011) Living dead slabs in 3-D: the dynamics of compositionally-stratified slabs entering a “slab graveyard D” above the core-mantle boundary. *Physics of Earth Planetary Interiors* 188:150–162
- Tackley PJ, Ammann M, Brodholt JP, Dobson DP, and Valencia D (2013) Mantle dynamics in super-Earths: Post-perovskite rheology and self-regulation of viscosity. *Icarus* 225:50–61
- Tang M, Kubin LP, and Canova GR (1998) Dislocation mobility and the mechanical response of bcc. single crystals: A mesoscopic approach. *Acta Materialia* 46:3221–3235
- Tateno S, Hirose K, Sata N and Ohishi Y (2009) Determination of post-perovskite phase transition boundary up to 4400 K and implications for thermal structure in D'' layer. *Earth and Planetary Science Letters* 277:130–136
- Thomas C, Garnero EJ, Lay T (2004) High-resolution imaging of lowermost mantle structure under the Cocos plate. *J Geophys Res Solid Earth* 109:B08307
- Timofeeva EE, Panchenko EY, Chumlyakov YI, Maier H (2012) Development of thermoelastic martensitic transformations in ferromagnetic [011]-oriented NiFeGa single crystals in compression. *Russian Physics Journal* 54:1427-1430
- Tschauner O, and Ma C. (2014) Bridgmanite, IMA 2014-017. *CNMNC Newsletter №. 21, August 2014*, p. 798. *Mineralogical Magazine* 78:797-804
- Tsuchiya J, and Tsuchiya T (2008) Postperovskite phase equilibria in the MgSiO₃-Al₂O₃ system, *Proceedings of the National Academy of Sciences* 105:19160-19164
- Tsuchiya T (2003) First-principles prediction of the *P-V-T* equation of state of gold and the 660-km discontinuity in Earth's mantle. *Journal of Geophysical Research* 108:2462

- Tsuchiya T, Tsuchiya J, Umemoto K, Wentzcovitch RM (2004a) Phase transition in MgSiO_3 perovskite in the Earth's lower mantle. *Earth and Planetary Science Letters* 224:241–248
- Tsuchiya T, Tsuchiya J, Umemoto K, Wentzcovitch RM (2004b) Elasticity of post-perovskite MgSiO_3 . *Geophysical Research Letters* 31:L14603
- Umemoto K, and Wentzcovitch RM (2011) Two-stage dissociation in MgSiO_3 post-perovskite. *Earth and Planetary Science Letters* 311:225–229
- Valencia D, O'Connell RJ, and Sasselov D (2006) Internal structure of massive terrestrial planets. *Icarus* 181:545–554
- van der Hilst RD, de Hoop MV, Wang P, Shim S, Ma P, Tenorio L (2007) Seismostratigraphy and thermal structure of Earth's core-mantle boundary region. *Science* 315:1813–1817
- Vanderbilt D (1990) Soft self-consistent pseudopotentials in a generalized eigenvalue problem. *Physical Review B* 41: 7892 – 7895
- Vegge T, Sethna JP, Cheong S-A, Jacobsen KW, Myers CR, Ralph DC (2001) Calculation of quantum tunneling for a spatially extended defect: the dislocation kink in copper has a low effective mass. *Physical Review Letters* 86:1546–1549
- Vinnik LP, Farra V, and Romanowicz B (1989) Observational evidence for diffracted SV in the shadow of the Earth's core. *Geophysical Research Letters* 16:519–522
- Vitek V (1968) Intrinsic stacking faults in body-centered cubic crystals. *Philosophical Magazine* 18:773-786
- Wallace D (1972) *Thermodynamics of Crystals*. Wiley, New York.
- Walte NP, Heidelbach F, Miyajima N, Frost D (2007) Texture development and TEM analysis of deformed CaIrO_3 : implications for the D" layer at the core-mantle boundary. *Geophysical Research Letters*
- Walte NP, Heidelbach F, Miyajima N, Frost DJ, Rubie DC, Dobson DP (2009) Transformation textures in post-perovskite: understanding mantle flow in the D" layer of the Earth. *Geophysical Research Letters* 36:L04302
- Wang J, and Sehitoglu H (2013) Twinning stress in shape memory alloys: Theory and experiments. *Acta Materialia* 61:6790–6801
- Wang Y, and Perdew JP (1991) Correlation hole of the spin-polarized electron gas, with exact small-vector and high-density scaling. *Physical Review B* 44: 13298 – 13307
- Wardle MG, Goss JP, and Briddon PR (2006) First-Principles Study of the Diffusion of Hydrogen in ZnO . *Physical Review Letters* 96:205504
- Weber M (1993) P-wave and S-wave reflections from anomalies in the lowermost mantle. *Geophysical Journal International* 115:183-210
- Wenk H-R, Cottaar S, Tomé C, McNamara A, and Romanowicz B. (2011) Deformation in the lowermost mantle: From polycrystal plasticity to seismic anisotropy. *Earth and Planetary Science Letters* 306:33–45

- Wetzcovitch R, Tsuchiya T, Tsuchiya J (2006) MgSiO₃ postperovskite at D'' conditions. *Proceedings of the National Academy of Sciences* 103:543–546
- Williams Q, and Garnero EJ (1996) Seismic evidence for partial melt at the base of Earth's mantle. *Science* 273:1528-1530
- Wright K (2003) Modelling point defects and diffusion in Earth materials. In *Computational materials science* 187: 308 – 320, Eds. Catlow CRA and Kotomin EA, Eds. IOS Press, Amsterdam.
- Wu SQ, Ji M, Wang CZ, Nguyen MC, Zhao X, Umemoto K, et al. (2014) An adaptive genetic algorithm for crystal structure prediction. *Journal of Physics. Condensed matter : an Institute of Physics Journal* 26:035402
- Yamazaki D, Yoshino T, Ohfuji H, Ando J, Yoneda A (2006) Origin of seismic anisotropy in the D'' layer inferred from shear deformation experiments on post-perovskite phase. *Earth and Planetary Science Letters* 252:372–378
- Zahn D (2011) Shearing mechanisms of MgSiO₃ at conditions of the Earth's D'' layer. *Geophysical Research Letters* 38:L16319
- Zhang F, Oganov AR (2006) Mechanisms of Al³⁺ incorporation in MgSiO₃ post-perovskite at high pressures. *Earth and Planetary Science Letters* 248:69–76
- Zhang S, Cottaar S, Liu T, Stackhouse S, Militzer B (2016) High-pressure, temperature elasticity of Fe- and Al-bearing MgSiO₃: Implications for the Earth's lower mantle. *Earth and Planetary Science Letters* 434:264-273
- Zimmerman JA, Gao H, Abraham FF (2000) Generalized stacking fault energies for embedded atom FCC metals. *Modelling and Simulation in Materials Science and Engineering* 8:103-115

List of publications

Results of this thesis have been published in the following articles:

CHAPTER 3

A.M. Goryaeva, Ph. Carrez, P. Cordier (2015) Modeling defects and plasticity in MgSiO_3 post-perovskite: Part 1-Generalized stacking faults. *Phys Chem Minerals*, Vol. 42, p. 781-792. doi: [10.1007/s00269-015-0762-9](https://doi.org/10.1007/s00269-015-0762-9) (open access)

CHAPTER 4

A.M. Goryaeva, Ph. Carrez, P. Cordier (2016). Low viscosity and high attenuation in MgSiO_3 post-perovskite inferred from atomic-scale calculations. *Scientific Reports*, Vol. 6, p. 34771. doi: [10.1038/srep34771](https://doi.org/10.1038/srep34771) (open access)

A.M. Goryaeva, Ph. Carrez, P. Cordier (2015) Modeling defects and plasticity in MgSiO_3 post-perovskite: Part 2-screw and edge [100] dislocations. *Phys Chem Minerals*, Vol. 42, p. 793-803. doi: [10.1007/s00269-015-0763-8](https://doi.org/10.1007/s00269-015-0763-8) (open access)

CHAPTER 5

A.M. Goryaeva, Ph. Carrez, P. Cordier (2017) Modeling defects and plasticity in MgSiO_3 post-perovskite: Part 3-screw and edge [001] dislocations. *Phys Chem Minerals*, in press

List of abbreviations:

AGA	Adaptive Genetic Algorithm
bcc	Body-Centered Cubic (lattice, structure)
cg	Conjugate-Gradient (algorithm)
CMB	Core-Mantle Boundary
CPO	Crystal Preferred Orientation
DAC	Diamond Anvil Cell
D-DIA	Deformation DIA (cubic-anvil apparatus)
DD-map	Differential Displacement Map
DFT	Density Functional Theory
EBSD	Electron Backscatter Diffraction
EoS	Equation of State
fcc	Face-Centered Cubic (lattice, structure)
GGA	Generalized Gradient Approximation
GPSF	Generalized Planar Fault Energy
GSF	Generalized Stacking Fault
hcp	Hexagonal Close Packed (structure)
hftn	Hessian-free truncated Newton (algorithm)
isf	Intrinsic Stacking Fault
ISS	Ideal Shear Stress
KK	Kink-kink (interaction model)
LGA	Local Density Approximation
LHDAC	Laser-Heated Diamond Anvil Cell
LLSVP	Large Low Shear-Wave Velocity Province
LT	Line Tension (model)
MD	Molecular Dynamics
MEP	Minimum Energy Path
MORB	Mid-Ocean Ridge Basalt
NEB	Nudged Elastic Band (method)
Opx	Orthopyroxene
PAW	Projector Augmented Wave (method)
PN	Peierls-Nabarro (model)
PPV	Post-Perovskite

PREM	Preliminary Reference Earth Model
PV	Perovskite
QHA	Quasiharmonic Approximation
SEM	Scanning Electron Microscopy
SF	Stacking Fault
TEM	Transmission Electron Microscopy
TZ	Transition Zone
ULVZ	Ultralow Velocity Zone
US	Ultrasoft (pseudopotential)
VPSC	Viscoplastic Self-Consistent (model)
XRD	X-Ray Diffraction

